REPORT D

AD-A249 449

Form Approved
OMB No. 0704-0188

1. AGENCY USE ONLY (Leave blank)	2. REPORT DATE	3. REPORT TYPE AND DATES COVERED
	May 1991	THESIS/~~DISSERTATION~~

4. TITLE AND SUBTITLE
A Statistical Analysis of a Convective Boundary Layer Over Lake Michigan on 10 January 1984

5. FUNDING NUMBERS

6. AUTHOR(S)
Daniel M. Rozema, Capt

7. PERFORMING ORGANIZATION NAME(S) AND ADDRESS(ES)
AFIT Student Attending: Purdue University

8. PERFORMING ORGANIZATION REPORT NUMBER
AFIT/CI/CIA- 91-108

9. SPONSORING / MONITORING AGENCY NAME(S) AND ADDRESS(ES)
AFIT/CI
Wright-Patterson AFB OH 45433-6583

10. SPONSORING / MONITORING AGENCY REPORT NUMBER

11. SUPPLEMENTARY NOTES

12a. DISTRIBUTION / AVAILABILITY STATEMENT
Approved for Public Release IAW 190-1
Distributed Unlimited
ERNEST A. HAYGOOD, Captain, USAF
Executive Officer

12b. DISTRIBUTION CODE

13. ABSTRACT *(Maximum 200 words)*

14. SUBJECT TERMS

15. NUMBER OF PAGES
127

16. PRICE CODE

17. SECURITY CLASSIFICATION OF REPORT	18. SECURITY CLASSIFICATION OF THIS PAGE	19. SECURITY CLASSIFICATION OF ABSTRACT	20. LIMITATION OF ABSTRACT

A STATISTICAL ANALYSIS OF A CONVECTIVE BOUNDARY LAYER OVER LAKE MICHIGAN ON 10 JANUARY 1984

A Thesis

Submitted to the Faculty

of

Purdue University

by

Daniel M. Rozema

In Partial Fulfillment of the

Requirements for the Degree

of

Master of Science

May 1991

ACKNOWLEDGEMENTS

My thanks to my major professor, Dr. Ernest Agee, for his enthusiastic support of my thesis research. Thanks also to the other members of my committee: Dr. Wen–Yih Sun and Dr. Phil Smith. Their suggestions and comments were most helpful.

I would like to thank Ross Aiken for setting up the data files used in this study. I also would like to thank Dan Vietor and Brett Pennington for their help in answering what must have seemed like countless hardware and software questions. My appreciation also to Michelle Breaker for proofreading this thesis and to Guan–Shu Rao and Dr. Al Howsmon for their insights into interpretation of results.

I would like to express my appreciation to the Air Force Air Weather Service for selecting me to attend graduate school, and making this thesis possible. My appreciation also to my wife Pam who has been a constant source of encouragement and moral support. Last but not least, I would like to take this opportunity to thank my best friend and Saviour Jesus Christ. Were it not for Him, none of this work could have been possible.

This research has been sponsored by the National Science Foundation Mesoscale Dynamic Meteorology Program (NSF Grant ATM–8711611), and by the Department of the Navy – Office of Naval Research (Grant N00014–86–K–0179).

TABLE OF CONTENTS

Page

LIST OF TABLES

LIST OF FIGURES

Figure Page

Figure Page

Figure Page

ABSTRACT

Rozema, Daniel M., M.S., Purdue University, May 1991. A Statistical Analysis of a Convective Boundary Layer over Lake Michigan on 10 January 1984. Major Professor: Ernest M. Agee.

This research has focused on the continued study and analysis of data collected over Lake Michigan by NCAR research aircraft during a northerly flow cold-air outbreak on 10 Jan 84 during the Lake Effect Snow Studies (LESS) project. Turbulence statistics including variances, covariances, TKE, skewness and buoyancy have been calculated from 20Hz data for u,v,w,θ_v and q for a strategically selected 30km flight segment and the two contiguous 15km flight segments that comprise such. Emphasis is placed on the interpretation and comparison among the LESS results as well as those for the Air Mass Transformation EXperiment (AMTEX), the Mesoscale Air-Sea EXchange (MASEX) Experiment and the models of Deardorff (1980) and Moeng(1984).

Of particular interest are the vertical profiles of normalized buoyancy (B) and vertical velocity skewness (S_w) for the LESS results, where the former shows a primary maximum at level 1 and a secondary maximum at level 4 with the latter most likely due to condensational heating. The vertical profile of S_w also shows positive maxima at the same levels indicating that skewness is buoyancy driven. The buoyancy profiles for the AMTEX and MASEX both show only the surface maximum with buoyancy decreasing with height from the surface to the top of the mixed layer. The buoyancy profiles of case 6 from the Deardorff model agrees very well with the LESS profile presented in this study.

1. INTRODUCTION AND STATEMENT OF OBJECTIVES

1.1 Literature Review

William Prout (1834) is credited for being the first to introduce the term convection into the field of science as he expressed in his own words: "There is at present no single term in our language employed to denote this mode of propagation of heat; but we venture to propose for that purpose the term convection which accords very well with the two other terms (conduction and radiation)." The word convection comes from the Latin word convectus meaning to bring together or carry. Webster defines convection as "the circulatory motion that occurs in a fluid at a nonuniform temperature owing to the variation of its density and the action of gravity." As a result of his pioneering work and thorough study while at the University of Paris, the name of Henri Benard (1901) has long been associated with the study of cellular convection that occurs in an unstable fluid. Benard's observations were anticipated to some degree about twenty years earlier by James Thomson (the brother of Lord Kelvin) who observed a "tessellated structure" in cooling soapy water in a tub seen in the yard of an inn. However, the most important study in the area of thermal convection clearly was that of Benard's.

Benard's experiments mark the first quantitative work on the onset of thermal instability and the role played by viscosity in the phenomenon. His work consisted of using a thin layer (approximately 1 mm thick) of whale oil called spermacetti that was heated from below with a horizontal metallic plate maintained at uniform temperature. The fluid layer, initially at rest, after becoming unstable resolved itself into a number of hexagonal convective cells with ascending motion at the cell centers

and descending motion at the periphery between adjoining cells (i.e. uphexagons or closed cells).

Lord Rayleigh (1916) went on to theoretically examine the physical conditions leading to the formation of convection cells in Benard's experimental study. Thermal convection (often referred to as Benard–Rayleigh convection) is recognized as the systematic overturning of a fluid layer, when sufficiently and uniformly heated from below and/or cooled from above. This overturning results in an organized geometric pattern of convection cells, often viewed as hexagonal (as in Benard's study) although a wide array of geometric planforms can be achieved under a variety of conditions. Rayleigh's model for thermal convection represents a non–rotating gravitating fluid with constant viscosity ν and conductivity κ initially at rest between two free surfaces, and the assumptions of Boussinesq (1903) which are: (1) the fluctuations in density which appear with the start of motion result principally from thermal (as opposed to pressure) effects, and (2) in the equations for the rate of change of momentum and mass, density variations may be neglected except when coupled with the gravitational force. Applying first–order perturbation theory and the linearizing Boussinesq approximations gives the following form for the momentum, continuity, state and energy equations used in the Rayleigh model:

$$\frac{\partial u}{\partial t} = \frac{-1}{\rho_m}\frac{\partial p}{\partial x} + \nu \nabla^2 u \qquad (1.1)$$

$$\frac{\partial v}{\partial t} = \frac{-1}{\rho_m}\frac{\partial p}{\partial y} + \nu \nabla^2 v \qquad (1.2)$$

$$\frac{\partial w}{\partial t} = \frac{-1}{\rho_m}\frac{\partial p}{\partial z} + \nu\nabla^2 w - \frac{g\rho}{\rho_m} \tag{1.3}$$

$$\frac{\partial u}{\partial x} + \frac{\partial v}{\partial y} + \frac{\partial w}{\partial z} = 0 \tag{1.4}$$

$$\rho = -\rho_m \alpha T \tag{1.5}$$

$$\frac{\partial T}{\partial t} + w\frac{d\overline{T}}{dz} = \kappa\nabla^2 T \tag{1.6}$$

where $\overline{T}$ is the undisturbed temperature, α is the coefficient of thermal expansion, ρ_m is the mean density of the fluid layer and primes have been dropped from the perturbation variables for convenience. In addition, radiation and friction effects have been excluded in the energy equation. After nondimensionalizing the equations, Rayleigh obtained three dimensionless groupings of numbers that appeared in the momentum and energy equations, each describing the characteristics of the fluid. One of these is the Rayleigh number (Ra, a term coined by Chandrasekhar (1957)) which represents the ratio of buoyancy forces and viscous forces:

$$Ra = \frac{g\,\alpha\,\beta\,d^4}{\kappa\,\nu} \tag{1.7}$$

Here g is the acceleration due to gravity, β is the lapse rate of the fluid, d is the convection depth, κ is the thermal diffusivity and ν is the molecular kinematic viscosity. In his theoretical work, Rayleigh showed that a fluid initially at rest when uniformly heated from below will begin to convect above some critical value of the Rayleigh number (Ra_c) which is dependant upon boundary conditions. In Rayleigh's model for free–free boundary conditions, the minimum critical Rayleigh number (min Ra_c) for which convection occurs is for a Rayleigh value of 657.5 at a critical

wavelength (k_c) of 2.221.

Comparisons between Lord Rayleigh's findings and those of Benard revealed a serious discrepancy related to the critical Rayleigh number required for convection to occur. The value of the Rayleigh number was lower for convective onset in Benard's experiments than it was in Rayleigh's model. Eventually Benard suspected that the difference was perhaps a result of the role played by surface tension forces in the convective process since his experiment was with oil of only a few mm depth. Low and Brunt (1925) recognized that the temperature gradients in Benard's experiments were at least tenfold less than that predicted by Rayleigh's theory. Benard (1927, 1928) discussed the role of surface tension as a possible explanation for this discrepancy.

As mentioned above, the critical Rayleigh number for a given fluid is dependent upon the boundary conditions (free–free, rigid–free, rigid–rigid). Jeffreys (1926, 1928) examined cases for rigid–free and rigid–rigid boundary conditions and found successively larger values for Ra_c. For rigid–free boundary conditions Jeffreys found the minimum Ra_c to be 1100.6 and for rigid–rigid conditions he found it to be 1707.7. These minimum critical Rayleigh numbers correspond to critical wavelengths of 2.682 and 3.117 respectively. These results were later confirmed by Pellew and Southwell (1940) in a linear convection model.

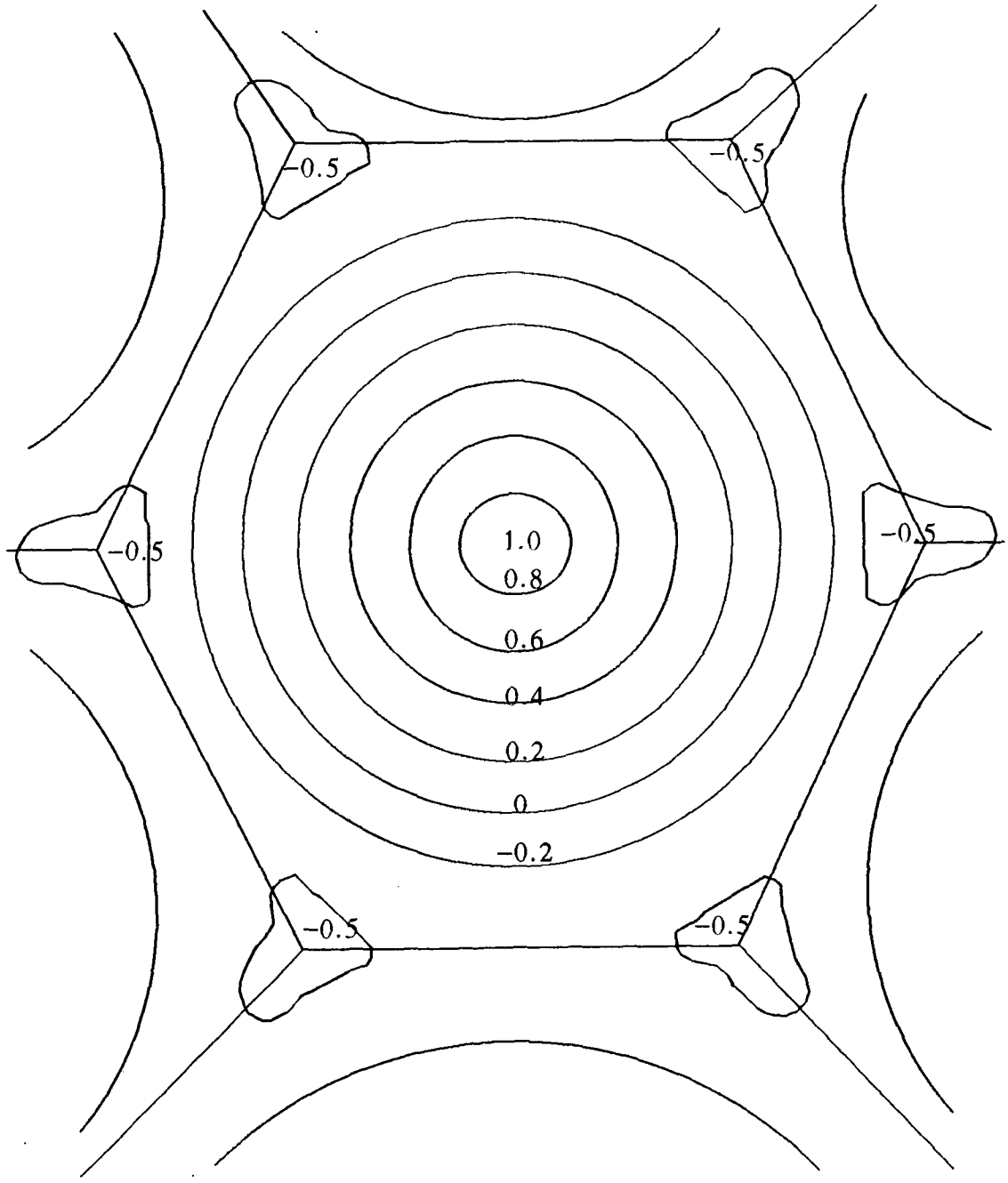

Figure 1.1 Classical linear solution of the relative vertical velocity field in a hexagonal convection cell (from Pellew and Southwell (1940).

1.1.1 Geometric Shape

Since a linear model, as used by Rayleigh, does not yield the geometry of the convective pattern, Rayleigh and his immediate successors were forced to assume a horizontal planform for their models that corresponded to an array of square convection cells. By using Christopherson's (1940) mathematical shape function for a hexagonal array, Pellew and Southwell (1940) were able to re–examine Rayleigh's results for the case of hexagonal cells, as well as for a wider range of boundary conditions. The classical linear solution of the relative vertical velocity field in the hexagonal cell obtained by Pellew and Southwell is shown in Figure 1.1. The zero–valued isopleth is circular with ascending (or descending) motion in the cell center with reversed direction in the periphery of the cell. Extreme values for the relative vertical velocities occur at the corners of the hexagon and at the cell center. Relative velocities at cell center are double those at the corners of the hexagon.

1.1.2 Transitional Patterns

As pointed out by Agee et al (1973), the preferred convective mode is not uniquely determined by the complete set of equations of motion and the boundary conditions if the convecting layer is of infinite horizontal extent. Malkus and Veronis (1958) showed that for convective flows of rectangular and hexagonal structure the infinite number of solutions were of a finite amplitude. They concluded for the case of a rigid boundary and a free surface that hexagons will not appear as the initial instability. However, even though vortex rolls may form initially, the tendency is for a hexagonal form to evolve for a finite range of disturbances. Palm (1960) tried to explain this result theoretically and found the variation in molecular viscosity with temperature, along with its non–linear effects, may be the cause. Segal and Stuart (1962) modified Palm's conclusion saying that hexagonal convection cells may

be the stable solution only when the variation of molecular viscosity with temperature is sufficiently large. As pointed out by Agee et al (1973) two-dimensional convective rolls (e.g. cloud streets) are preferred in a convecting layer with significant vertical shear of the horizontal wind.

Figure 1.2 shows a summary of some of the laboratory and nonlinear theoretical studies carried out by Krishnamurti (1975) for a non-rotating horizontal layer of fluid uniformly heated from below and uniformly cooled from above. The diagram shows the types of flow observed and/or predicted for the ranges of the Rayleigh (Ra) and Prandtl (Pr) number indicated where the Ra is as defined above and the Pr is defined as

$$Pr = \nu / \kappa$$

where ν is the kinematic viscosity and κ is the thermal diffusivity. Along a third coordinate axis is a schematic parameter γ which is a mathematical measure of the vertical asymmetry associated with any one of a number of physical processes that could be imposed. For Krishnamurti's work the γ parameter is representative of the imposed large-scale vertical velocity. The transition points in the diagram depend upon factors such as whether a point is approached from a smaller or larger Ra (i.e. the hypothesis effect) ,uniformity in the cell pattern (Busse and Whitehead, 1974) and imperfections such as curvature and periodicities induced by the sidewall effects (Krishnamurti, 1973). However, in general the horizontal convecting layer is seen to make a slow transition to turbulence. At sufficiently small Ra, the flow is stable to all disturbances. As Ra is increased the flow becomes unstable to one kind of disturbance which grows to finite amplitude. As Ra is increased even further, the flow becomes unstable to more kinds of disturbances. Once Ra is made sufficiently large, the flow is unstable to so

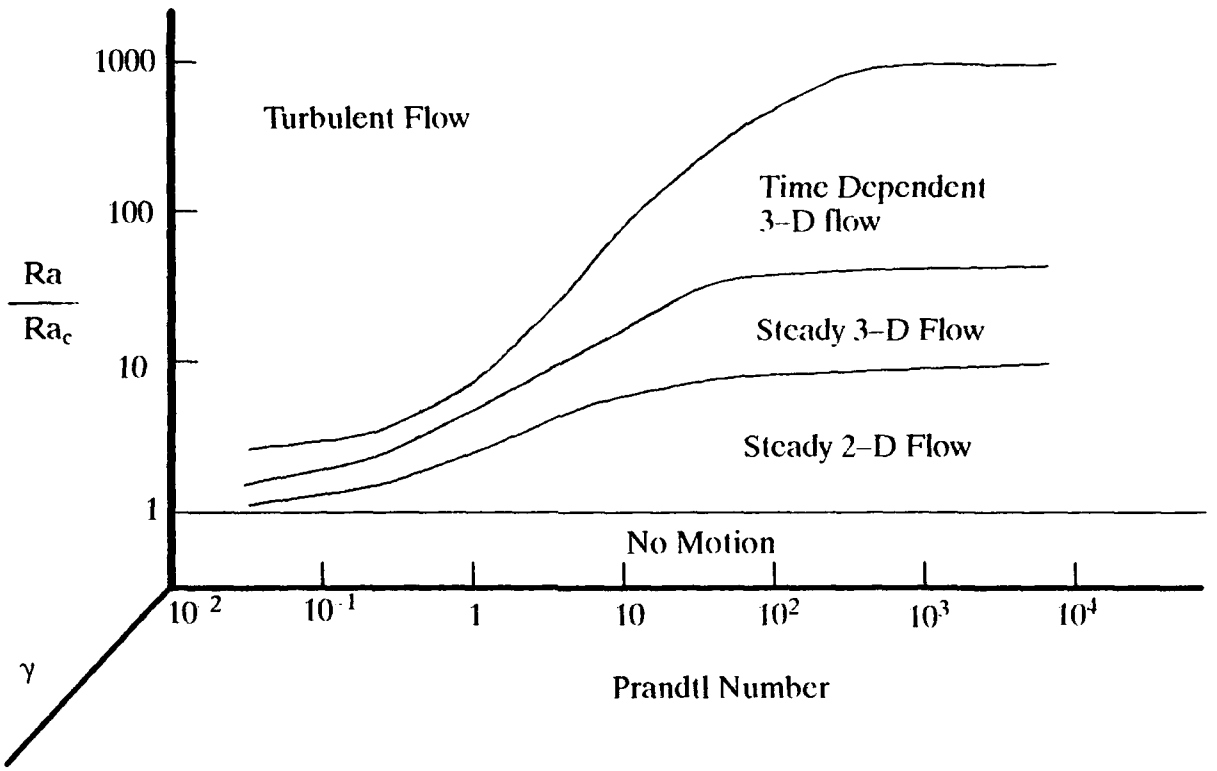

Figure 1.2 Stability regime diagram for the $\gamma = 0$ plane, where γ is a measure of vertical asymmetry. (After Krishnamurti, 1975)

many kinds of disturbances that the resulting flow is called turbulent. Therefore, unlike the "fast" transition seen for Couette flow, the horizontal convecting layer, especially at higher Prantl number, remains in a discrete regime for a finite range of Rayleigh number. Krishnamurti (1976) has also derived the vertical velocity in hexagonal convection, based on nonlinear theory. This hexagonal solution is similar to that by Pellew and Southwell, but it is inscribed within the linear cell and rotated 30°.

1.1.3 Circulation Direction

The convective cells in Benard's experiments had ascending motion at cell center surrounded by descending motion at the periphery. Stommel (1947) postulated that the favored direction of convective circulation involves the smallest frictional loss, and

that convective motion originates in the low viscosity region toward the region of high viscosity. Since the molecular viscosity of liquids usually decreases with increasing temperature but increases for gases, one would expect that liquids initially at rest should develop hexagonal cells with ascending motion at cell center and descending motion in the periphery (i.e. closed cells) For gases, the observed circulation direction should be downward at cell center and upward in the periphery (i.e. open cells). It was Hubert (1966) who adopted the nomenclature of open and closed cells to atmospheric thermal convection observed in convective marine boundary layers. The logic behind the names comes from the occurrence of cloudy centers for closed cells and relatively cloud–free centers for open cells.

Based on the discussion given above, one might expect to see only open cells during atmospheric manifestations of Benard–Rayleigh convection. However this clearly is not the case. For instance, Rothermel and Agee (1980) have documented the coexistence of both open and closed cells during the Air–Mass Transformation EXperiment (AMTEX) over the East China Sea. Tippleskirch (1956) attempted to investigate the possible role played by the vertical variation of molecular viscosity on the circulation direction in a Benard–Rayleigh cell by performing laboratory experiments with molten sulfur. Tippleskirch chose molten sulfur because it behaves like a liquid in the temperature range of 110°C to 153°C with decreasing molecular viscosity with increasing temperature, but behaves like a gas in the range of 153°C to 200°C with increasing molecular viscosity with increasing temperature. In his experiment , Tippleskirch had closed cells with the molten sulfur in the range of 110° C to 153°C but observed a transition in the circulation direction pattern to open convection cells in the range of 153°C to 200°C. Further studies by Palm (1960) and Segal and Stuart (1962) give additional support to the idea that temperature–produced changes in the molecular viscosity may determine the direction of circulation in laboratory convection.

Within the atmosphere, however, the transport of heat, momentum and moisture is dominated by the effects of eddy motions and not molecular viscosity and conductivity. Based upon the mathematical solution of a free convection model for the atmosphere used in conjunction with Stommel's physical argument, Agee and Chen (1973) showed that the sign of the change in eddy viscosity with height can fix the direction of circulation in cellular convection. Or, more specifically, if the eddy viscosity is increasing (decreasing) with height, an unstable layer of cellular convection will have open (closed) cells. They go on to emphasize that the mathematical solution only proves a circulation reversal if the sign of the vertical gradient of eddy viscosity changes, and that Stommel's physical argument is necessary to determine the circulation direction. Krishnamurti (1975) later proposed that the circulation direction in mesoscale cellular convection (MCC) is related to the upward and downward large–scale vertical motions with closed (open) cells forming in regions of large–scale up motion (down motion). Van der Borght (1975) proposed that a stronger heat flux from the sea to the atmosphere should occur in regions of open cells than in regions of closed cells. All of these studies suggest that many different processes can affect or even alter the direction of circulation in a pattern of cells.

1.1.4 The Type I vs. Type II CTBL

While there are certainly more than just two types of cloud–topped boundary layers (CTBLs) (see Agee, 1987), the Type I or cold–air outbreak CTBL and the Type II or marine stratocumulus CTBL are particularly significant in the earth's atmosphere. The Type I CTBL is a thermally–driven convective boundary layer that forms when cold air moves over relatively warmer water. The Type I typically forms during the winter off the east coast of continents over warm ocean currents and south or north of the respective ice caps. Two particularly common regions for the formation of the Type I CTBL are off the east coast of the United States over the Gulf Stream and off

the East China coast over the warm waters of the Kuroshio current. The two case studies used for comparison in this paper were conducted in these areas and will be discussed in greater detail in Chapter 3. The Type I CTBL tends to form very quickly (< 24 hours) and may persist for 2 – 5 days. The cloud species formed in the wake of the cold–air outbreak accompanying the Type I CTBL are of the cumulus and stratocumulus variety with the geometry varying from 2–d rolls (i.e. cloud streets) to 2–d and 3–d chains or 3–d open and closed MCC.

The Type II CTBL is in many ways the antithesis of the Type I. It tends to form over water surfaces with temperatures comparable to that of the air above. The primary driving mechanism is cloud–top radiative cooling. Type II CTBLs tend to form in the summer to the west of continents over cool ocean currents and, although they are relatively slow to form, they may persist for several weeks, with diurnal variation caused by radiative–entrainment effects. One of the especially favored regions for the formation of the Type II CTBL is off the west coast of California as evidenced by expansive layers of stratocumulus during the summer in this area.

Both the Type I and Type II CTBLs are characterized by weak wind shear and negative large–scale vertical velocities which act to reduce the depth of the CTBL. Discussion in this thesis will focus entirely on the Type I CTBL.

Figure 1.3 shows the vertical profile of potential temperature for the typical Type I CTBL. The lowest layer of the CTBL is the superadiabatic surface layer which results from the very cold air coming in contact with the relatively warm waters below. Above this layer is the well–mixed layer which includes the neutral (dry) subcloud layer and the neutral (moist) cloud layer. Above this is typically found the inversion layer, including the transition layer through which entrainment occurs, above which is found the undisturbed inversion layer and finally the free atmosphere.

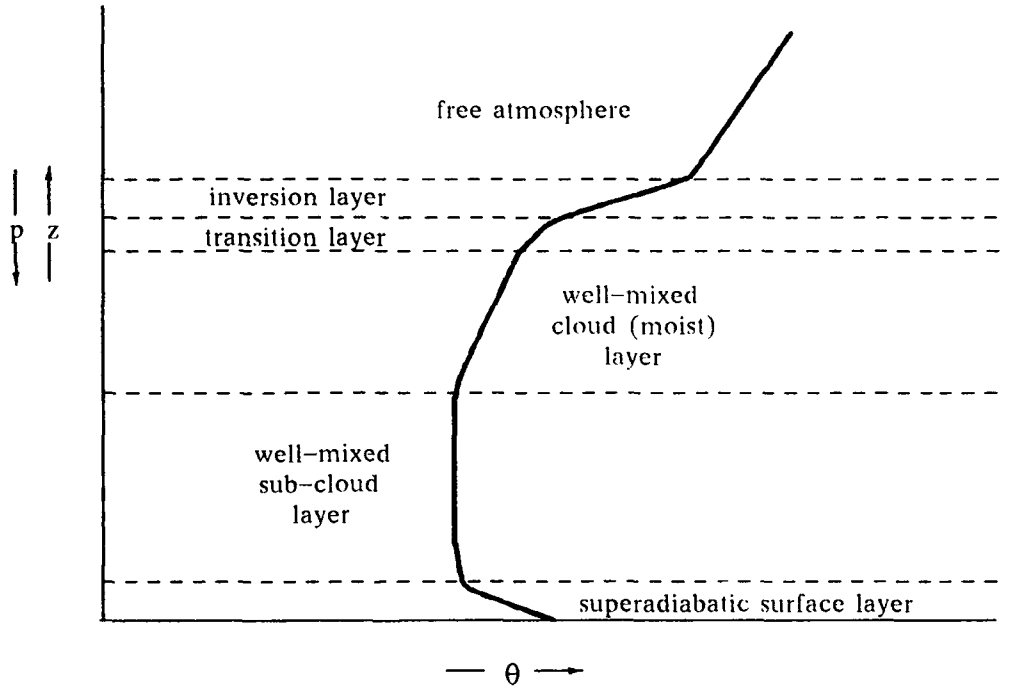

Figure 1.3 Vertical profile of potential temperature for a Type I CTBL which includes the transition layer where penetrative convection occurs (from Agee and Gilbert, 1989).

1.1.5 Heat Flux

Cold air outbreaks (CAOs) over regions favorable to MCC formation such as the East China Sea over the Kuroshio Current and off the East Coast of the United States over the warm waters of the Gulf Stream result in total heat fluxes (sensible and latent heat) that approach that of the solar parameter (1380 W m $^{-2}$). These large energy fluxes in turn are capable of influencing large-scale flows and may provide a mechanism for providing energy for cyclogenesis to occur (Agee and Howley, 1977). Sheu and Agee (1977) showed that a sensible heat flux of 70 Wm $^{-2}$ and total heat flux of 200 Wm $^{-2}$ were necessary conditions for the formation of MCC. They also found that both open and closed cells occurred during the Air Mass Transformation EXperiment (AMTEX)

conducted over the East China Sea when the sea to air energy flux (latent plus sensible) was either strong ($\sim$ 1200 Wm^{-2}) or weak ($\sim$ 200 Wm^{-2}). Previously, Agee and Dowell (1974) had observed that strong heat flux from the sea to the atmosphere occurs in regions of open cells and a weaker flux from the ocean to the air in regions of closed cells. Hubert (1966) inspected a large number of MCC cases and observed that open cells can exist under conditions of both strong and weak surface heating while closed cells tend to exist only with small surface heating. A plausible explanation for Hubert's finding is that open cells may be more efficient at transporting heat than closed cells since strong downward motion occupies most of the open cell and continues to provide cold air to the sea surface and thus enhances the air–sea interaction (Sheu and Agee, 1977). This theory is supported at least partially by the observance of penetrative MCC exclusively for the open cells; indicative of a more vigorous ascending branch in the convective cell.

1.2 Statement of Research Goals and Objectives

Data collected over Lake Michigan as part of Project LESS have been used in this thesis research to increase the understanding of convection in a Type I CTBL. In particular, results from the 10 January 1984 case are examined closely to study transport processes in a convective marine boundary layer. Statistics including means, variances, covariances and skewness values have been determined in the hope of increasing the conceptual understanding of the structure of Type I CTBLs. To achieve this objective, the following specific research goals were set and have been achieved:

1. Establish a unique data set in a homogeneous region of a Type I marine CTBL over which turbulent statistics can be calculated.

2. Calculate the turbulent statistics associated with the heat, momentum and moisture budgets for a Type I CTBL (Project LESS) using both detrended data (i.e.

$\overline{w} = 0$) and raw data $\overline{w} \neq 0$.

3. Compare and contrast the turbulent statistics for the 10 Jan 84 case of Project LESS with other analogous observational case studies from AMTEX and MASEX, and with model results by Deardorff (1980) and Moeng (1984), with the goal of explaining physically the similarities and differences of these convective events.

4. Investigate the role played by the release of the latent heat of condensation in the upper portion of the convective marine boundary layer.

5. Compare select conventional (i.e. detrended) data results with non-conventional (i.e. raw) data results.

2. PROJECT LESS

2.1 Background

Anyone who has lived in the vicinity of the Great Lakes is well aware of the profound impact that these bodies of water have upon the weather in this region. One of the most obvious of these impacts is the lake–induced snow storms which occur when polar air masses move southward out of Canada over the relatively warm waters of the Great Lakes. This often results in substantial increases in the amount of snowfall at locations along the downwind shores.

Braham and Dungey (1984) have investigated snowfall patterns around Lake Michigan and along the south shore of Lake Superior for the winters of 1909/10 through 1980/81 with the goal of quantitatively estimating the effect of Lake Michigan on snowfall. They have estimated the lake effect by taking the ratio of observed to predicted snow amount for four different areas in Wisconsin and Michigan and found the long–term (70 year) average effect along the west shore (south of Sheboygan, Wisconsin) was about 10% compared with roughly 60% along the east shore (south of Hart, Michigan). Charnon (1968) estimated lake effects on total winter precipitation for the period 1921 –51 and found the average effect along the west shore to be about 5% and and up to 30% in the snowbelt regions of southwest lower Michigan. Dewey (1970) concluded the lake effect increases the annual snowfall along the Wisconsin shore by 30–40% while some areas in western lower Michigan receive about 200% more snow than stations at a comparable latitude but inland, away from the lake effect.

The Lake Effect Snow Studies (LESS) Project was conducted during the winter

of 83–84 by the University of Chicago Cloud Physics Group, the National Center for Atmospheric Research (NCAR) and the Purdue University Mesoscale Convection Research Group. The study ran from 1 December 1983 – 28 January 1984. The objectives of the study included the study of cold air outbreaks and resulting modification of the polar air that passed over both Lake Superior (northerly flow cases) and Lake Michigan (both northerly and westerly flow cases). Included is an analysis of convective PBLs and lake–effect snow systems. The Chicago Cloud Physics Group focused mostly on westerly flow cases; the Purdue group on northerly flow cases. Routine observations by the National Weather Service and the Canadian Atmospheric Environment were supplemented by the NCAR Portable Automated Mesonet (PAM II) and special rawinsonde stations manned by both the Chicago and Purdue research groups. Data were collected over Lake Michigan at roughly 43°N by NCAR's King Air (flight level 5) and Queen Air (flight levels 1 – 4) aircraft with a total of 15 missions flown. This particular research has focused on the data collected on 10 January 1984 between 1812 and 1959 UTC for a northerly flow case. Figure 2.1 shows the vertical profile for NCAR aircraft flights for the 10 January 1984 case. The Queen air flew at flight levels 1 – 4 while the King Air flew level 5. From Figure 2.1 it is noted that the King Air flew through the inversion layer (marked by A), the interfacial layer (B) and the mixed layer (C) as it flew from west to east. The Queen Air also flew through a portion of the interfacial layer at level 4. The environment of the interfacial or transition layer is characterized by warm, dry air from the inversion layer mixed with the cool, moist air from the convective region by entrainment or penetrative convection. While these regions were a focus of the work done by Agee and Gilbert (1989), for the work done in this study it was desirable to obtain turbulent statistics over as homogeneous a region as possible. This led to the selection of a "hand–picked" data set which not only eliminated as much as

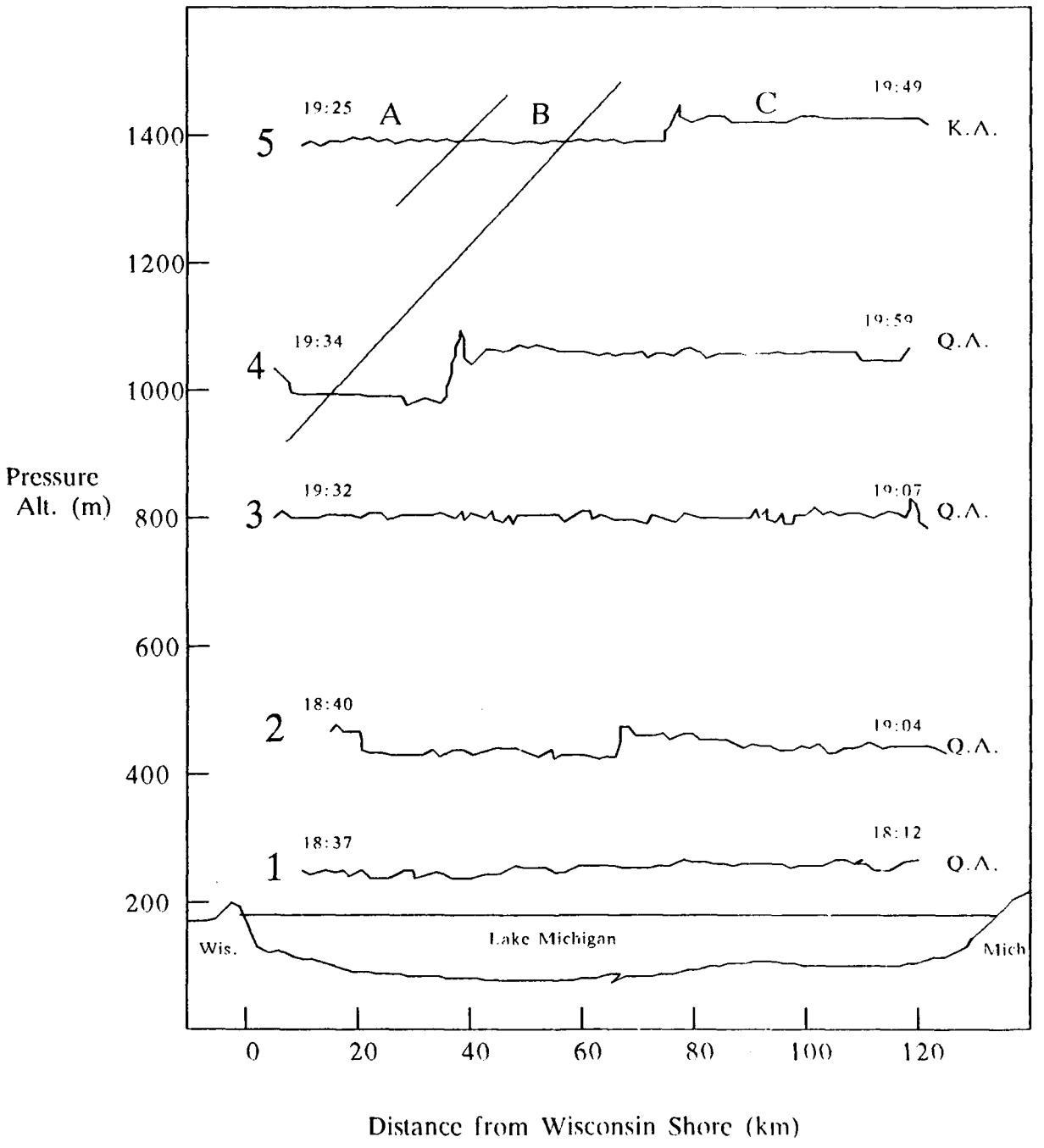

Figure 2.1 The five flight levels of the NCAR Queen Air and King Air aircraft from 1812 to 1959 UTC for the cold air outbreak of 10 January 1984 (from Agee and Hart, 1990)

possible the effects of the interfacial and inversion layers but also the effects of the Michigan and Wisconsin land breezes which were detected at levels 1 and, to a lesser degree, at level 2. This "hand-picked" data set will be discussed in more detail in the section on data analysis techniques. Since the 10 Jan 84 case represented a northerly flow event, by flying from west to east (or vise versa) the aircraft were able to make data measurements along a path that was transverse with respect to the orientation of the three-dimensional convective cloud bands present in the flow.

2.2 Synoptic Discussion

CAO events are of interest to the meteorologist because of the frequent dramatic drop in temperature that results from their occurrence and the often times severe disruptions to man's activities in the affected regions. This disruption may be especially acute in the Great Lakes areas because of the significant lake-induced clouds and snow that often times accompany such events. As pointed out by Konrad and Collucci (1989) such CAO events are generally associated with a surface anticyclone-cyclone couplet between which a southward transport of cold air occurs from a high latitude source region. Zishka and Smith (1980) have studied the climatology of cyclones and anticyclones using a 2° latitude/longitude grid spanning North America and surrounding ocean waters for January and July 1950 – 1977. They determined areal distributions of cyclones/anticyclone events, genesis, decay, relative variability and preferred propagation tracks. For the January case, anticyclogenesis generally occurs over the snow and ice fields from Montana through the Northwest Territories or in the central United States from South Dakota to Texas, often south of the jet stream. Using Wexler's classification(1951), these two types of anticyclones appear to be of the "cold" and "warm" anticyclone class, respectively. From their analysis, Zishka and Smith determined four preferred propagation tracks for January anticyclones (see figure 4d in their paper). One of the preferred tracks originates from

the Northwest Territories and then splits into two distinct tracks over Manitoba. One branch continues southward and then turns eastward through the midwestern United States. The other branch turns directly to the east through Ontario and Quebec. The CAO event that occurred during Project LESS on 10 Jan 84 was of the first type; a southward moving anticyclone that eventually turned eastward.

As pointed out by Wexler (1943), as a polar high moves southward, the cold air warms because of subsidence and surface heating. Since this cold layer shrinks in depth and covers an increasingly larger area, it typically decays. This was the case for the CAO event of 10 Jan 84. Behind the leading cold front at 12Z on 9 Jan 84, a strong high pressure (cp 1044mb) to the lee of the Canadian Rockies moved southeastward into Montana and North Dakota. By 12Z on 10 Jan 84, the cold anticyclone was centered over northern Minnesota (cp 1040 mb) creating a light to moderate north–northwesterly flow over Lake Michigan. By 12Z on the 11th, the anticyclone had moved southward over northern Illinois and had weakened an additional 8 mb to approximately 1032 mb.

Only a brief account of the synoptic situation has been given here; those interested in a more thorough synoptic discussion are referred to Agee and Gilbert (1989). Especially noteworthy is Figure 4 in the above mentioned article, which shows a streamline analysis for both the surface and 850mb level flow. From this figure it is clear that the polar air moving over Lake Michigan analyzed during Project LESS had already been warmed as it passed over the relatively warmer waters of Lake Superior.

As part of their examination of extreme CAOs over eastern North America, Konrad and Colucci (1989) did the following analysis. Temperatures at the 850mb level from cold seasons (1 December through 28 February) during the period 1 January 1976 – 31 December 1985 were extracted from reports for 20 stations within

the area bounded by the 30° and 50°N parallels and 75° and 90°W meridians (note that the Project LESS operational area is included in this bounded region). The temperatures were then averaged over the stations at 1200 UTC each winter season day of the 10 year period, thus providing a regional mean temperature $\overline{T}$. Results indicated a mean temperature for the period in question of −1.7°C and a standard deviation of 5.9°C. The Purdue Regional Objective Analysis of the Mesoscale (PROAM) and its upper air counterpart (PROAMU) over this same area gives a rough estimate of the 850mb temperature during the 10 Jan 84 CAO of about −12°C (approximately −15°C over the LESS area), nearly two standard deviations from the mean, qualifying this event as a strong if not extreme CAO event.

2.3 Data Analysis Procedures

As mentioned previously in section 2.1 above, for purposes of this study it was desirable to examine a portion of the convectively mixed layer over the middle of Lake Michigan not affected by the land breeze or inversion layer phenomena. The resulting "hand–picked" data set provides results that can be compared with numerical model simulations of convective boundary layers and other relevant observational data sets such as were collected during the AMTEX and MASEX. As noted earlier, the overall objective of this study has been to gain a more thorough understanding of the convective transport phenomena and associated turbulence statistics. The meteorological parameters of interest for this study include the following 20Hz data: u, v, w wind components (m/s), virtual potential temperature, Θ_v (°K) and specific humidity q (g/kg). The data set selected for this study included data collected from 45–75km from the Wisconsin shore at all five vertically stacked levels. This 30km flight leg was in turn divided into 2–15km flight legs for which convergence in the convective turbulent statistics was checked. *It took 1 hour and 47 minutes* for the NCAR King and Queen Air aircraft to collect the data used in this study.

The table below gives specifics about the five flight legs flown. The heights indicated below are meters above mean sea level which are easily converted to heights above lake level by subtracting 160 meters. It is clear from the data shown below that the aircraft did not maintain a constant speed as they flew across the lake, with flight level 5 flown the fastest by the King Air and flight level 1 flown the slowest by the Queen Air. Clearly there is more than a sufficient number of observations for each flight segment to calculate meaningful turbulent statistics and skewness values.

Table 2.1 Characteristics of the flight paths flown by the King Air and Queen Air aircraft for the 10 January 1984 cold air outbreak during the Project LESS.

45 – 75 km Flight Legs

Level	Height (m)	Heading	Number of Obs	Speed (m/s)	Elapsed Time (s)
5	1392	west–east	7969	75.29	398.45
4	1090	west–east	8441	71.08	422.05
3	800	east–west	8063	74.41	403.15
2	480	west–east	8256	72.67	412.80
1	210	east–west	8683	69.10	434.15

45 – 60 km Flight Legs

Level	Height (m)	Heading	Number of Obs	Speed (m/s)	Elapsed Time (s)
5	1392	west–east	3938	76.18	196.90
4	1090	west–east	4230	70.92	211.50
3	800	east–west	4067	73.76	203.35
2	480	west–east	4143	72.41	207.15
1	210	east–west	4293	69.88	214.65

60 – 75 km Flight Legs

Level	Height (m)	Heading	Number of Obs	Speed (m/s)	Elapsed Time (s)
5	1392	west–east	4031	74.42	201.55
4	1090	west–east	4211	71.24	210.55
3	800	east–west	3996	75.08	199.80
2	480	west–east	4113	72.94	205.65
1	210	east–west	4390	68.34	219.50

The 20Hz data for the convective mixed layer have been detrended using a second degree polynomial in order to remove any synoptic scale or large mesoscale signal. Wilczak and Businger (1983) show there is little difference between linear and quadratic detrending when compared to the variability when no detrending is used. The data were detrended using the International Mathematical and Statistical Library (IMSL) subroutine call RLFOTH which fits a univariate curvilinear regression model using orthogonol polynomials. The model used for the multiple regression is,

$$y = B_0 + B_1x + B_2x^2 + \epsilon \qquad (2.1)$$

where y is the value for the given weather variable (u, v, w, Θ_v, or q); x is the distance from the Wisconsin shore in meters; B_0, B_1 and B_2 are the true coefficients for the slope and x terms in the equation; and ϵ is the random error, which is assumed to have a normal distribution with a mean of zero and a variance of σ^2. Each flight segment was detrended separately; i.e. the 45 – 75 km, 45 – 60 km and 60 – 75 km segments were each detrended using a second order model of the form indicated above. The value for y–hat, the estimated value for y in the model shown above, was obtained using the IMSL routine RLOPDC which gives a response prediction using an orthogonal polynomial regression model. The y–hat value obtained for each x value was then subtracted from the raw data values for each variable to get a detrended value for that variable. The 1 Hz specific humidity data were used to calibrate the 20 Hz Lyman–Alpha data according to the method of Friehe et al. (1986) before they were detrended. The IMSL routine RLDOPM was used to transform the polynomial regression model, fitted using orthogonal polynomials, into a polynomial function of the original independent variable. The resulting y–intercept

and coefficients of the x and x^2 terms in the regression equation are shown in Table 2.2 below.

Table 2.2 Y–intercepts and x–term coefficients from 2nd degree polynomial detrending process.

45 – 75 km Flight Legs

Flt Level		Intercept	x–term coeff	x^2–term coeff
u	5	20.0028	-7.0825E-04	5.2348E-09
	4	-9.1543	3.2419E-04	-2.9159E-09
	3	1.7712	-7.8785E-05	8.0508E-10
	2	7.5159	-2.0955E-04	1.5275E-09
	1	22.7080	-8.0340E-04	6.9954E-09
v	5	37.1980	-1.4763E-03	1.1955E-08
	4	-20.0785	4.5535E-04	-3.4741E-09
	3	1.6142	-3.0904E-04	2.5595E-09
	2	-0.8622	-2.7817E-04	2.6231E-09
	1	-13.1880	1.4498E-04	-8.4877E-10
w	5	0.8926	-3.1054E-05	2.3476E-10
	4	14.3260	-4.7651E-04	3.9139E-09
	3	5.9528	-2.1169E-04	1.9221E-09
	2	-14.3981	4.8874E-04	-4.0054E-09
	1	-0.5993	1.8143E-05	-1.4997E-10
θ_v	5	297.1423	-9.5357E-04	7.2580E-09
	4	266.0135	-5.8769E-05	6.4514E-10
	3	263.2163	3.5901E-05	-5.2169E-11
	2	261.2700	9.5538E-05	-5.2510E-10
	1	263.9518	8.3481E-06	1.4985E-10
q	5	-8.1946	2.7406E-04	-2.0326E-09
	4	1.5173	-1.2223E-05	1.1767E-10
	3	0.9159	1.0420E-05	-6.7952E-11
	2	-0.9655	8.1903E-05	-7.0657E-10
	1	-0.4688	6.4444E-05	-5.7129E-10

45 – 60 km Flight Legs

Flt Level		Intercept	x–term coeff	x^2–term coeff
u	5	82.2350	-3.2246E-03	3.0544E-08
	4	71.6853	-2.7262E-03	2.5588E-08
	3	-29.4856	1.1109E-03	-1.0434E-08
	2	-67.6509	2.6313E-03	-2.5006E-08
	1	85.7552	-3.2563E-03	3.0703E-08
v	5	43.0201	-1.7271E-03	3.0544E-08
	4	71.6853	-2.7262E-03	2.5588E-08
	3	-29.4855	1.1109E-03	-1.0434E-08
	2	-6.7650	2.6313E-03	-2.5006E-08
	1	85.7552	-3.2563E-03	3.0703E-08
w	5	12.9967	-5.1703E-04	5.0869E-09
	4	54.1998	-2.0239E-03	1.8827E-08
	3	8.8863	-3.311E-04	3.1325E-09
	2	17.4669	-7.5701E-04	8.0987E-09
	1	-3.4638	1.3421E-04	-1.3061E-09
u	5	20.0028	-7.0825E-04	5.2348E-09
	4	-9.1543	3.2419E-04	-2.9159E-09
	3	1.7712	-7.8785E-05	8.0508E-10
	2	7.5159	-2.0955E-04	1.5275E-09
	1	22.7080	-8.0340E-04	6.9954E-09

Table 2.2, continued

Flt Level		Intercept	x–term coeff	x^2–term coeff
θ_v	5	288.7123	-5.9435E-04	3.4679E-09
	4	263.4219	5.0274E-05	-2.5892E-10
	3	266.7917	-1.0439E-04	1.3138E-09
	2	263.5610	5.6955E-06	3.5349E-10
	1	254.5918	3.6696E-04	-3.2567E-09
q	5	-11.7678	3.9910E-14	-3.0973E-09
	4	4,3957	-1,2904E-04	1.2950E-09
	3	3.9764	-1.1014E-04	1.1089E-09
	2	-4.2502	2.1418E-04	-2.0709E-09
	1	3.3737	-9.2839E-05	1.0666E-09

60 – 75 km Flight Legs

Flt Level		Intercept	x–term coeff	x^2–term coeff
u	5	-3.8999	-1.2454E-04	1.7837E-09
	4	103.6111	-2.9118E-03	2.0228E-08
	3	89.5051	-2.6908E-03	2.0163E-08
	2	-82.5159	2.3678E-03	-1.6860E-08
	1	28.7860	-9.9707E-04	8.5115E-09
v	5	135.9280	-4.4188E-03	3.3784E-08
	4	-6.4134	8.4201E-05	-1.1121E-09
	3	15.8231	-7.2665E-04	5.6214E-09
	2	-93.5781	2.6258E-03	-1.9881E-08
	1	-49.0781	1.2654E-03	-9.5103E-09
w	5	-11.9270	3.2768E-04	-2.2679E-09
	4	29.8591	-9.3929E-04	7.3418E-09
	3	-13.7750	3.6363E-04	-2.2592E-09
	2	-24.5864	7.7559E-04	-6.0215E-09
	1	26.1639	-7.6607E-04	5.5838E-09
θ_v	5	286.3911	-5.9921E-04	4.3983E-09
	4	277.3638	-3.9257E-04	3.2123E-09
	3	264.7012	-1.0140E-05	2.9978E-09
	2	272.2513	-2.2991E-04	1.8779E-09
	1	268.3663	-1.2622E-04	1.1706E-09
q	5	-25.4329	7.6503E-04	-5.5169E-09
	4	4.9283	-1.1439E-04	8.7670E-10
	3	4.5469	-1.0228E-04	7.8075E-10
	2	1.9937	-1.3577E-05	5.5091E-11
	1	18.8223	-5.1378E-04	3.7675E-09

After the data sets have been detrended for each meteorological variable, each value represents a residual (i.e. the difference between the true and predicted value). For any regression, simple linear or multiple, the residuals must sum to zero regardless of the goodness of the fit. As a result, the means for each detrended variable must also be zero. Table 2.3 gives the averages for all 5 weather variables for the

3 different flight segments used in this study. The ratio Z/Z_i is the ratio of the actual aircraft height to that of the mixed layer as determined by the mean height of the base of the inversion for each flight segment. The mean inversion heights for the 45–75 km, 45–60km and 60–75 km flight legs were 1240m, 1140m and 1340 m respectively. Note that in the table, averages are not given at level 5 for the 45–75km leg because this flight path represent samples from both the convective mixed layer and the interfacial layer. Averages are given for the 45–60km and 60–75km legs because the former, at least for the most part, represents a sample from the interfacial layer and the latter from the convective mixed layer. Also, two independent neighboring samples allow one to see to what extent the same results can be produced from within the homogeneously selected region.

2.3.1 U and V wind component Data

Figures 2.2 and 2.3 show the plots of raw 20Hz U and V wind components (m/s) for the five vertically stacked flight levels from 45 – 75 km with positive (negative) values representing westerly (easterly) winds for U and southerly (northerly) winds for V.

The plots of the u–component of wind in figure 2.2 show that the east–west component was quite weak with speeds generally less than 3 m/s. The strong land breeze detected by Agee and Hart (1990) extending from lower Michigan out to around 95 km at levels 1 and 2 is excluded from this "hand–picked" data set. The weaker Wisconsin land breeze that extended out to about 22 km from the Wisconsin shore at level 1 is also no longer evident. The plot of the u–component of wind at level 5 indicates a more easterly component to the wind than at any other flight level. There is also some evidence of a transition from the interfacial layer (roughly 40–60km from the Wisconsin shore), where the winds are quite variable,

Table 2.3 Weather variable averages for the 45–75km, 45– 60km and 60–75 km flight segments.

Boundary Layer Averages

Averages (45 – 75 km)

Flight

Level	Z/Zi	Avg U	Avg V	Avg W	Avg Θv	Avg q
5	(Convective and non-convective data not averaged)					
4	0.7500	-0.4188	-6.2302	0.1182	265.4490	1.2180
3	0.5161	0.0019	-7.5212	0.3139	265.1688	1.2914
2	0.2581	0.5592	-7.9129	0.2035	265.0765	1.3516
1	0.0403	0.2170	-7.6043	-0.0220	265.0095	1.4172

Averages (45 – 60 km)

Flight

Level	Z/Zi	Avg U	Avg V	Avg W	Avg Θv	Avg q
5*	1.0807	-2.3028	-7.0894	-0.0307	267.1346	0.6023
4	0.8158	-0.4371	-6.6398	0.1900	265.3432	1.2149
3	0.5614	-0.1168	-7.5353	0.1946	264.9538	1.2730
2	0.2807	0.9336	-8.5297	0.1898	264.8338	1.3806
1	0.0439	-0.0003	-8.0489	-0.0419	264.8147	1.4536

Averages (60 – 75 km)

Flight

Level	Z/Zi	Avg U	Avg V	Avg W	Avg Θv	Avg q
5	0.9194	-4.1473	-7.8013	-0.1836	266.0633	0.9783
4	0.6940	-0.4003	-5.8188	0.0461	265.5553	1.2210
3	0.4776	-0.1228	-7.5069	0.4353	265.3876	1.3102
2	0.2388	0.1820	-7.2916	0.2172	265.3209	1.3227
1	0.0373	0.4294	-7.1697	-0.0022	265.2000	1.3816

* Level 5 is above the convective PBL.

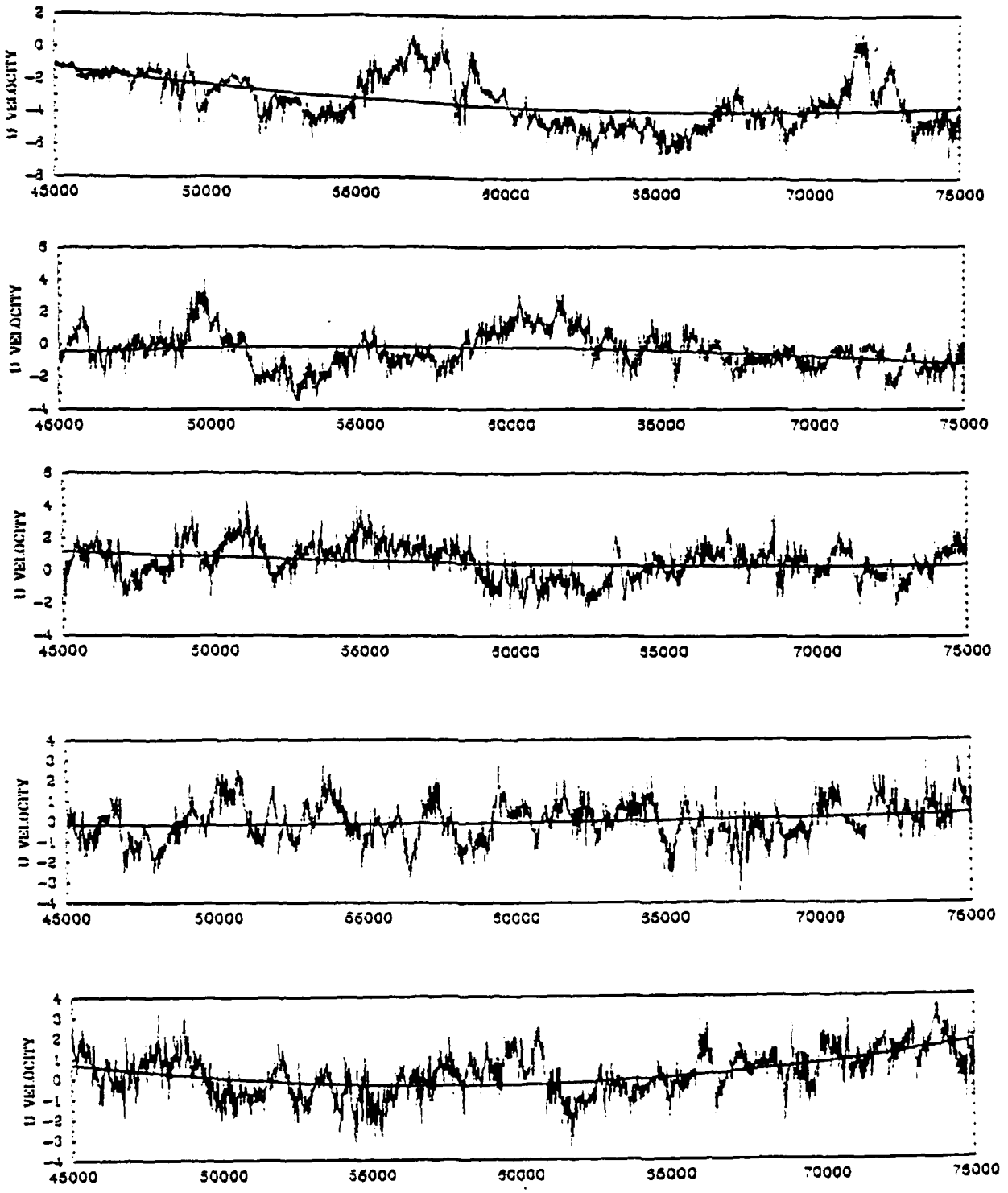

Figure 2.2 Plot of raw 20Hz u wind component (m/s) for flight levels 1 (bottom) through 5 (top) with detrend curve overlayed.

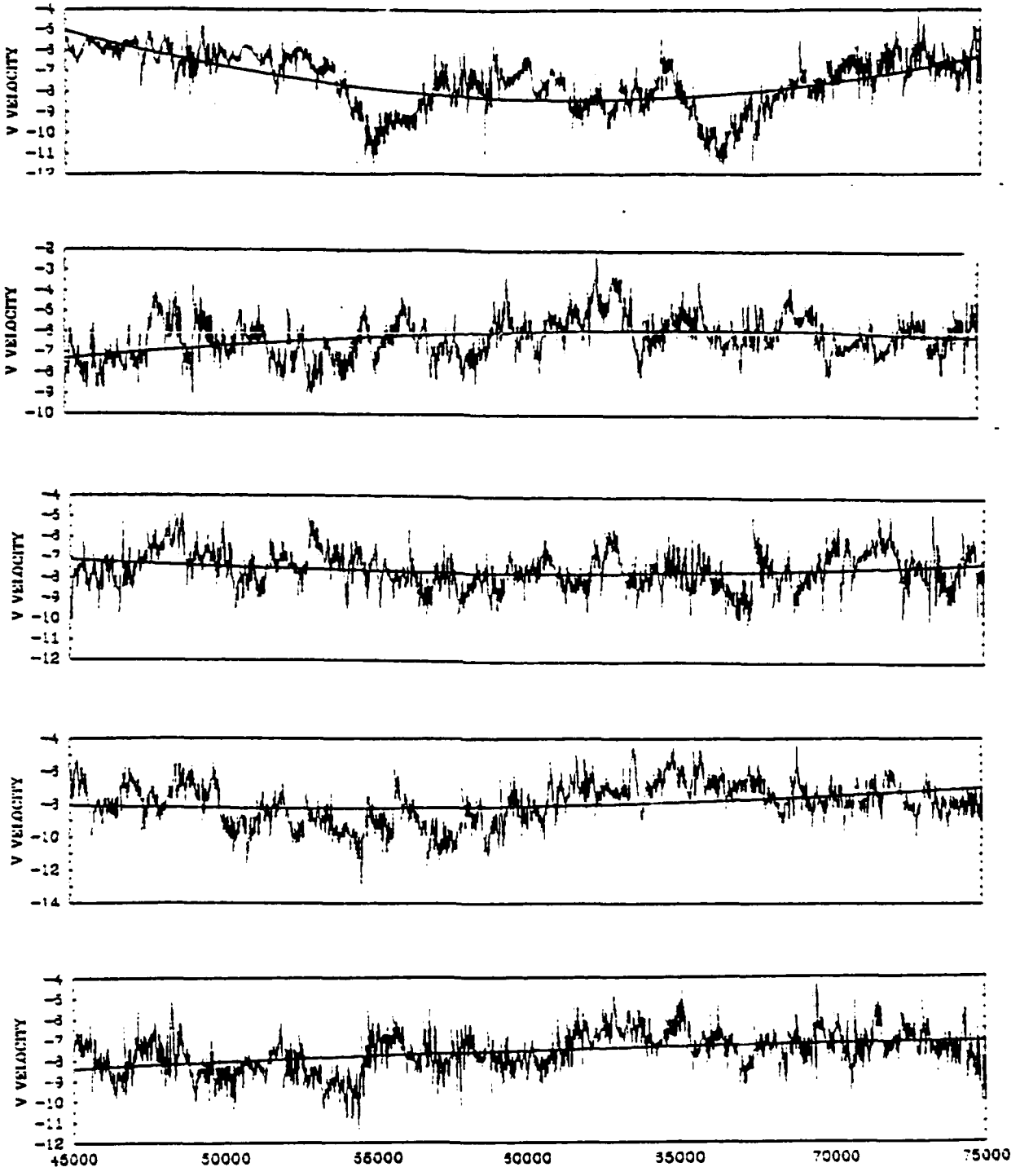

Figure 2.3 Plot of raw 20Hz v wind component (m/s) for flight levels 1 (bottom) through 5 (top) with detrend curve overlayed.

to the convective mixed layer, where, with the exception of of a segment from 72 – 74 km from the Wisconsin shore, the winds are steady at 4 to 5 m/s. The u–component of wind for levels 1 through 4 show much more frequent oscillations between weak westerly and easterly momentum than is evident at level 5. Levels 1 and 5 show the greatest synoptic and large–mesoscale trend. There is also strong evidence of a convergence band or zone at approximately 61 km from the Wisconsin shore at level 1 where there is an abrupt change from westerly (positive) to easterly winds (negative). It is worth noting that the 45–75km segment at flight level 4, does not include the interfacial layer.

The plots of the raw v–component of wind in figure 2.3 show very clearly that the 10 Jan 84 CAO was a northerly flow event with the northerly component of wind typically 2 to 3 times stronger than the u–component. The transition from the interfacial layer to the convective mixed layer at level 5 is less evident in the v–component, with the 2–15km segments appearing as mirror images of one another. Interestingly, the strongest northerly winds appear to occur over the western portion of the 45–75km leg especially at flight levels 1 and 2 (see Table 2.3 above). The only flight level for which this does not hold is level 5 which is influenced by the interfacial layer. Flight level 4 consistently had the lightest winds for the three flight segments.

2.3.2 W wind component Data

Figure 2.4 shows the plots of the raw 20Hz w–component of wind for the vertically stacked 45–75km segment flight paths. A very striking feature at level 5 in this figure is the strong peak in the vertical velocity at approximately 57km from the Wisconsin shore marking the transition from the interfacial layer to the convective

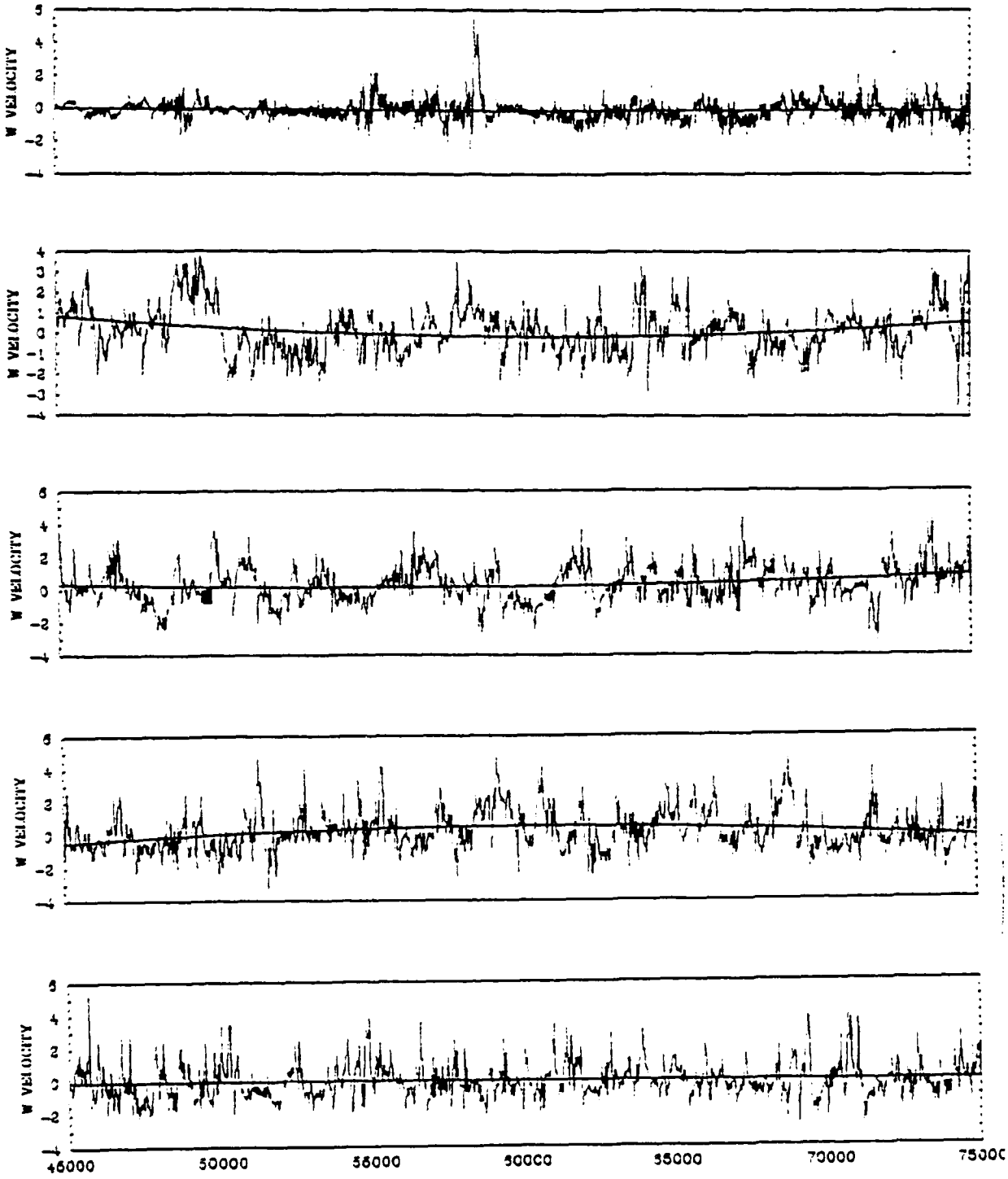

Figure 2.4 Plot of raw 20Hz w wind component (m/s) for flight levels 1 (bottom) through 5 (top) with detrend curve overlayed.

mixed layer. In general, vertical velocities at level 4 are the weakest (1 – 2 m/s). The average vertical velocity for level 5 is negative, indicating weak subsidence at this level. For levels 2, 3 and 4 (within the subcloud and cloud layers respectively) the average vertical velocity is weakly positive (0.2 – 0.4 m/s), while for level 1 it is very weakly negative (−0.002 – −0.04 m/s). The accuracy of w and all other variables measured is presented in the next section (see Table 2.4). The w−component at flight level 1 supports the possibility of a convergence band in the vicinity of 61km from the Wisconsin shore with strong upward motion (+3.5 m/s) in this area. Very little trend is found in the w−component of wind especially at levels 1, 3 and 5. However, each level was still detrended using a second−degree polynomial fit for the sake of consistency.

2.3.3 Virtual Potential Temperature and Specific Humidity Data

Figures 2.5 and 2.6 show the plots of the 20Hz raw virtual potential temperature and specific humidity data for the 5 vertically−stacked levels. The interfacial layer is now clearly evident at flight level 5 in both of these profiles.

For virtual potential temperature (figure 2.5) strong oscillations (> 3.0°K) are clearly evident in the transition from the inversion layer to the convective mixed layer. These oscillations are evidence of entrainment spikes from the warmer inversion layer above. The data for levels 3 and 4 show very little variability (less than 2°K) across the 45−75km flight path. Clearly evident from the overlayed detrend curves is the increase in virtual potential temperature as the distance from the Wisconsin shore increases. Overall, the CTBL is weakly stable as indicated by the slight increase in mean virtual potential temperature with height for all flight segments.

The plots of raw 20Hz specific humidity data (figure 2.6) also show the interfacial layer at level 5 with very strong oscillations (about 1g/kg) over the western

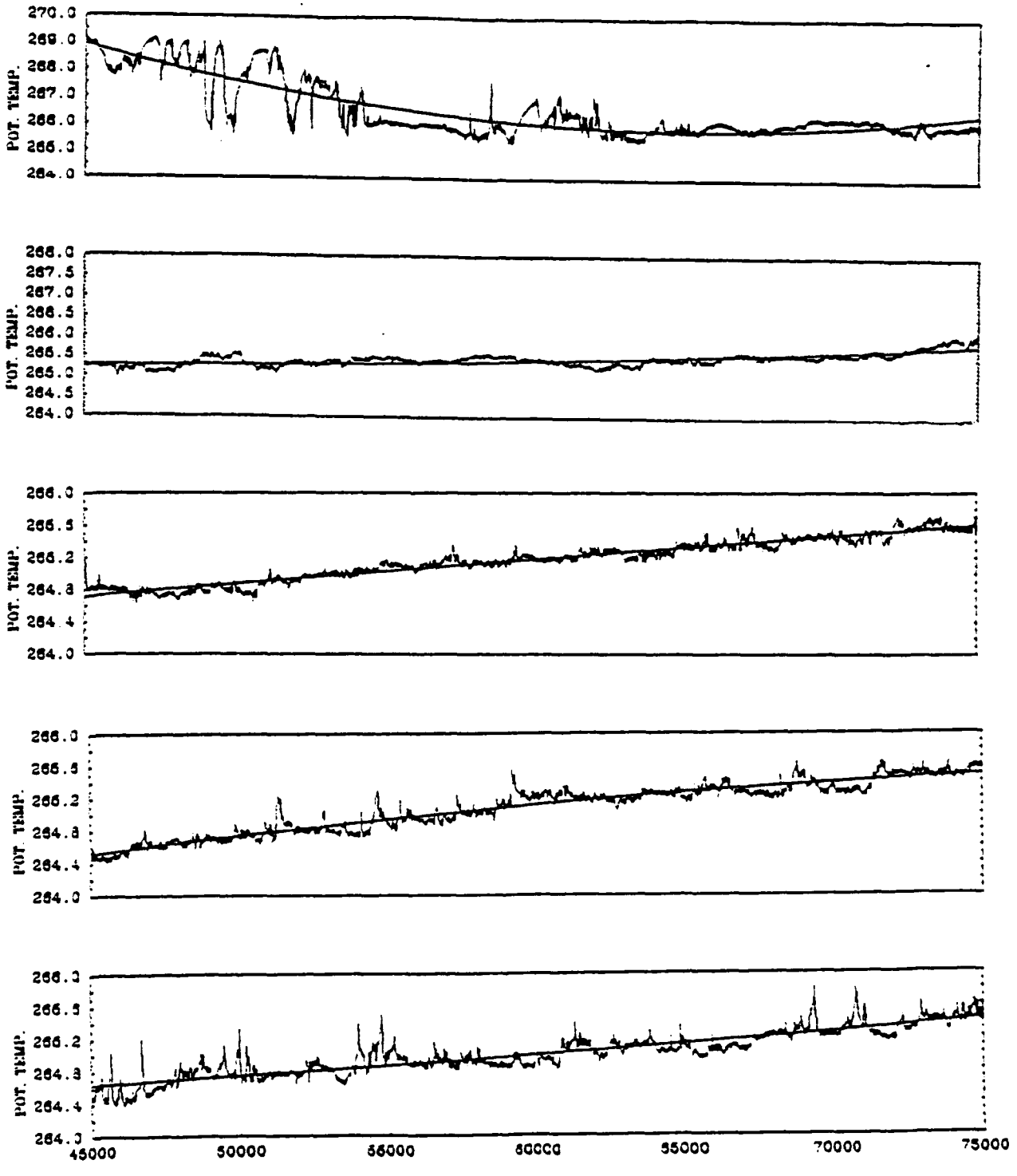

Figure 2.5 Plot of raw 20Hz Virtual Potential Temperature (°K) for flight levels 1 (bottom) through 5 (top) with detrend curve overlayed.

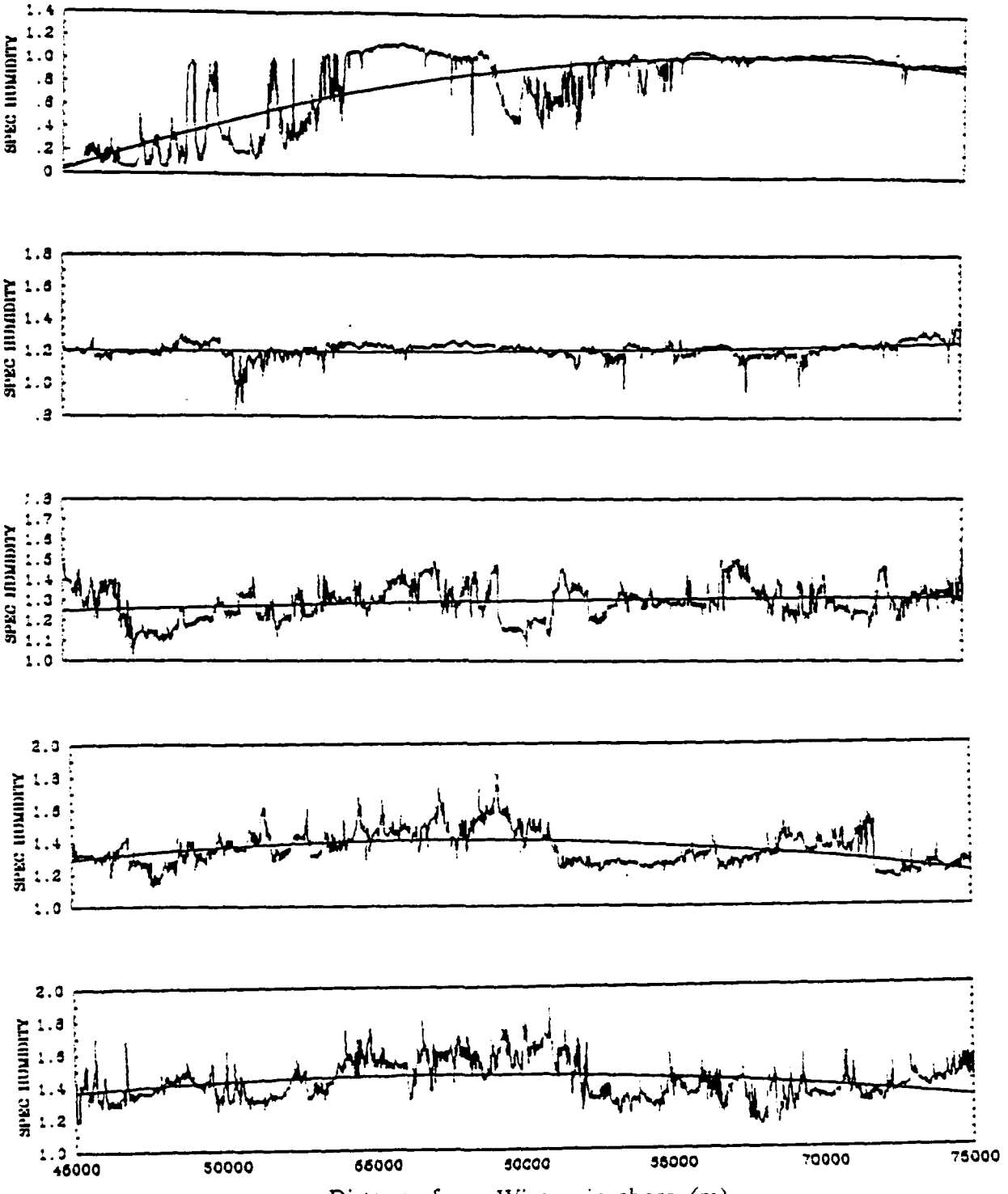

Figure 2.6 Plot of raw 20Hz specific humidity (g/kg), for flight levels 1 (bottom) through 5 (top) with detrend curve overlayed.

portion of the flight leg, indicative of entrainment of dry air from the overlying inversion layer. The average specific humidity decreases with increasing height (and distance from the moisture source) for all flight segments. The convective PBL appears to be quite moist with mean specific humidities as high as 1.46 g/kg at level 1. The specific humidity profile also supports the possibility of a convergence band in the vicinity of 61 km from the Wisconsin shore with relatively high (1.6 g/kg) specific humidity values in this region.

2.3.4 Detrended Data

Figures 2.7 through 2.11 show the plots of the 20Hz detrended data for u, v, w, Θ_v and q for all five flight levels for the 45–75km flight leg. A cursory comparison between the raw and detrended data plots shows that the detrending process has been successful in removing the large scale trends, especially at level 5, without removing the microscale fluctuations. A comparison of the maximum and minimum value for each variable both before and after detrending shows that the latter has very little effect on the range of the data.

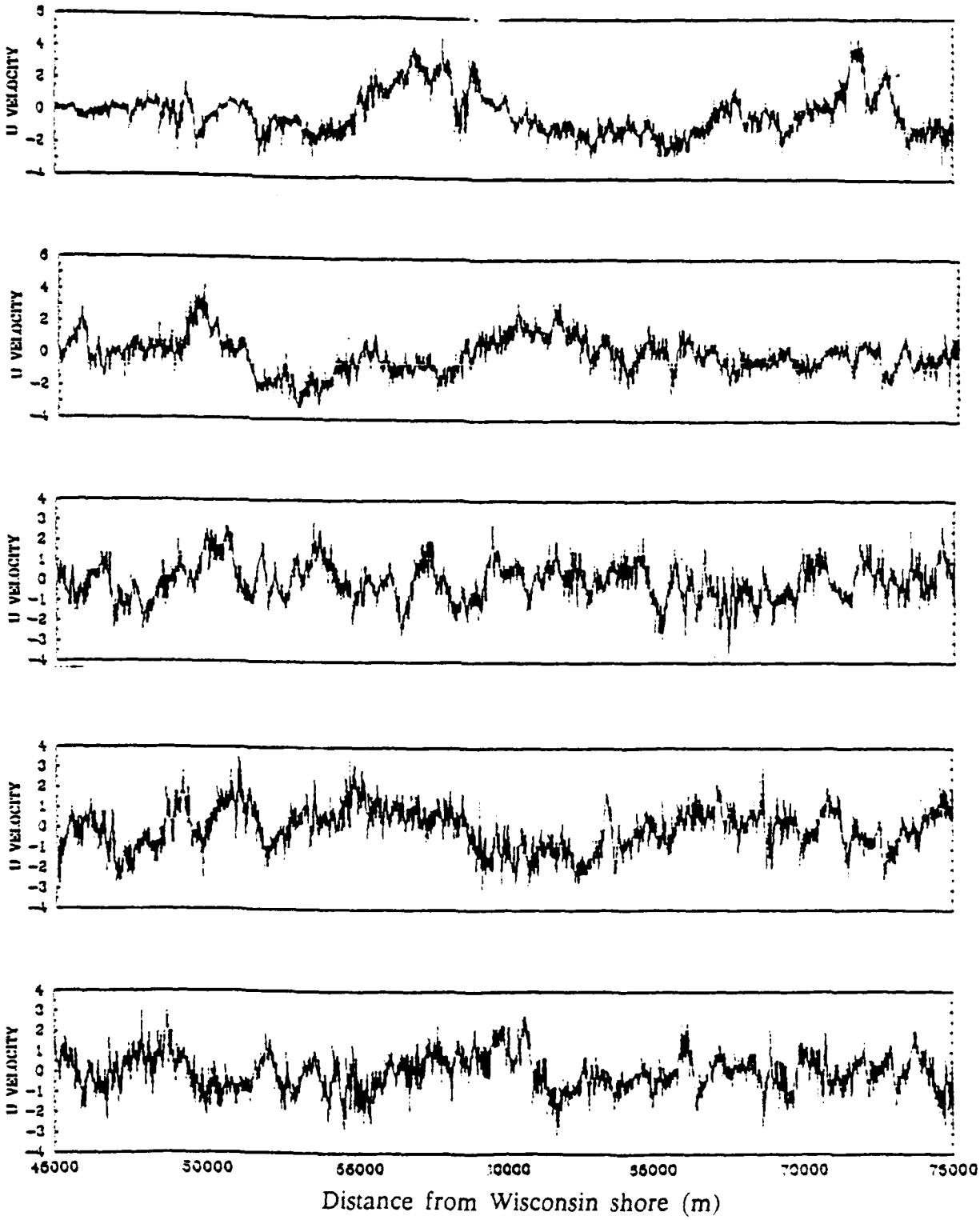

Figure 2.7 Plot of detrended 20Hz u wind component (m/s), for flight levels 1 (bottom) through 5 (top).

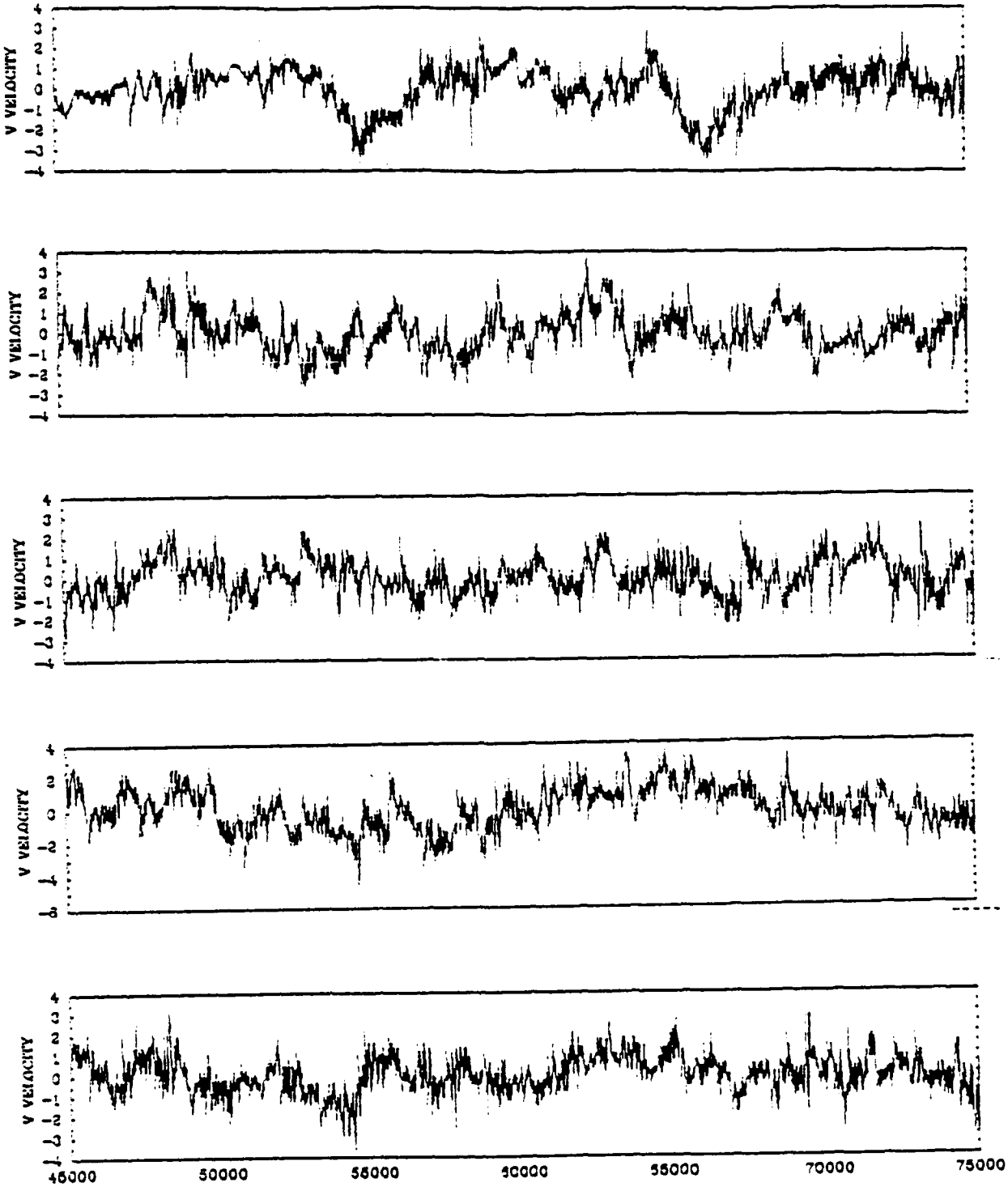

Figure 2.8 Plot of detrended 20Hz v wind component (m/s), for flight levels 1 (bottom) through 5 (top).

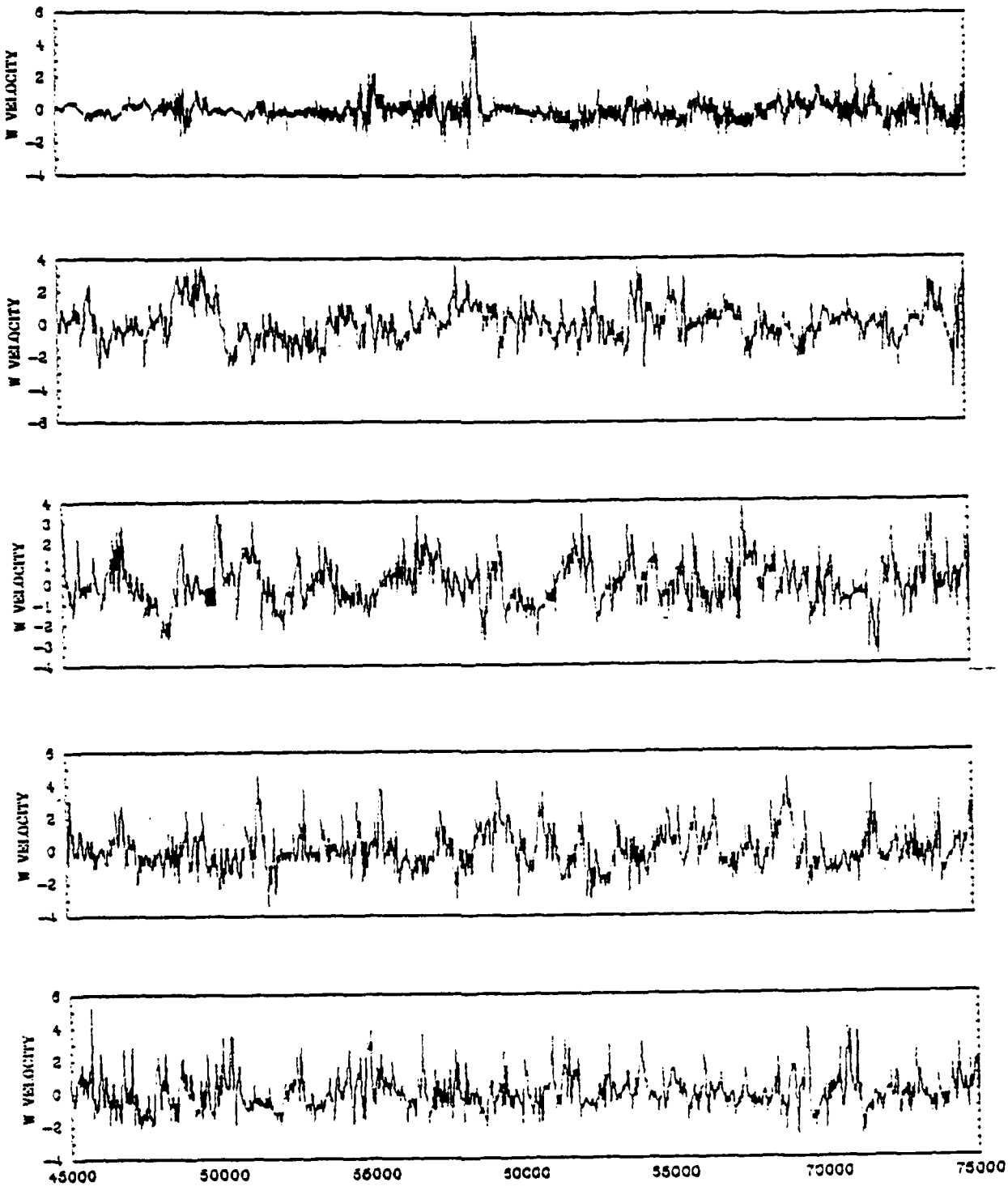

Figure 2.9 Plot of detrended 20Hz w wind component (m/s), for flight levels 1 (bottom) through 5 (top).

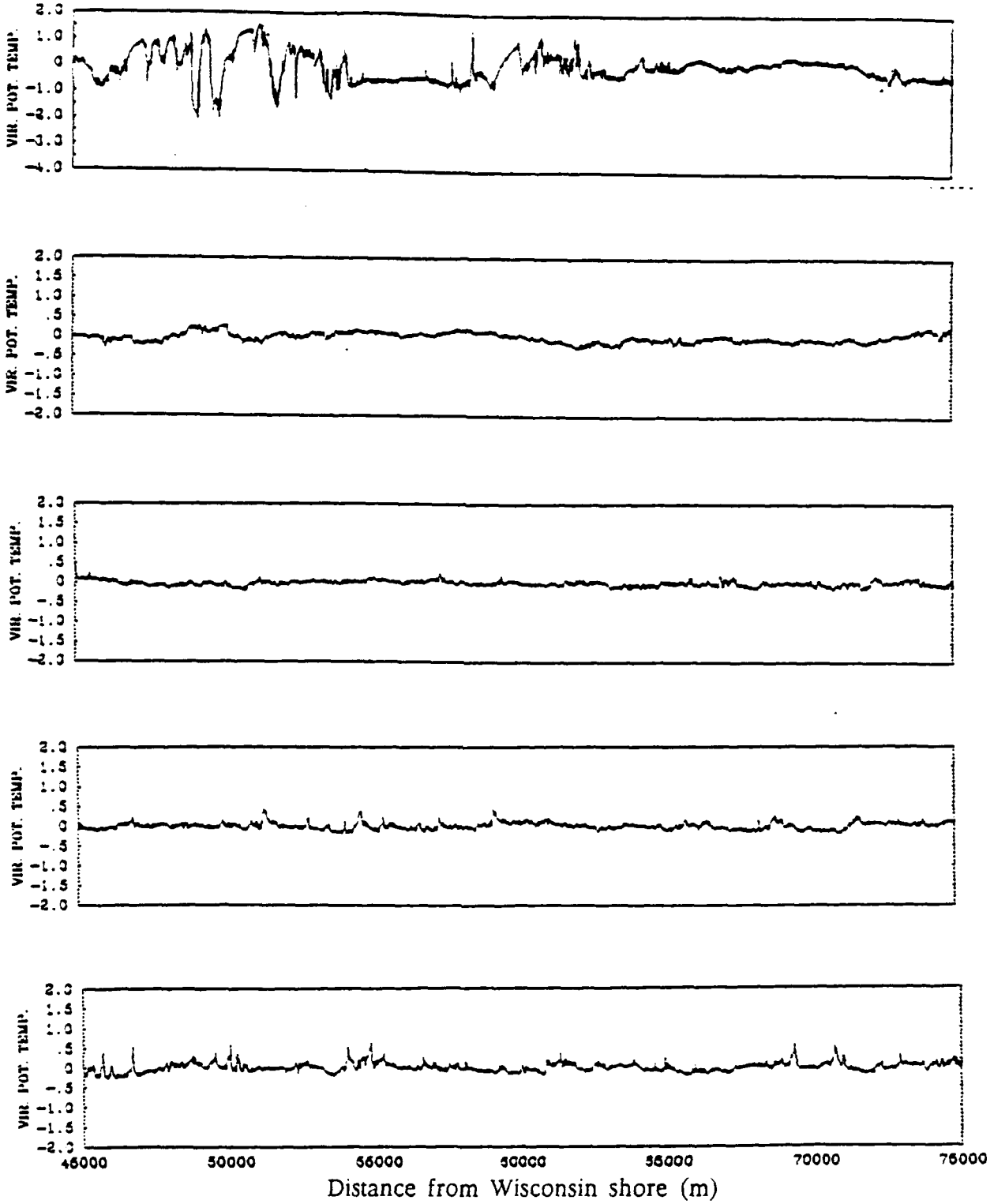

Figure 2.10 Plot of detrended 20Hz virtual potential temperature (°K), for flight levels 1 (bottom) through 5 (top).

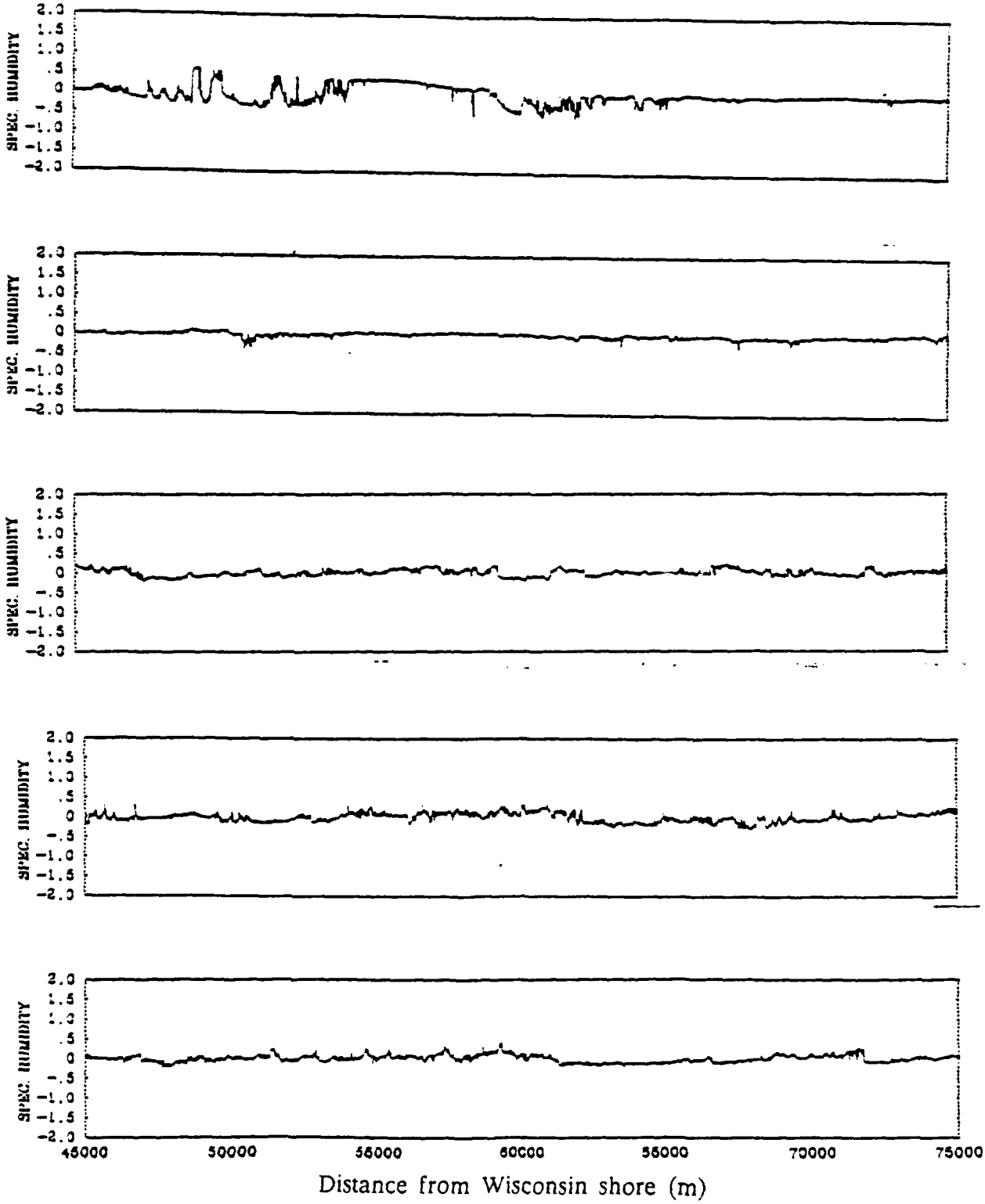

Figure 2.11 Plot of detrended 20Hz specific humidity (g/kg) for flight levels 1 (bottom) through 5 (top).

2.4 Aircraft and Instrument Specifications

The NCAR Beechcraft King Air (N312D) and Queen Air (N06D) are all metal, low-wing, pressurized monoplanes approved for flight in known icing conditions. Both aircraft have extensive research instrumentation on board, including sensors for measuring mean and fluctuating components of wind speed $\bar{u}$, $\bar{v}$, $\bar{w}$ and u', v', w', ambient temperature and pressure, dew point, water vapor fluctuations and geometric altitude, Aircraft position is available from the Inertial Navigation System (INS). Table 2.2 gives specifics about the instruments used to collect weather data used in this study.

Table 2.4 The Instrument specifications for the microphysical data collected by the NCAR King and Queen Air aircraft.

Variable	Symbol	Device	Range	Accuracy
Aircraft Altitude	ALAT	INS Litton LTN-51	+/-90°	< 1.0 nmi per flt. hr.
Aircraft Longitude	ALON	INS Litton LTN-51	+/-180°	< 1.0 nmi per flt. hr.
Aircraft Ground Speed	GSF	INS	0 - 400 m/s	< 1.0 knot per flt. hr.
Ambient Temperature	ATB	Rosemont 102E2AL	-60°-40°C	+/- .5°C
Vir.Pot.Temperature	VTHETA	Thermoelectric Hygrometer	-50° - 50°C	+/- 1.0°C <0°C
Absolute Humidity	VLA	Lyman-Alpha Hygrometer	0.1 - 25gm^{-3}	+/- 5% [1]
Specific Humidity	SPHUM	Johnson-Williams LWH	0 - 5gm^{-3}	-------
Wind Vector Horizontal component	UI, VI	Gust Probe and INS	0 - 100m/s (<10 min)	+/- 0.1m/s
Wind Vector Vertical component	WI	Gust Probe and INS	-15 - 15m/s (<10 min)	+/-0.1 m/s

[1] With periodic baselining

3. BOUNDARY LAYER STATISTICS

3.1 Other Observational Case Studies

As mentioned in Chapter 2, the selection of a "hand-picked" data set facilitates a comparison of the Project LESS results with those of other observational case studies and numerical models. Before the LESS results are presented, a brief description is given of these other observational case studies (AMTEX and MASEX) and the numerical models to which comparisons are also made.

3.1.1 Air Mass Transformation EXperiment (AMTEX)

AMTEX 74 and 75 were conducted as a subprogram of the Global Atmospheric Research Program (GARP) sponsored by the Japan National Committee for GARP. The goal of the field program was to increase the understanding of the processes by which heat, moisture, and momentum are transferred from the ocean surface through the boundary layer and to the free atmosphere under conditions of large temperature difference between the warm ocean and cold air above (Lenschow and Agee, 1976). The field program was conducted during 14–28 February 1974 and 14 February – 1 March 1975 over the East China Sea over the warm Kuroshio Current. Agee et al. (1973) have indicated that this is a climatologically favored region for the formation of MCC of the Type I variety.

Sources of data used during AMTEX 75 included 33 land stations in Japan that provided surface synoptic data on a regular basis during the period of the experiment. Three special ships, *Ryofu Maru*, *Keifu Maru* and *Nojima* and island stations were added to the network which formed a hexagon with Naha, Okinawa at the center

(see figure 2, Lenschow and Agee, 1976). The NCAR Electra aircraft flew nine research missions originating fr n Naha totaling 50 hours of flight time. The data collected by the aircraft were the focus of the analysis of Lenschow et al. (1980).

As was done by Chou et al. (1986), Comparisons in this study were restricted to those between the LESS and the AMTEX results for the four northerly wind events of the AMTEX that occurred on the 15th, 16th, 18th and 22nd of February 1975. The CAO events of the 24th and 26th were much weaker, with ΔT (difference between air and sea surface temperature) values $> -5°C$ (temperature difference less than 5°C). These ΔT values fall short of one of the necessary conditions for MCC formation proposed by Sheu and Agee (1977) of a temperature difference of at least 5°C between the overlying cold air and warmer water below. In addition the fetch for the 4 northerly wind events was approximately 1500 km, while the fetch for the northerly flow event of 10 Jan 84 during the LESS was approximately 250 km.

3.1.2 The Mesoscale Air–Sea EXchange (MASEX) Experiment

The MASEX field program was conducted in January 1983 with four daylong experimental flights conducted during CAO events on 16, 18, 19 and 20 January 1983. The primary goals of the MASEX experiment were to investigate the dynamics of the marine PBL and to assess remote sensing techniques for measuring the ocean waves and the surface sensible and latent heat fluxes (Chou et al., 1986). The area of operation for the experiment was bounded by 35°–41°N and 76°–69°W as shown in Figure 3.1 below. This area off the east coast of the United States is also identified by Agee et al. (1973) as a climatologically favored region for MCC formation as continental polar air moves off the land over the relatively warmer Gulf Current waters. The experiment was conducted from the Wallops Flight Facility with three aircraft, NOAA P–3, NASA P–3 and NASA Electra collecting data via various in situ and remote sensing instruments. Boundary layer parameters were measured

by the NOAA P–3 at various flight levels within the rectangle ABCD shown

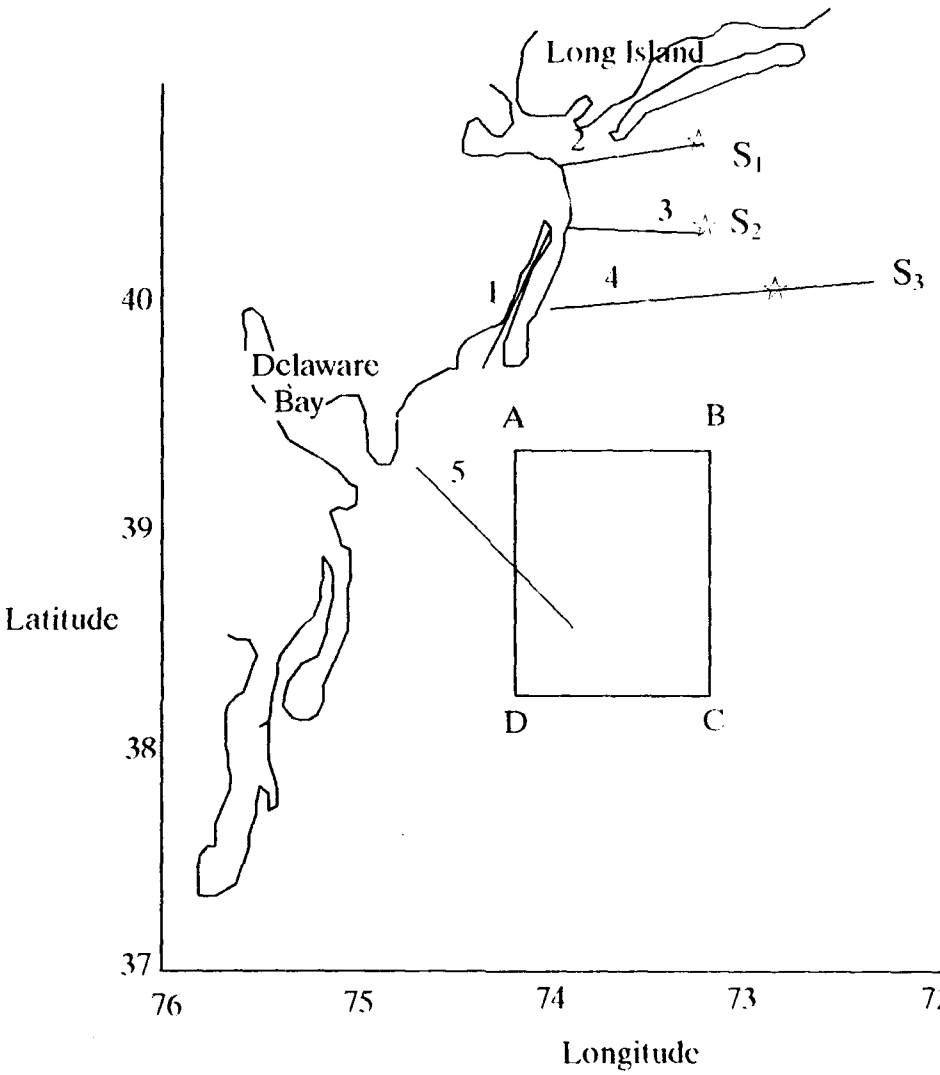

Figure 3.1. The NOAA P–3 and NASA Electra aircraft measurement locations. Temperature, humidity and wind are measured by dropsondes at locations S_1, S_2 and S_3. Downward looking lidar measurements from the NASA Electra aircraft are marked by the flight tracks 1 to 5. Boundary layer parameters are measured by the NOAA P–3 aircraft at the box ABCD. From Chou et al. (1986)

in Figure 3.1. Temperature, humidity and wind were measured by dropsondes at locations S_1, S_2 and S_3. Downward–looking lidar measurements from the NASA Electra aircraft are marked by the flight tracks 1 to 5. For the northerly flow case

of 20 January 1983, the fetch was about 200km. The ΔT value is not available but is probably larger than that for either the LESS or the AMTEX because of the smaller fetch and warm sea surface temperatures (12°C at the southeastern corner of the box ABCD). Table 3.1 gives a summary of the characteristics of the two observational case studies and the resulting data sets:

Table 3.1 Summary of observational case study characteristics

Study Name	Dates	Detrending	Flt. Path Length (km)	Elapsed Time (s)	Aircraft Orientation wrt mean wind
AMTEX	15,16,18 22 Feb 75	None	20 km	204.8	Varied
MASEX	20 Jan 83	Linear	40 km	360	Perpendicular
LESS	10 Jan 84	Quadratic	30 km	Varied 390–430	Perpendicular

The dates indicated for the AMTEX are not inclusive of all the dates of the study but indicates only those used for comparison in this paper (where air–sea temperature differences exceeded 5°C).

3.2 Numerical Models

Turbulent statistics calculated from the Project LESS data were also compared with those from two models; Deardorff's 3–D model (1980) and Moeng's Large–Eddy–Simulation model (1984). Each model is briefly discussed below.

3.2.1 Deardorff's 3–D Model

The Deardorff model was a three–dimensional numerical model containing 40^3 grid points inside a volume of horizontal area 5km x 5km and height 2km. The horizontal and vertical grid spacing were 125m and 50m respectively. The situation treated was day–33 of the Wangara data between 9a.m. and 5p.m. The surface was assumed to be horizontally homogeneous with respect to temperature and roughness. The scaling parameter z_i, the depth of the mixed layer, was defined

by Deardorff as the height at which the sensible heat flux is most negative. For purposes of comparison only case 6 from Deardorff's work will be used since it most closely replicates the conditions of the LESS. This case is for a stratocumulus deck occupying the upper half of the mixed layer with liquid–water effects included and cloud–top radiative flux divergence present at the uppermost grid volume in each vertical column for which $\bar{q}_l$, the Reynolds average of specific liquid–water content over the volume $\Delta x \bullet \Delta y \bullet \Delta z$, exceeded 0.01×10^{-3} (Deardorff, 1980). For this case the physical domain was reduced to a 2km cube and the horizontal grid spacing was set at 50m. The radiative flux divergence then occurred over only the uppermost 50m of cloud, while the cloud–top height varied somewhat in space and time.

3.2.2 Moeng's Large–Eddy–Simulation Model

As pointed out by Moeng (1984), a model which explicitly simulates the large eddies but parameterizes the small eddies is called a large–eddy simulation (LES) model. Moeng's LES model used a pseudospectral representation in the horizontal direction, in which the PBL turbulence is nearly homogeneous, and second–order finite–differencing in the vertical direction. The model output (to be discussed later) showed that the resolvable–scale eddies contain more turbulent energy and transfer more heat than do the subgrid–scale eddies,. The latter act mostly to dissipate the turbulent energy which cascades down from the resolvable–scale eddies. Except for within the surface layer, the subgrid–scale eddies do not contribute much to direct or indirect heat transfer (Moeng, 1984). The LES model was used to simulate day–33 of the Wangara data from hours 9 and 16. The grid used measured 32 x 32 x 40 resulting in a horizontal and vertical resolution of approximately 156m and 50m respectively with a 3s time step used. For simplicity, the moisture field and radiation effects were left out of the model.

3.3 Scaling

In this and the following sections, boundary layer statistics will be examined for the 10 Jan 84 CAO event of the Project LESS. Included in the statistics are means, variances, covariances, various TKE component values and skewness values. Results are presented for the 45–75km flight segment and the 2–15km (45–60km and 60–75km) segments which comprise it. In accordance with similarity principles, appropriate scaling has been done for the turbulent statistics based on Stull (1988) and Lenschow et al. (1980) as follows:

Z_i: depth of the mixed layer above the ocean surface, taken to be the inversion base height;

w^*: free convective scaling velocity, based on the buoyancy flux at flight level 1 (50m above the lake surface);

$$w^* = \left[\frac{g\, z_i}{\overline{\Theta_v}} \overline{(w'\Theta'_v)_1} \right]^{1/3} ; \qquad (3.1)$$

u^*: friction velocity, $u^* = \left[\left(\overline{u'w'} \right)_1^2 + \left(\overline{v'w'} \right)_1^2 \right]^{1/4}$; (3.2)

q^*: moisture scale, $q^* = \dfrac{\overline{(w'q')_1}}{w^*}$; (3.3)

Θ_v^*: virtual potential temperature scale, $\Theta_v^* = \dfrac{\overline{(w'\Theta_v')_1}}{w^*}$. (3.4)

The free convective scaling velocity has been used for scaling in most instances because the boundary layer was well mixed and filled with thermals due to strong heating from below. The friction velocity has been used for scaling the stress profiles so as to facilitate comparison with the MASEX and AMTEX results.

3.4 Boundary Layer Means

Figure 3.2 gives the vertical profile of means for the raw 20Hz u and v wind components for the 45–75km, 45–60km and 60–75 km flight segments. Note that mean wind speeds are not indicated for flight level 5 for the 45–75km leg since this level represents a mixture of both convective and non–convective data. Level 5 for the 45–60 km leg is within the interfacial layer. This is particularly evident in the u–component which has its highest mean value at this level. The overall mean wind is almost due north throughout the mixed layer with speeds of between 12 and 15 knots. For the 45–60 km segment at level 5 the mean wind is at 20° (i.e. from the northeast) at about 55 ms^{-1} (approximately 15 knots). The strongest average winds are in the subcloud layer at levels 1 and 2; the weakest are in the cloud layer at levels 3 and 4.

Figure 3.3 (see below) shows the vertical profile of the means for the raw 20Hz vertical velocity, w, for the different flight segments. Clearly the mean vertical velocity, $\overline{w}$, is not zero at any of the flight levels as is required in many numerical models. The strongest (positive) mean vertical velocities are at level 3, within the cloud layer, for all three segments; the weakest are at level 1 where the mean vertical velocities are weakly negative. The mean vertical velocity at level 5 for both 15km segments is weakly negative, indicative of overall weak subsidence at this level.

Figure 3.4 (see below) is the vertical profile of the means for both the raw 20Hz virtual potential temperature, Θ_v, and the raw 20Hz calibrated specific humidity, q. As one would expect in a Type I convective boundary layer, the Θ_v profile

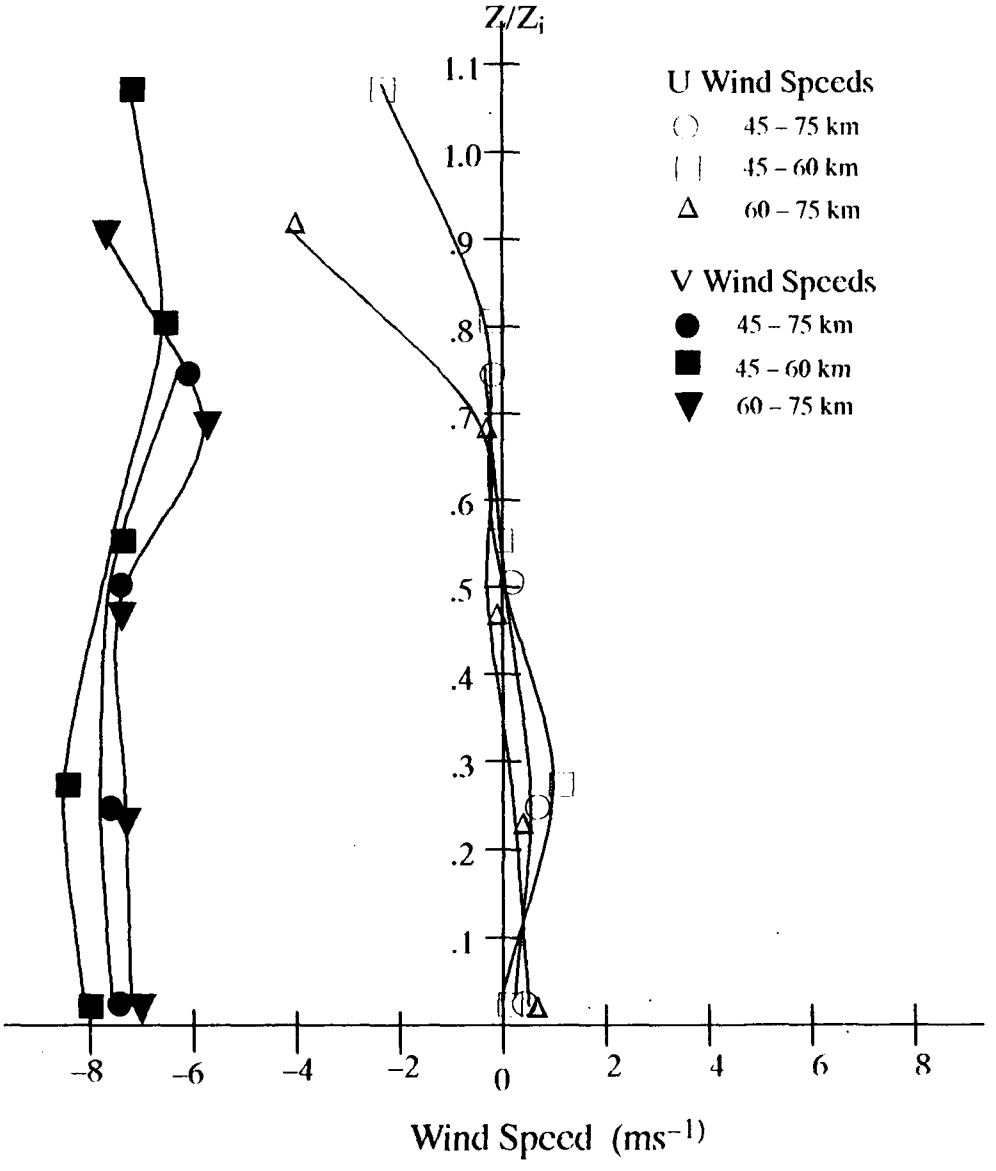

Figure 3.2 Vertical profile of mean raw 20Hz u and v–wind speeds (m/s) for the 5 Project LESS flight levels for the 45–75km, 45–60km and 60–75km segments

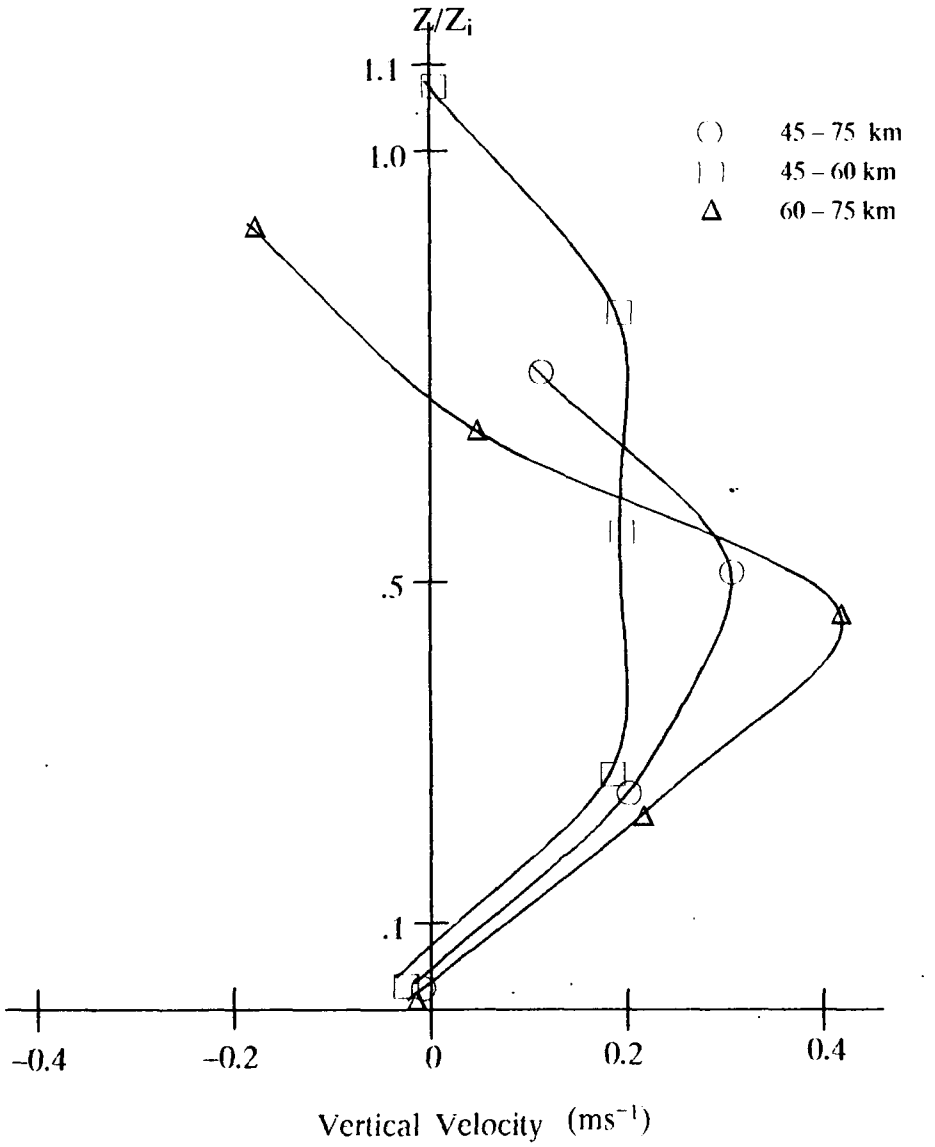

Figure 3.3 Vertical profile of average raw 20Hz w–wind speeds for the 5 Project LESS flight levels for the 45–75km, 45–60km and 60–75km segments

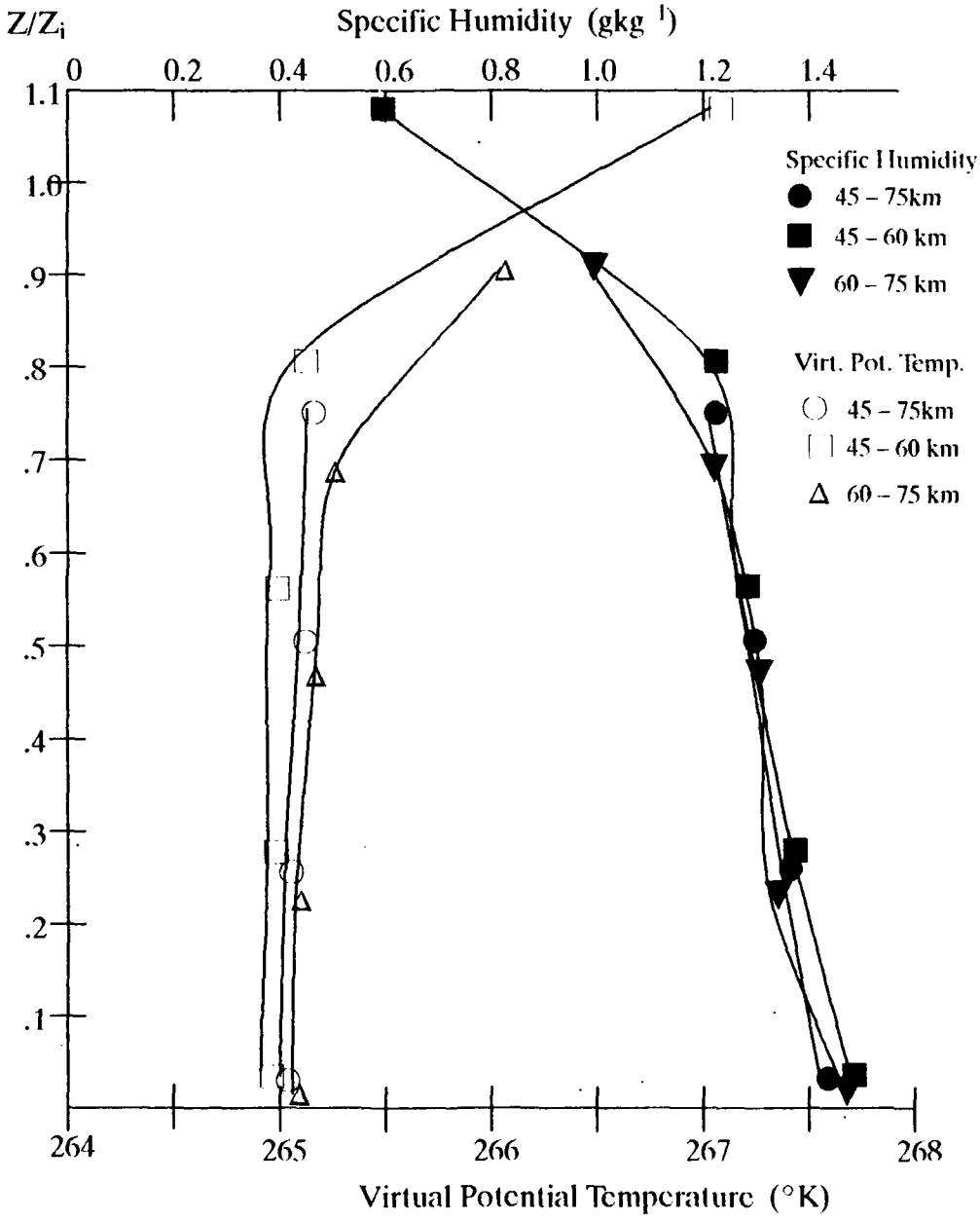

Figure 3.4 Vertical profile of average raw 20Hz virtual potential temperature and specific humidity for the 5 Project LESS flight levels for the 45–75km, 45–60km and 60–75km segments

is neutral dry within the subcloud layer (level 2) and neutral moist within the cloud layer (levels 3 and 4). The vertical profile of Θ_v shows very clearly the warm air intrusion due to entrainment occurring at the top of the PBL for both the 45–60km and 60–75km segments with an increase in Θ_v of nearly 2°K from level 4 to level 5 for the 45–60km flight segment. The vertical profile of $\bar{q}$ shows a decrease in specific humidity with height as the distance from the moisture source (i.e. Lake Michigan) increases. The drop in $\bar{q}$ is especially dramatic for the 45–60km segment at level 5 where a 50% decrease is observed from level 4 indicating entrainment of dry inversion air.

3.5 Boundary Layer Variances

As pointed out by Stull (1988) variances of variables such as u, v, w, Θ_v, and q give information about the turbulent energies and intensities. Lenschow and Wyngaard (1980) point out that turbulence second–moment budgets are of considerable importance in atmospheric boundary layer (ABL) modeling. In this section the average variances of u, v, w, Θ_v, and q are presented as computed from the detrended data sets obtained from the raw 20Hz data as described in section 2.3. To calculate the turbulent variation for a variable, u, one would normally subtract the mean $\bar{u}$ from each instantaneous value of u as shown in the equation below:

$$u' = u_i - \bar{u} , \qquad (3.5)$$

where u′ represents the turbulent fluctuation in u. This process is known as Reynold's decomposition. For the detrending process, $\bar{u}$ can be thought of as a running average (actually its the predicted value for each u_i resulting from the second degree polynomial detrending) which is subtracted from each instantaneous value of u. The resulting u′ values are squared and then averaged over the given flight segment. Finally, the averages are normalized by the square of the appropriate scaling factor (w^*, Θ_v^* or q^*) which provides dimensionless results for comparison with other studies.

Table 3.1 gives a summary of the variances for the 3 flight segments for the 10 Jan 84 CAO event. The values for w^*, Θ_v^*, and q^* are also shown for each flight segment. Since each segment was detrended separately, the scaling factors were also calculated separately for each leg.

Table 3.2 Project LESS boundary layer normalized average variances.

Variances (45 – 75 km)

Z_i = 1240m, w^* = 1.4684 ms^{-1}, Θ_v^* = 0.0470 °K, q^* = 0.0281 g kg^{-1}

Flight Level	$\frac{Z}{Zi}$	$\frac{\overline{u'^2}}{w^{*2}}$	$\frac{\overline{v'^2}}{w^{*2}}$	$\frac{\overline{w'^2}}{w^{*2}}$	$\frac{\overline{\Theta_v'^2}}{\Theta_v^{*2}}$	$\frac{\overline{q'^2}}{q^{*2}}$
5		(Convective and non-convective data not averaged)				
4	.7500	0.5697	0.4377	0.5700	5.7031	1.8536
3	.5161	0.4267	0.3666	0.5669	2.0492	7.0896
2	.2581	0.5047	0.7132	0.6588	3.5537	10.7675
1	.0403	0.3714	0.3587	0.5452	6.4843	15.2117

Variances (45 – 60 km)

Z_i = 1140m, w^* = 1.4445 ms^{-1}, Θ_v^* = 0.0495 °K, q^* = 0.0347 g kg^{-1}

Flight Level	$\frac{Z}{Zi}$	$\frac{\overline{u'^2}}{w^{*2}}$	$\frac{\overline{v'^2}}{w^{*2}}$	$\frac{\overline{w'^2}}{w^{*2}}$	$\frac{\overline{\Theta_v'^2}}{\Theta_v^{*2}}$	$\frac{\overline{q'^2}}{q^{*2}}$
5*	1.0807	0.5294	0.4644	0.2090	185.8579	37.2395
4	.8158	0.5802	0.4676	0.6392	3.4100	2.2073
3	.5614	0.4753	0.3125	0.5701	1.8690	4.3771
2	.2807	0.4269	0.5486	0.6192	3.4206	3.7420
1	.0439	0.3252	0.3394	0.5907	5.7819	5.8629

Variances (60 – 75 km)

Z_i = 1340m, w^* = 1.4754 ms^{-1}, Θ_v^* = 0.0440 °K, q^* = 0.0194 g kg^{-1}

Flight Level	$\frac{Z}{Zi}$	$\frac{\overline{u'^2}}{w^{*2}}$	$\frac{\overline{v'^2}}{w^{*2}}$	$\frac{\overline{w'^2}}{w^{*2}}$	$\frac{\overline{\Theta_v'^2}}{\Theta_v^{*2}}$	$\frac{\overline{q'^2}}{q^{*2}}$
5	.9194	0.6318	0.4262	0.1390	37.0043	17.6242
4	.6940	0.2210	0.3606	0.4828	2.9577	1.8473
3	.4776	0.3227	0.3840	0.5723	1.8727	7.4173
2	.2388	0.3299	0.3478	0.6831	2.7842	29.3327
1	.0373	0.3362	0.2983	0.5085	5.5732	15.7693

* Level 5 is above the convective PBL.

Note that the free convective scaling velocity is generally 4 to 5 times as large as the friction velocity (see Table 3.3 for u^*), indicating that buoyancy is dominating over shearing forces at level 1.

3.5.1 Comparisons with Observational Case Studies

Figure 3.5 shows the vertical profile of the average u variance for both the Project LESS and AMTEX studies. Generally the shapes of the profiles are in very good agreement with values for the LESS approximately 50% to 100% larger than the AMTEX values with the exception of the very lowest data levels where the AMTEX values are slightly larger. The AMTEX results may be higher than for the LESS at the lowest levels because data were collected closer to the ocean surface where shear would be strongest. Since the mean variances have been scaled using w^*, which takes into account the surface buoyancy flux and, hence, the different strengths of the heat source (i.e. different ΔT values), the larger values of u variance for the LESS is probably due to stronger shear resulting from a shorter fetch than that of the AMTEX (250km vs 1500km)

The vertical profile for the average v-component variance (figure 3.6) is very similar to that of the u-component. The values for the LESS are consistently larger than those of the AMTEX; as much as 300% larger for level 2 of the LESS data. Very little variation is noticeable in the AMTEX results; but a significant peak is clearly shown at level 2 in the LESS profile, with a value of 0.7132 for the 45–75km leg. The vertical profile for the average w-component variance (figure 3.7) shows more clearly than either of the first two profiles how much more dynamically active the CTBL for the LESS was than that of the AMTEX. Values are consistently 200% to 300% larger in the LESS case with maxima found in the subcloud layer at level

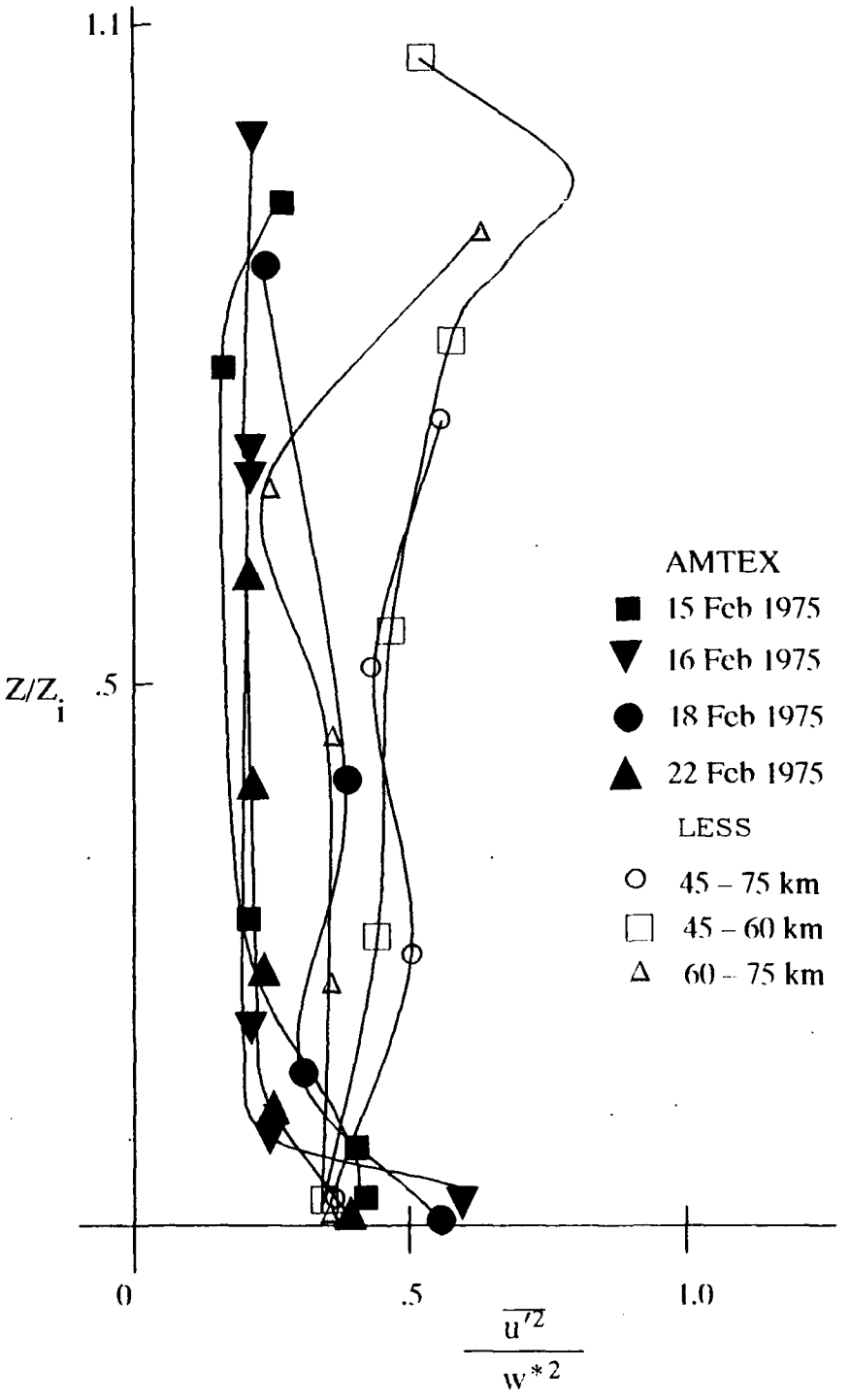

Figure 3.5 Vertical profile of average u–wind component variance for the LESS and AMTEX normalized by w^{*2}.

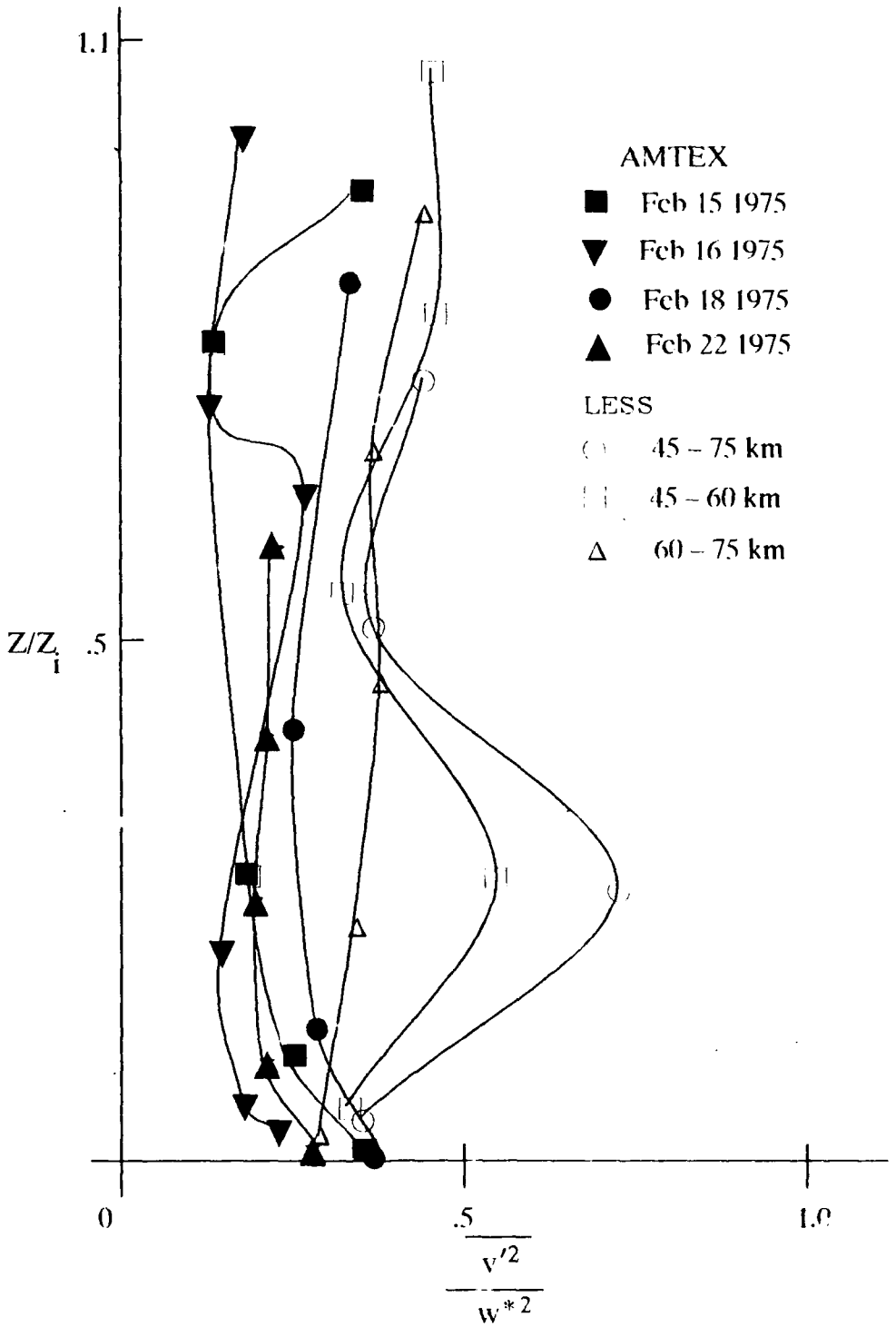

Figure 3.6 Vertical profile of average v–wind component variance for the LESS and the AMTEX normalized by w^{*2}

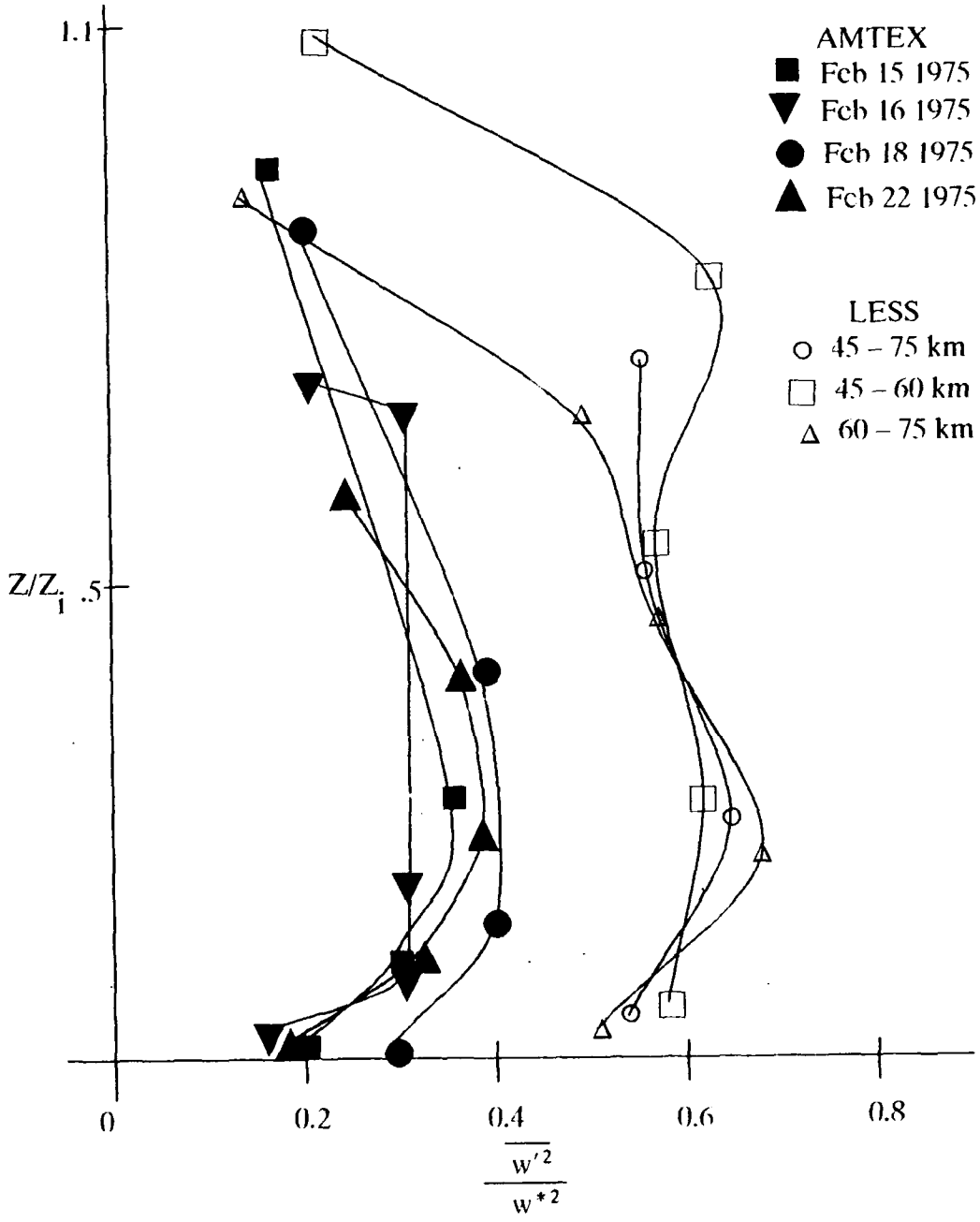

Figure 3.7 Vertical profile of average w–wind component variance for the LESS and the AMTEX normalized by w^{*2}

2 and in the cloud layer at level 4. Both the LESS and AMTEX results show the effect of the capping inversion with a significant drop–off, especially in the LESS results, in the average variance at levels near the inversion base. Clearly the capping inversion acts to dampen the vertical velocity variances (i.e. turbulence) at this level.

The vertical profiles for the average Θ_v and q variances (see Figures 3.8 through 3.11) show the effects of entrainment very clearly near the top of the mixed layer, where the variances are as much as 50 times larger than over the bulk of the mixed layer. The increase in the Θ_v variance near the top of the mixed layer is larger than that for q variance because the normalized potential temperature jump ($\Delta\Theta_v/\Theta_v^*$) is larger than that of the humidity jump ($\Delta q/q^*$) at the top of the PBL (Chou et al., 1986). Results for the MASEX are from segments of the box ABCD shown in Figure 3.1 earlier. Both the AB and CD flight segments, both of which were perpendicular to the mean wind direction, are divided into an east (E) and west (W) segment. This division was done by Chou et al. because the PBL height increases eastward and, hence, the normalized height Z/Z_i decreases eastward for a leg flown at a constant height.

3.5.2 Comparisons with Model results

A comparison of the average u variance for the LESS with results from Moeng's LES model for hour 16 of day 33 of the Wangara experiment (Figure 3.12) reveals a very similar profile in the lower half of the convective PBL. In the upper half of the PBL the u variance for the LESS continues to increase, reaching a maximum at level 5. In the LES, the average u variance decreases above 0.5 Z/Z_i. The increase in average u variance for the LESS may be due to the release of the latent heat of condensation at level 4, thus increasing the horizontal component of TKE.

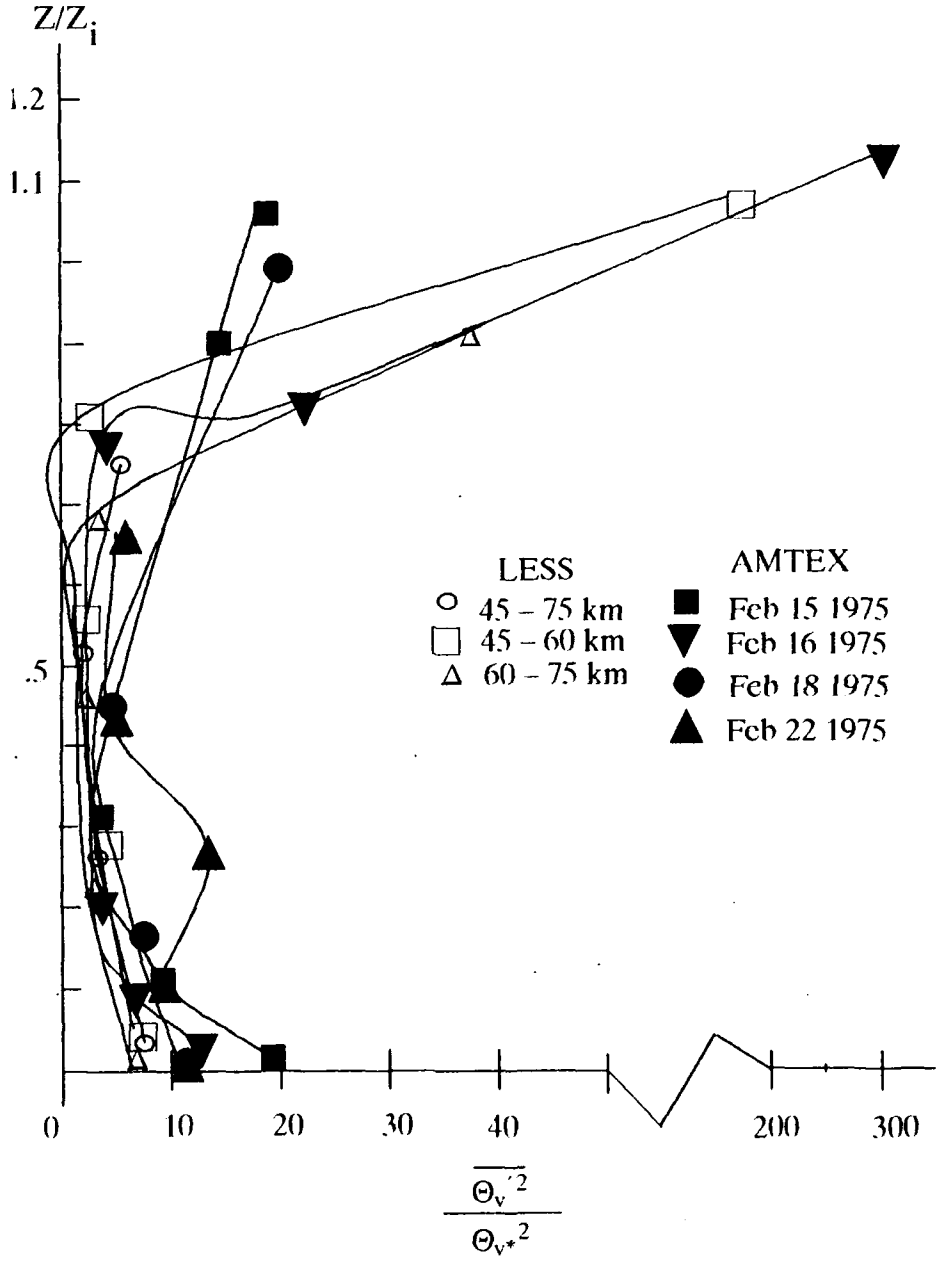

Figure 3.8 Vertical profile of average virtual potential temperature for the LESS and the AMTEX normalized by Θ_v^{*2}

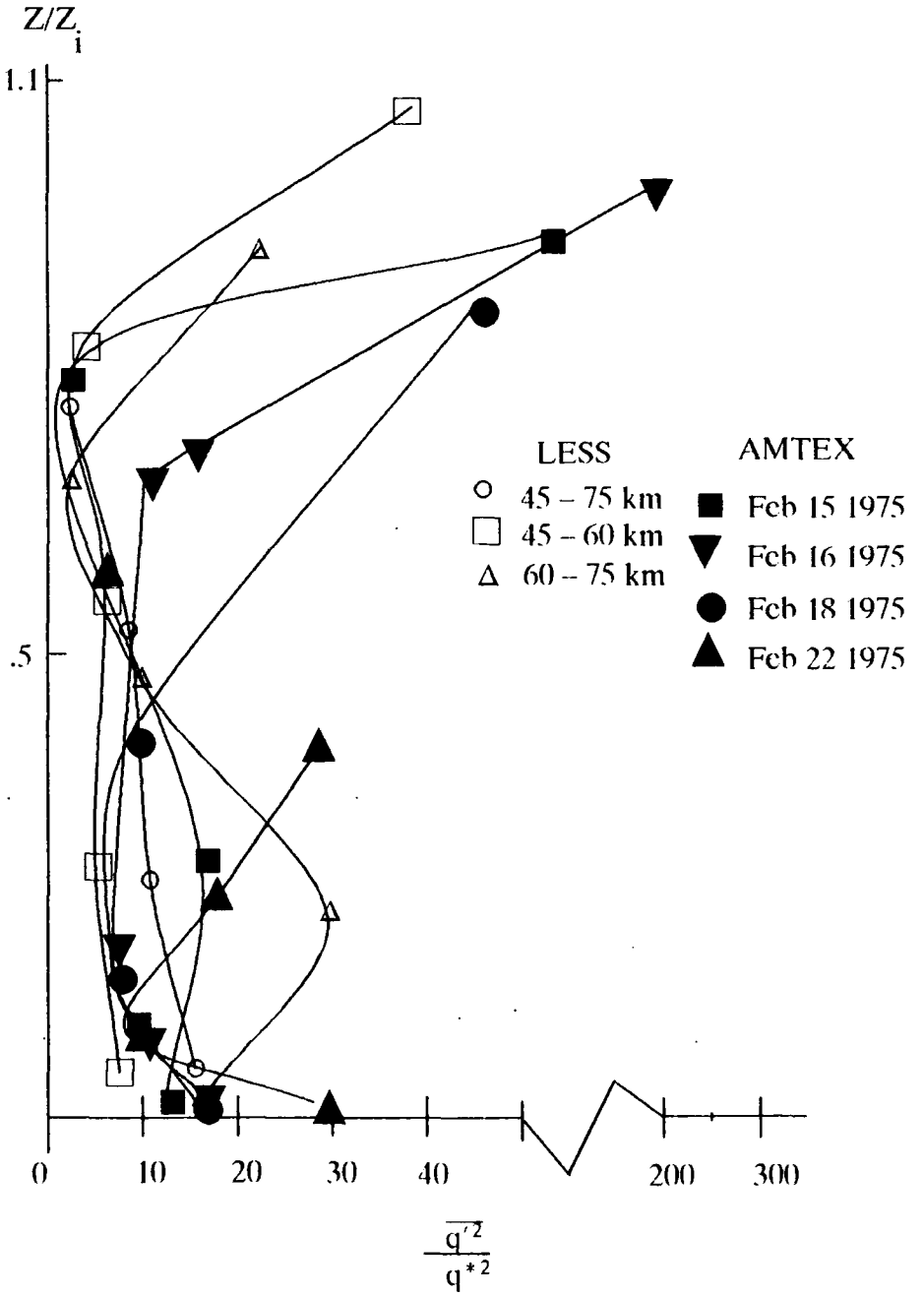

Figure 3.9 Vertical profile of average specific humidity variance for the LESS and AMTEX normalized by q^{*2}

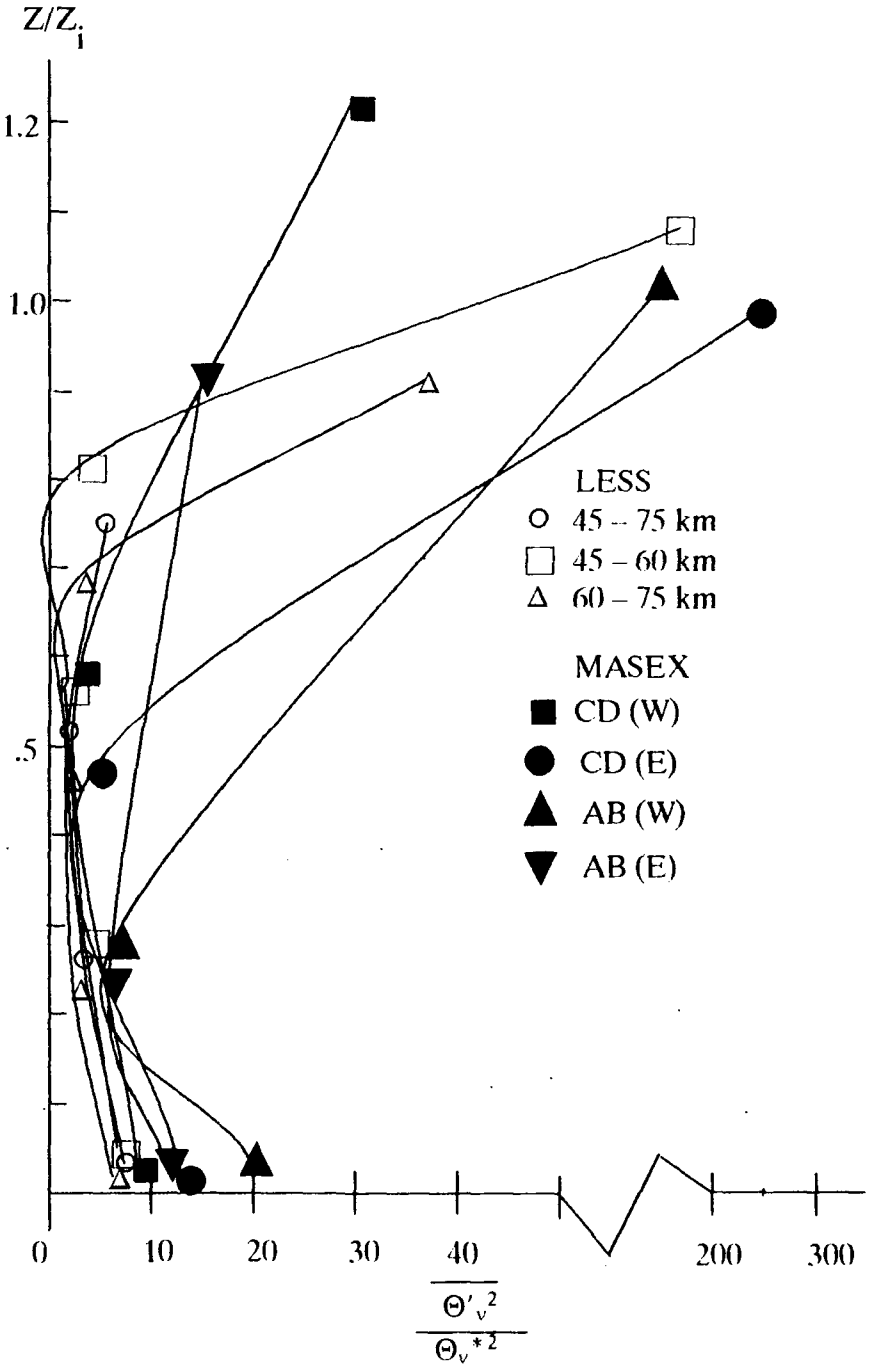

Figure 3.10 Vertical profile of average virtual potential temperature variance for the LESS and the MASEX normalized by Θ_v^{*2}

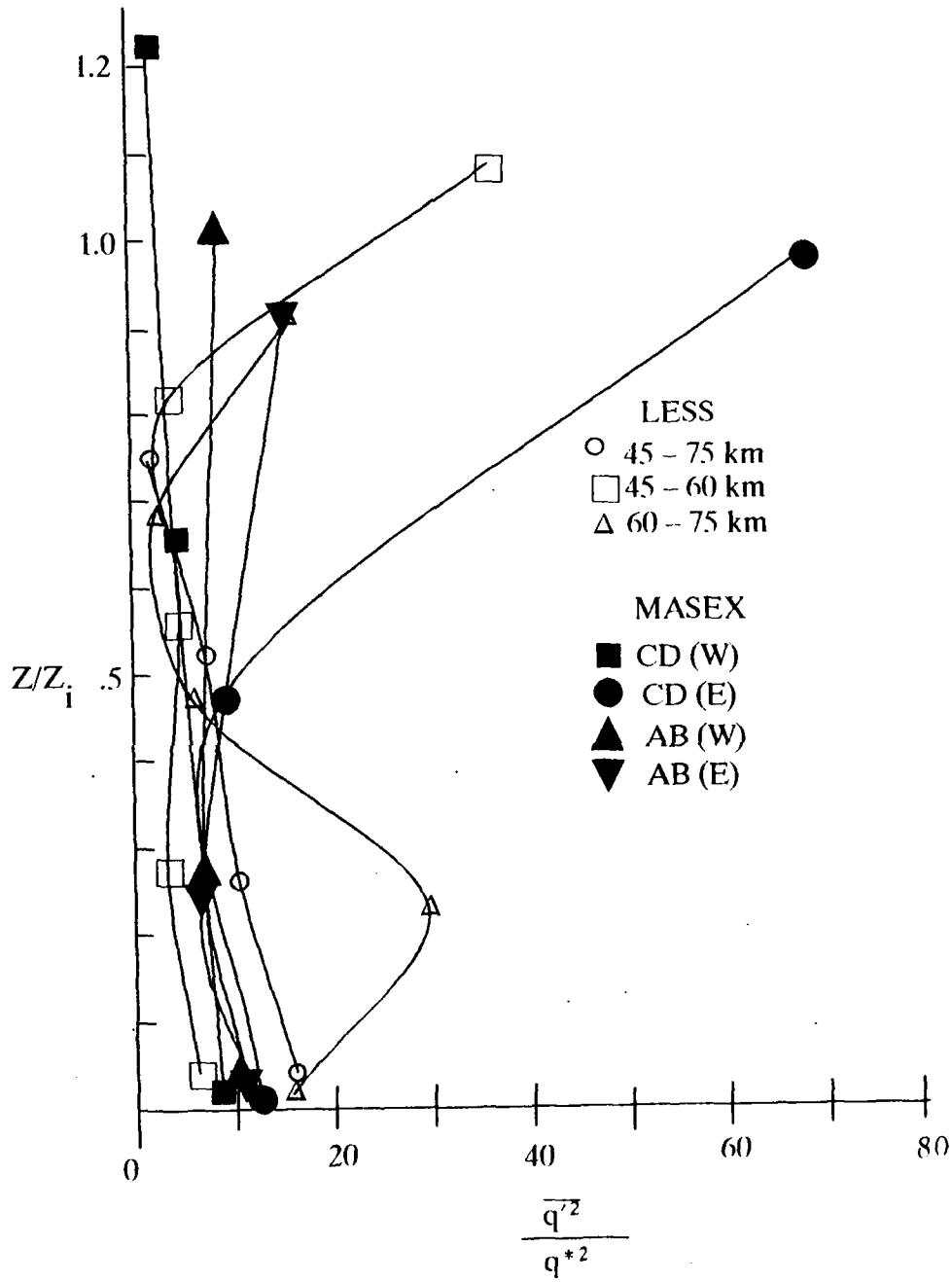

Figure 3.11 Vertical profile of average specific humidity variance for the LESS and the MASEX normalized by q^{*2}

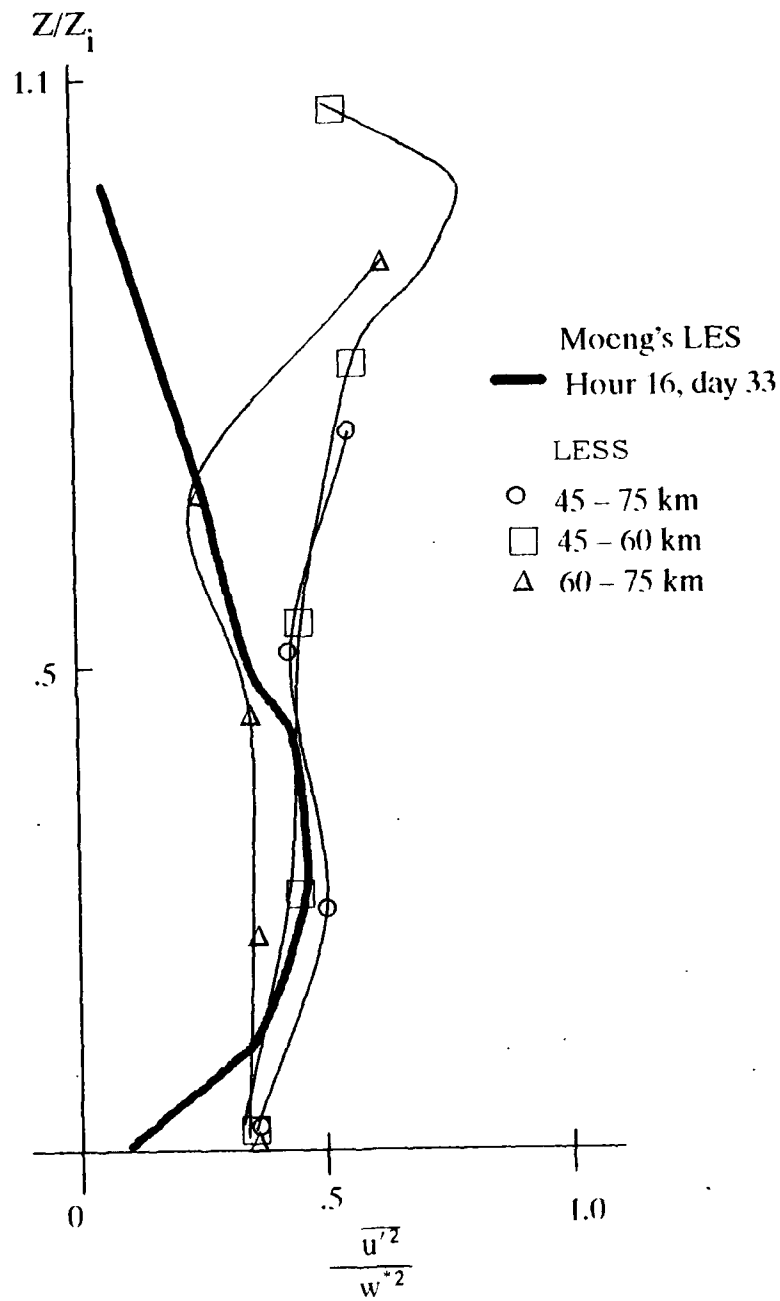

Figure 3.12 Vertical profile of average u–wind component variance for the LESS and Moeng's LES model normalized by w^{*2}

3.6 Boundary Layer Covariances

As pointed out by Stull (1988), covariances provide a measure of flux or stress, where a flux is defined as the transfer of a quantity such as mass, heat, moisture or momentum per unit area per unit time. Statistically, the covariance of two variables A and B is defined as:

$$covar(A,B) = \frac{1}{N} \sum_{i=0}^{N-1} (A_i - \overline{A}) \cdot (B_i - \overline{B}) \qquad (3.6)$$

Using Reynolds averaging, this can be reduced to:

$$covar(A,B) = \frac{1}{N} \sum_{i=0}^{N-1} a'_i \, b'_i = \overline{a' \, b'} \qquad (3.7)$$

The covariance then indicates the degree of common relationship between the two variables A and B. The covariances that have been calculated and will be presented in this paper are those listed below:

Average vertical kinematic eddy flux of u–momentum = $\overline{u'w'}$

Average vertical kinematic eddy flux of v–momentum = $\overline{v'w'}$

Average vertical kinematic eddy flux of virtual potential temperature = $\overline{w'\Theta'_v}$

Average vertical kinematic eddy moisture flux = $\overline{w'q'}$

Future references to these quantities will omit the word kinematic.

3.6.1 Comparisons among Observational Case Studies

Table 3.3 shown below gives fluxes/stresses for the buoyancy, moisture and momentum for the Project LESS data set. As was done previously for the momen-

tum,heat and moisture variances, the covariances have been normalized by the quantities indicated.

Table 3.3 Project LESS boundary layer normalized average covariances

Covariances (45 – 75 km)

Z_i = 1240m, w^* = 1.4684 ms $^{-1}$, u^* = 0.3159 ms $^{-1}$, Θ_v^* = 0.0470 °K, q^* = 0.0281 g kg $^{-1}$

Flight Level	$\frac{Z}{Zi}$	$\frac{\overline{w'q'}}{w^*q^*}$	$\frac{\overline{w'\Theta_v'}}{w^*\Theta_v^*}$	$\frac{\overline{u'w'}}{u^{*2}}$	$\frac{\overline{v'w'}}{u^{*2}}$
5		(Convective and non-convective data not averaged)			
4	.7500	0.5595	0.7594	3.2271	–1.7356
3	.5161	1.1011	0.2825	1.3275	–2.4996
2	.2581	1.0790	0.7118	0.3018	0.4067
1	.0403	1.0000	1.0000	–0.9137	0.4064

Covariances (45 – 60 km)

Z_i = 1140m, w^* = 1.4445 ms $^{-1}$, u^* = 0.3814 ms $^{-1}$, Θ_v^* = 0.0495 °K, q^* = 0.0347 g kg $^{-1}$

Flight Level	$\frac{Z}{Zi}$	$\frac{\overline{w'q'}}{w^*q^*}$	$\frac{\overline{w'\Theta_v'}}{w^*\Theta_v^*}$	$\frac{\overline{u'w'}}{u^{*2}}$	$\frac{\overline{v'w'}}{u^{*2}}$
5*	1.0807	0.2786	0.1635	0.5560	–0.5404
4	.8158	0.6190	0.8869	3.8621	–0.7328
3	.5614	0.8494	0.2710	1.6478	–1.7392
2	.2807	0.8469	0.6815	–0.0680	0.1816
1	.0439	1.0000	1.0000	–0.9847	0.1744

Covariances (60 – 75 km)

Z_i = 1340m, w^* = 1.4754 ms^{-1}, u^* = 0.2493 ms $^{-1}$, Θ_v^* = 0.0440 °K, q^* = 0.0194 g kg $^{-1}$

Flight Level	$\frac{Z}{Zi}$	$\frac{\overline{w'q'}}{w^*q^*}$	$\frac{\overline{w'\Theta_v'}}{w^*\Theta_v^*}$	$\frac{\overline{u'w'}}{u^{*2}}$	$\frac{\overline{v'w'}}{u^{*2}}$
5	.9194	0.1706	0.4411	0.3696	1.2031
4	.6940	0.5878	0.5616	–0.5012	–3.6597
3	.4776	1.2249	0.2863	0.7666	–3.7191
2	.2388	1.4032	0.7234	1.3672	1.9726
1	.0373	1.0000	1.0000	–0.4344	0.9007

* Level 5 is above the convective PBL.

Figures 3.13 and 3.14 show the vertical profiles of the average normalized crosswind and alongwind stresses respectively for the LESS and AMTEX data. The

crosswind component generally increases with height in the LESS with the exception of the 60–75 km segment and level 5 for the 45–60km segment. Results for the two studies are in good agreement below about 0.4 Z/Z_i, indicating that crosswind shear is comparable at low levels for the two studies. However, the LESS crosswind stress is significantly stronger from 0.5 Z/Z_i to approximately 0.9 Z/Z_i. In order to physically interpret the meaning of the average covariances, each covariance sum was partitioned into its positive and negative part. Naturally, the one with the larger absolute value determined the sign of the covariance. Then the percentage of each partition that had positive w′ and negative w′ values was calculated. In this way, the overall sign of the other variable (u′ or v′) could also be determined. From this analysis it was then possible to physically interpret the meaning of the average covariances in terms of upward or downward transport of easterly/westerly ($u'<0$, $u'>0$) or northerly/southerly ($v'<0$, $v'>0$) momentum. Some of the results of this analysis and corresponding physical interpretation are shown in Table 3.3 following the vertical profiles. In Table 3.3 the interpretation for easterly (westerly) momentum transfer refers to air moving from east to west (west to east). Similarly, northerly (southerly) momentum transfer refers to air moving from north to south (south to north). The temptation to visualize structure based on this analysis should be avoided since results represent averages over long flight segments.

For the normalized alongwind component ($\overline{v'w'}/u^{*2}$) weak positive values are found below about 0.3 Z/Z_i for the LESS with strong negative values dominating in the middle portion of the PBL from 0.3 to 0.8 Z/Z_i. Results for the LESS are again in good agreement at low levels with those of the AMTEX indicating that shears were comparable (but slightly stronger for the AMTEX) near the surface for the two

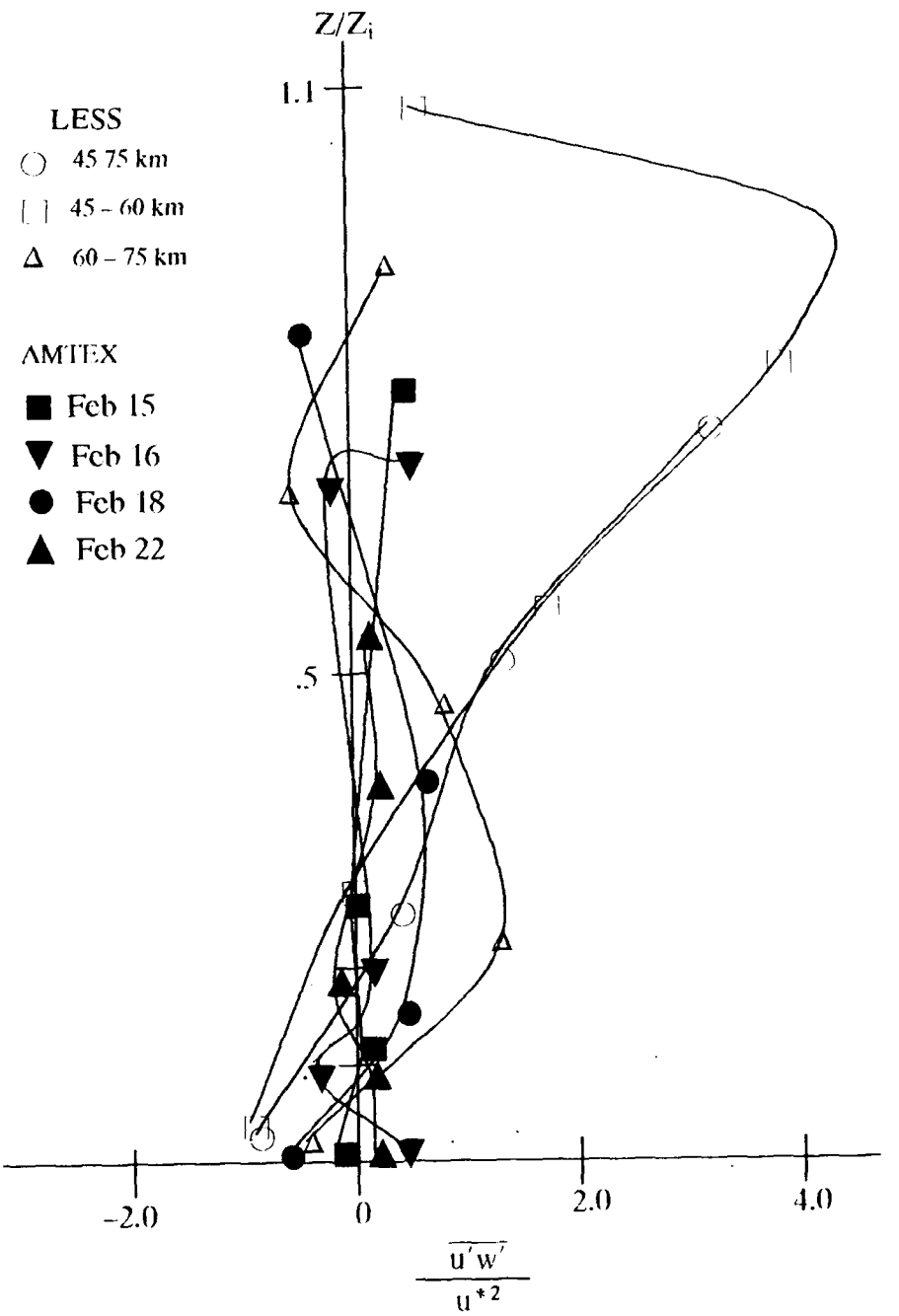

Figure 3.13 Average normalized crosswind component of stress for the LESS and AMTEX data.

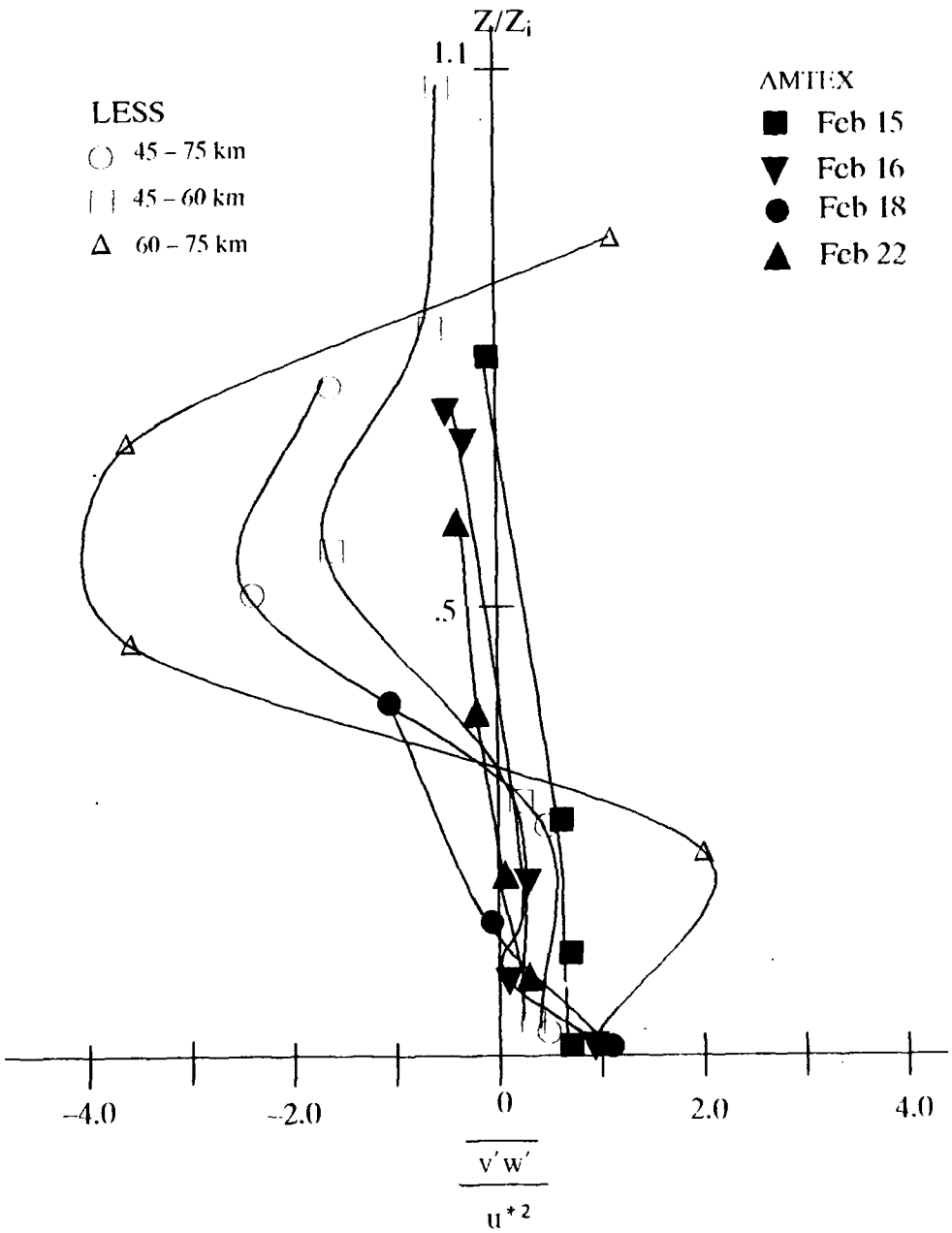

Figure 3.14 Average normalized alongwind component of stress for the LESS and AMTEX data.

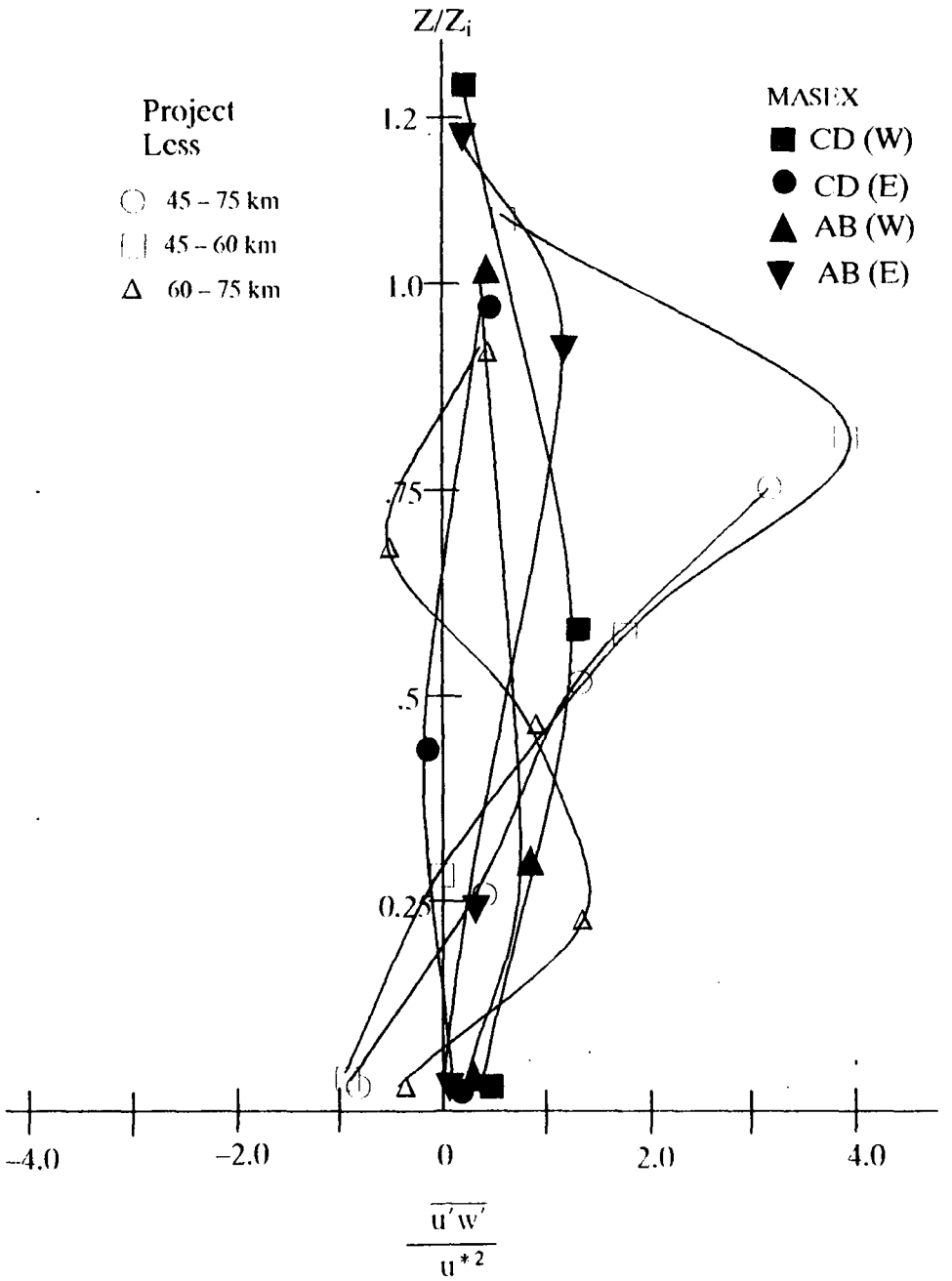

Figure 3.15 Average normalized crosswind stress for the LESS and MASEX data.

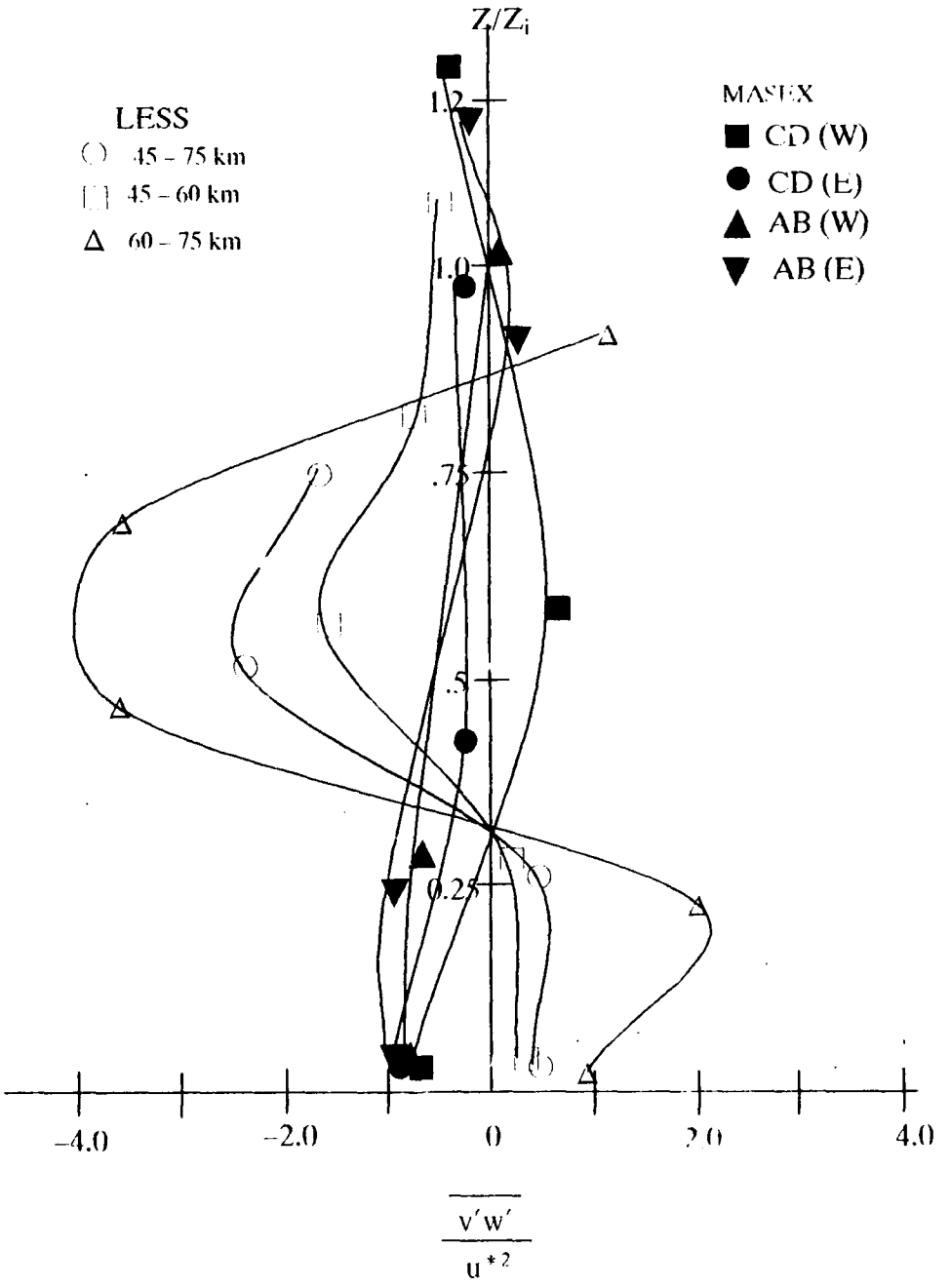

Figure 3.16 Average normalized alongwind stress for the LESS and MASEX data.

Table 3.4 Results from analysis of sign of u', v' and w' for covariances.

Covariances (45 – 75 km)

Flight Level	Sign of $\overline{u'w'}$	Percentage of $\overline{u'w'}$ with w'<0	w'>0	Average Sign of u'/ w'	Physical Interpretation
4	+	50.07	49.93	– / –	Downward trans. of easterly momentum
3	+	44.59	55.41	+ / +	Upward trans. of westerly momentum
2	+	55.41	44.59	– / –	Downward trans. of easterly momentum
1	–	41.09	58.91	– / +	Upward trans. of easterly momentum.

Flight Level	Sign of $\overline{v'w'}$	Percentage of $\overline{v'w'}$ with w'<0	w'>0	Average Sign of v'/ w'	Physical Interpretation
4	–	50.43	49.57	+ / –	Downward trans. of southerly momentum
3	–	54.86	45.14	+ / –	Downward trans. of southerly momentum
2	+	38.87	61.13	+ / +	Upward trans. of southerly momentum
1	+	44.20	55.80	+ / +	Upward trans. of southerly momentum.

Covariances (45 – 60 km)

Flight Level	Sign of $\overline{u'w'}$	Percentage of $\overline{u'w'}$ with w'<0	w'>0	Average Sign of u'/ w'	Physical Interpretation
5	+	48.09	51.91	+ / +	Upward transport of westerly momentum
4	+	36.41	63.59	+ / +	Upward transport of westerly momentum
3	+	44.29	55.71	+ / +	Upward trans. of westerly momentum
2	–	49.73	50.27	– / +	Upward trans. of easterly momentum.
1	–	41.89	58.11	– / +	Upward trans. of easterly momentum.

Flight Level	Sign of $\overline{v'w'}$	Percentage of $\overline{v'w'}$ with w'<0	w'>0	Average Sign of v'/ w'	Physical Interpretation
5	–	39.57	60.43	– / +	Upward transport of northerly momentum
4	–	53.93	46.07	+ / –	Downward transport of southerly momentum
3	–	53.07	46.93	+ / –	Downward transport of southerly momentum

Table 3.4, continued

Flight Level	Sign of $\overline{v'w'}$	Percentage of $v'w'$ with $w'<0$	$w'>0$	Average Sign of v' / w'	Physical Interpretation
2	+	43.37	56.63	+ / +	Upward trans. of southerly momentum.
1	+	44.73	55.27	+ / +	Upward trans. of southerly momentum.

Covariances (60 – 75 km)

Flight Level	Sign of $\overline{u'w'}$	Percentage of $u'w'$ with $w'<0$	$w'>0$	Average Sign of u' / w'	Physical Interpretation
5	+	52.62	47.38	– / –	Downward transport of easterly momentum
4	–	34.50	65.50	– / +	Upward transport of easterly momentum
3	+	47.92	52.08	+ / +	Upward trans. of westerly momentum
2	+	50.49	49.51	– / –	Downward trans. of easterly momentum.
1	–	42.33	57.67	– / +	Upward trans. of easterly momentum.

Flight Level	Sign of $\overline{v'w'}$	Percentage of $v'w'$ with $w'<0$	$w'>0$	Average Sign of v' / w'	Physical Interpretation
5	+	53.43	46.57	– / –	Downward transport of northerly momentum
4	–	51.78	48.22	+ / –	Downward transport of southerly momentum
3	–	54.47	45.53	+	Upward transport of southerly momentum
2	+	40.58	59.42	+ / +	Upward trans. of southerly momentum.
1	+	43.42	56.88	+ / +	Upward trans. of southerly momentum.

cases. However, once again stronger shears for the LESS are indicated for the mid-portion of the PBL.

A comparison between the results for the LESS and the MASEX (figures 3.15 and 3.16) again show generally good agreement at low levels (at least as far as magnitude is concerned) but both the crosswind and alongwind shears are much stronger for the LESS at the mid-portion of the PBL. The crosswind shears at level 4 in

the LESS data may be due to the secondary maximum in buoyancy at this level (to be discussed later). The very strong alongwind stress from level 2 to level 3 (Figure 3.16) may be due to the transition from the subcloud to cloud layer at these levels.

Stull (1988) points out that buoyancy is one of the driving forces for turbulence in the PBL and results from thermals of warm air rising because they are less dense (positively buoyant) than there surrounding environment. Buoyancy is generally expressed in the following way:

$$B = \frac{g Z_i \, (\overline{w'\Theta'_v})}{w^{*3} \, \overline{\Theta}_v} \quad , \tag{3.8}$$

where $g \, \overline{w'\Theta'_v} \, / \, \overline{\Theta}_v$ is called the buoyancy flux. To see why this is equivalent to the normalized covariance of w and Θ_v, (i.e. $\overline{w'\Theta'_v} \, / \, w^* \, \Theta^*_v$), substitute the expression for w^* (equation 3.1), the free convective scaling velocity, into (3.8). After simplification, (3.8) reduces to:

$$B = \frac{\overline{w'\Theta'_v}}{(\overline{w'\Theta'_v})_1} = \frac{\overline{w'\Theta'_v}}{w^*\Theta^*} \quad . \tag{3.9}$$

The profiles of normalized buoyancy for the AMTEX and the LESS are in very good agreement in the lower half of the PBL, with nearly a linear decrease in the buoyancy with height up to 0.5 Z/Z_i (Figure 3.17) for both observational cases. In the case of the AMTEX, the normalized buoyancy continues to decrease from this height upward, but it does so more slowly than in the lower half of the PBL. For the LESS results, however, a sharp increase in the buoyancy is seen at level 4 for all segments but especially so for the 45 – 75 km and 45 – 60 km segments. The relatively large normalized buoyancy value at level 4 (nearly 90% of the surface

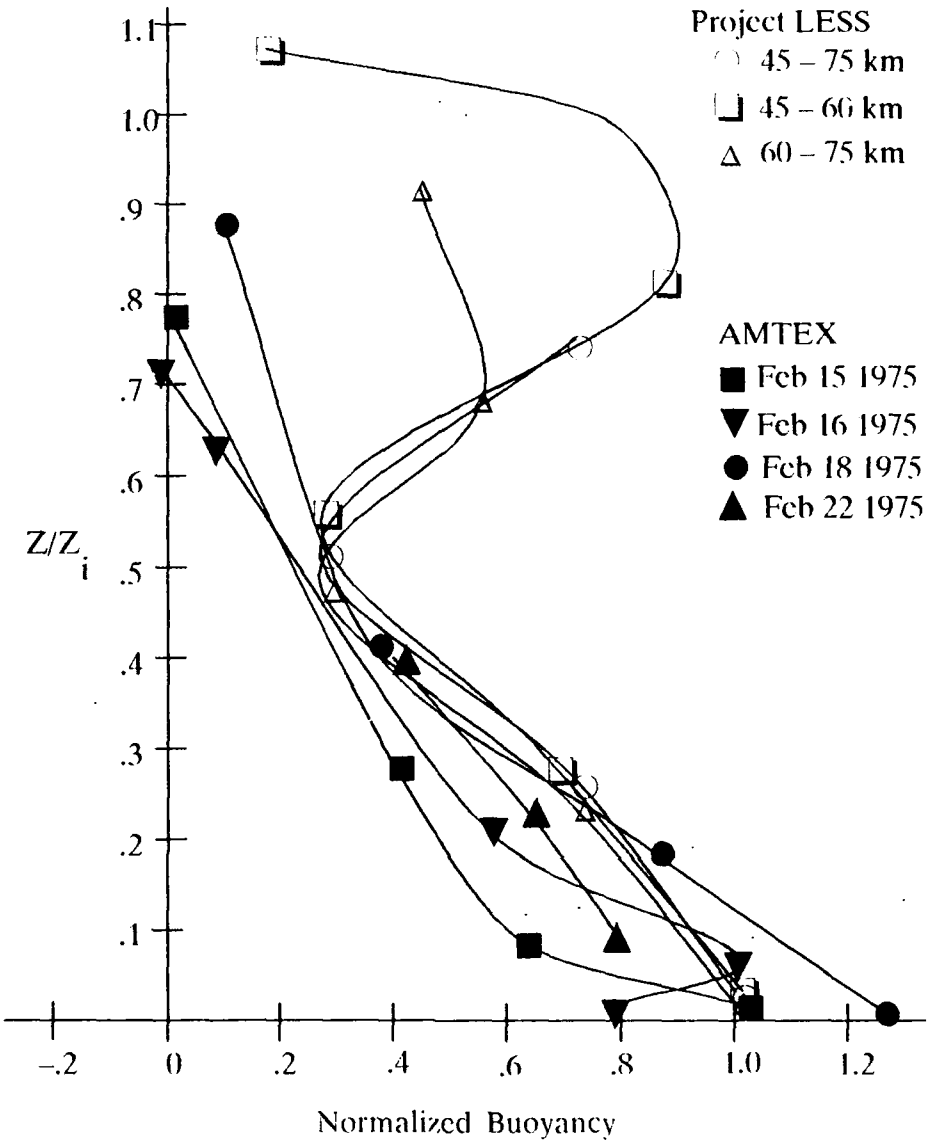

Figure 3.17 Vertical profile of the average normalized buoyancy for the AMTEX and the LESS field programs.

value for the 45 – 60km segment) is most likely due to increased buoyancy caused by the release of latent heat due to condensation resulting from formation of precipitation within the clouds.

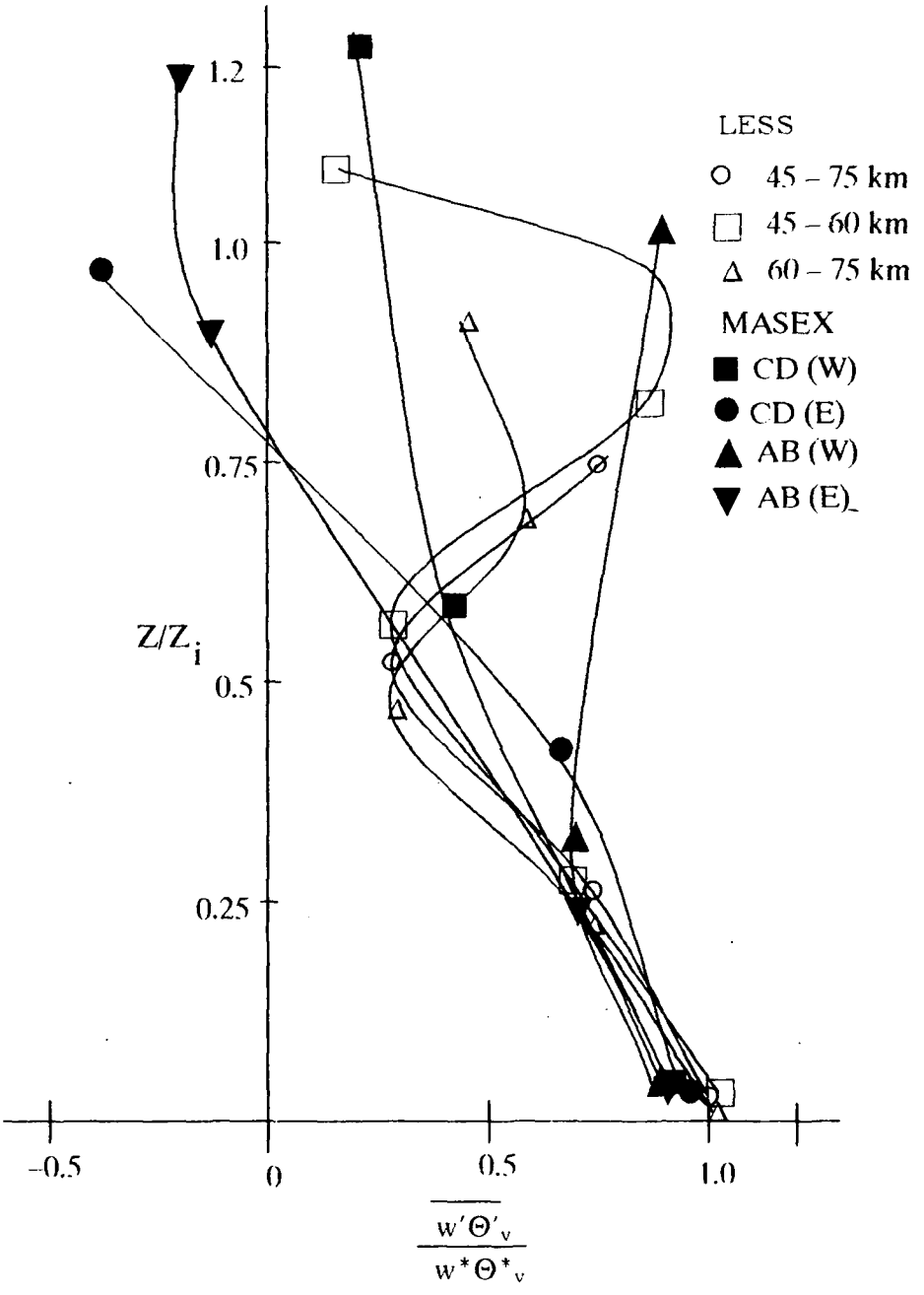

Figure 3.18 Vertical profile of the average normalized buoyancy for the MASEX and the LESS field programs

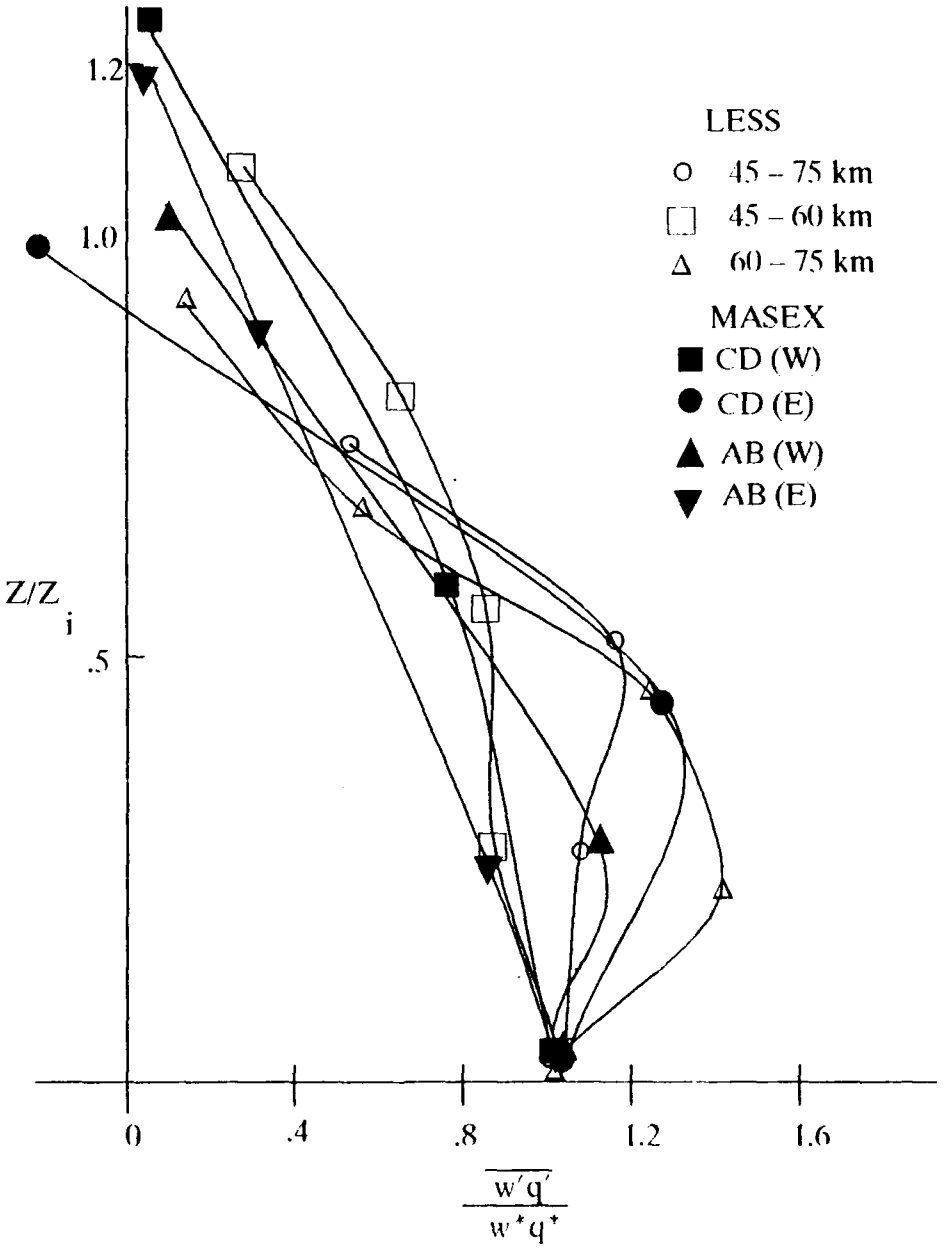

Figure 3.19 Average normalized vertical eddy moisture flux for the LESS and the MASEX.

Vertical profiles of the average normalized vertical eddy buoyancy flux for both the MASEX and LESS field programs are shown in Figure 3.18. Again, good agreement is generally found between the two studies in the lower portion of the PBL. The data point for the MASEX for AB(W) at 1.0 Z/Z_i is dismissed by Chou et al. as coming from a biased sample. According to them this sample included two cold thermals which were associated with an extremely large positive heat flux, due to descending return flow of a substantial amount of unmixed air. By removing the contribution of these two thermals, the heat flux was reduced from 90% to 8% of the surface value (Chou et al., 1986). With the exception of this data point the normalized buoyancy generally continues to decrease with height above 0.5 Z/Z_i.

The vertical profiles of the average normalized vertical eddy moisture flux from the MASEX and the LESS are shown in Figure 3.19. The profiles are very similar for the two case studies with the moisture flux generally decreasing with height. The especially strong fluxes at level 2 and, to a lesser extent, level 3 for the 60–75 km segment are due to large positive turbulent q values at these two levels as evidenced by the larger q variances for this segment at these levels.

3.6.2 Comparison of LESS Covariances with Model Results

A comparison between the vertical profile of the average normalized buoyancy for the LESS and Moeng's LES model is shown in Figure 3.20. Both the model and the LESS results are in quite good agreement in the lower half of the PBL but do not agree very well in the upper portion. As mentioned previously, the LESS profile shows a secondary maxima in the buoyancy at level 4 which is due to condensation–induced buoyancy. The LES model profile does not reflect this secondary maximum, probably because the moisture field effects were excluded from the model.

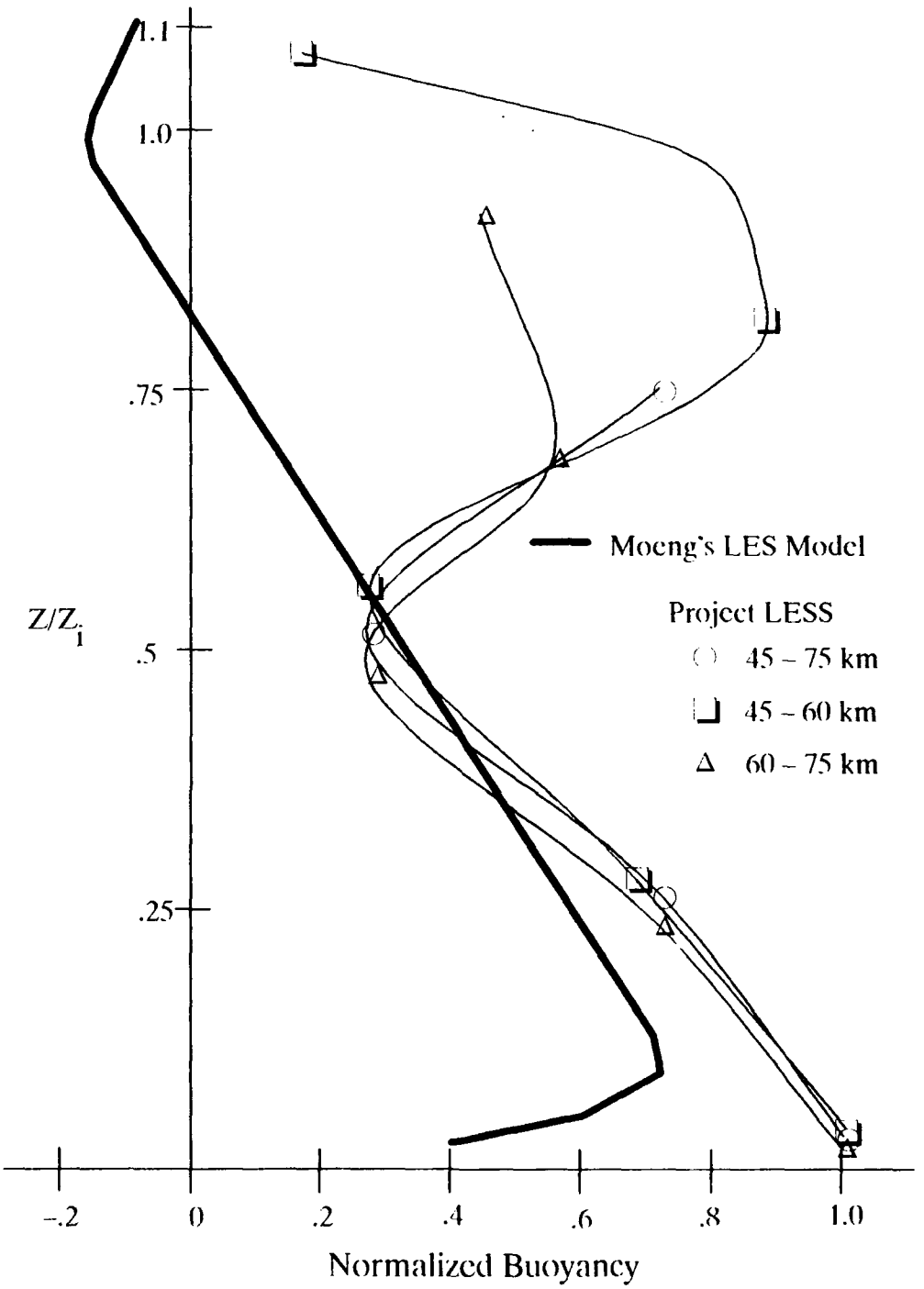

Figure 3.20 Vertical profile of the average normalized buoyancy for Moeng's LES model and the LESS

Figure 3.21 shows the vertical profile of the non–normalized buoyancy for the Deardorff model and for the Project LESS 60–75km segment (note the ordinate is this Figure is geometric height). The two profiles are very similar with a primary maximum near the surface where heating is the greatest, followed by a decrease with height extending from the subcloud layer to the cloud layer. Both profiles indicate a secondary maximum which is weaker than its respective surface counterpart (but still significant) that is most likely due to the release of the latent heat of condensation in the upper portion of the PBL.

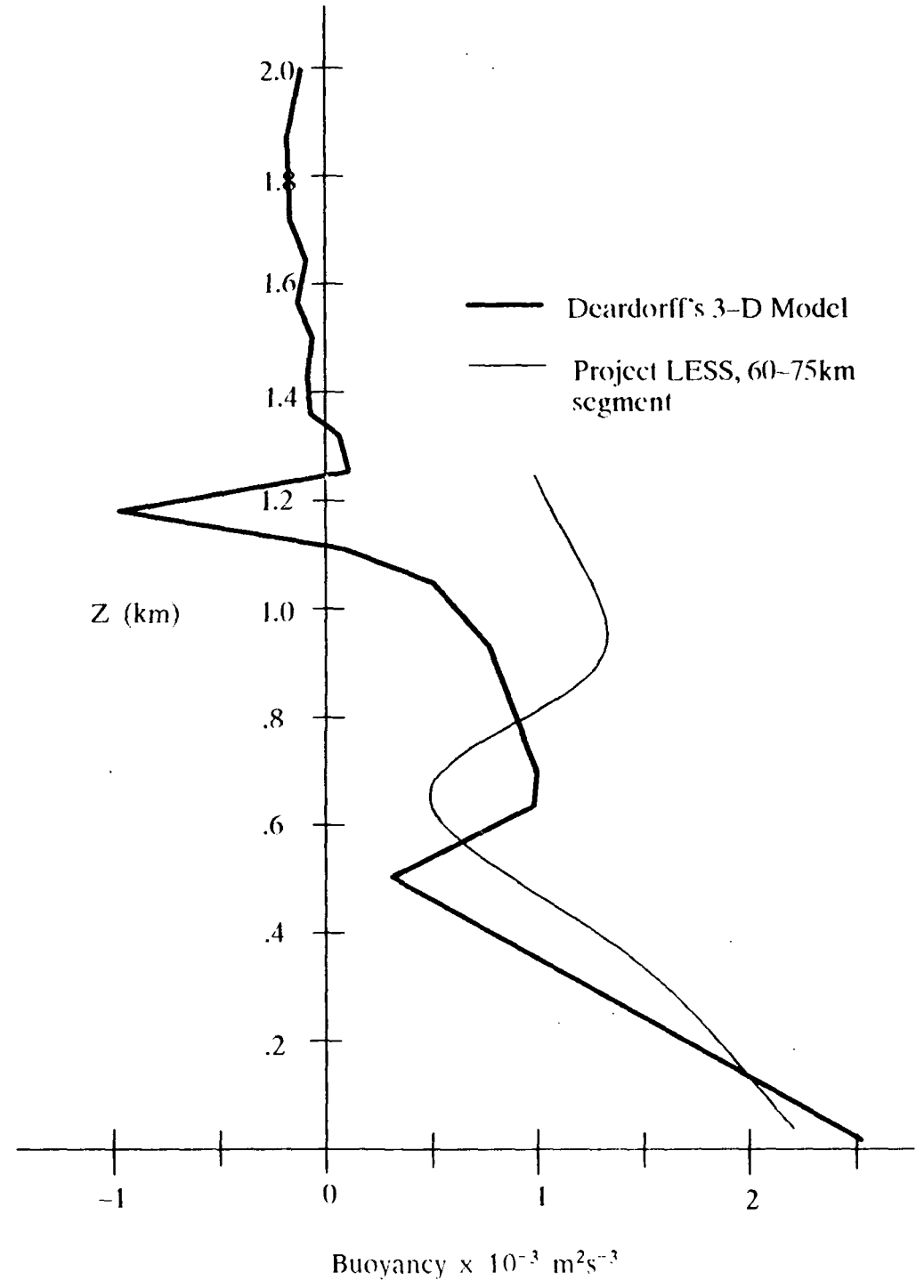

Figure 3.21 Vertical profile of the average non-normalized buoyancy for Deardorff's model and the Project LESS 60–75km segment.

3.7 Turbulence Kinetic Energy

No analysis of a convective PBL would be complete without a discussion of the turbulent kinetic energy (TKE). The TKE provides a measure of the intensity of turbulence and is directly related to the momentum, heat, and moisture transport through the boundary layer (Stull, 1988).

The turbulence kinetic energy per unit mass (TKE/m) is defined in Equation 3.10 below:

$$\frac{TKE}{m} = \frac{1}{2}(u'^2 + v'^2 + w'^2). \qquad (3.10)$$

For the sake of brevity, the turbulence kinetic energy per unit mass will be hereafter referred to as *simply TKE with the "per unit mass" understood.* It isn't difficult to see the relationship between the TKE and the variances of the u, v and w–wind components shown earlier in this chapter; *the TKE is equal to one–half the sum* of these variances. The average TKE then is just one–half the average of the sum of variances of the three wind components as shown in equation 3.11:

$$\overline{TKE} = \frac{1}{2}\overline{(u'^2 + v'^2 + w'^2)}. \qquad (3.11)$$

In a Type I CTBL, turbulent kinetic energy is produced by buoyancy and/or wind shear and is transported by the mean wind (advection) and/or by the turbulent eddies (turbulent transport). TKE may also be redistributed by the pressure perturbations taking place within the PBL. TKE is destroyed or lost through viscous dissipation by the smallest eddies through the energy cascade process described earlier.

The TKE can be easily broken down into its components and other terms to further illustrate the makeup of TKE as described in the equations below:

Average horizontal component of TKE: $\overline{TKE_h} = \frac{1}{2}(\overline{u'^2} + \overline{v'^2})$ (3.12)

Average vertical component of TKE: $\overline{TKE_v} = \frac{1}{2}(\overline{w'^2})$ (3.13)

Average vertical eddy transport of TKE. $\overline{w'TKE} = \frac{\overline{w'}}{2}(\overline{u'^2} + \overline{v'^2} + \overline{w'^2})$ (3.14)

Average vertical eddy transport of the horizontal component of TKE: $\overline{w'TKE_h} = \frac{\overline{w'}}{2}(\overline{u'^2} + \overline{v'^2})$ (3.15)

Average vertical eddy transport of the vertical component of TKE: $\overline{w'TKE_v} = \frac{\overline{w'}}{2}(\overline{w'^2})$ (3.16)

Ratio of the average vertical eddy transport of the horizontal component of TKE to the average vertical eddy transport of the vertical component of TKE: $\frac{\overline{w'TKE_h}}{\overline{w'TKE_v}} = \frac{\overline{w'}(\overline{u'^2} + \overline{v'^2})}{\overline{w'}(\overline{w'^2})}$ (3.17)

Table 3.5 Project LESS boundary layer normalized average TKE statistics

TKE Statistics (45 – 75 km)

Z_i = 1240m, w^* = 1.4684 ms^{-1}

$\frac{Z}{Zi}$	$\frac{\overline{TKE}}{w^{*2}}$	$\frac{\overline{TKE_h}}{w^{*2}}$	$\frac{\overline{TKE_v}}{w^{*2}}$	$\frac{\overline{w'TKE}}{w^{*3}}$	$\frac{\overline{w'TKE_h}}{w^{*3}}$	$\frac{\overline{w'TKE_v}}{w^{*3}}$	$\frac{\overline{w'TKE_h}}{\overline{w'TKE_v}}$
0.9935	(Convective and non-convective data not averaged)						
0.7500	0.7887	0.5037	0.2850	0.0720	0.0008	0.0711	0.0116
0.5161	0.6801	0.3967	0.2834	0.0825	0.0136	0.0689	0.1969
0.2581	0.9383	0.6089	0.3294	0.2288	0.0496	0.1792	0.2770
0.0403	0.6376	0.3651	0.2726	0.2091	0.0361	0.1731	0.2083

Table 3.5, continued

TKE Statistics (45 – 60 km)

Z_i = 1140m, w^* = 1.4445 ms $^{-1}$

$\frac{Z}{Zi}$	$\frac{\overline{TKE}}{w^{*2}}$	$\frac{\overline{TKE_h}}{w^{*2}}$	$\frac{\overline{TKE_v}}{w^{*2}}$	$\frac{\overline{w'TKE}}{w^{*3}}$	$\frac{\overline{w'TKE_h}}{w^{*3}}$	$\frac{\overline{w'TKE_v}}{w^{*3}}$	$\frac{\overline{w'TKE_h}}{\overline{w'TKE_v}}$
1.0807*	0.6014	0.4969	0.1045	0.1152	-0.0130	0.1283	-0.1016
0.8158	0.8435	0.5239	0.3196	0.2578	0.1208	0.1370	0.8815
0.5614	0.6790	0.3939	0.2851	0.1053	0.0228	0.0825	0.2769
0.2807	0.7974	0.4877	0.3096	0.1747	0.0108	0.1639	0.0661
0.0439	0.6277	0.3323	0.2954	0.2349	0.0372	0.1977	0.1881

TKE Statistics (60 – 75 km)

Z_i = 1340m, w^* = 1.4754 ms $^{-1}$

$\frac{Z}{Zi}$	$\frac{\overline{TKE}}{w^{*2}}$	$\frac{\overline{TKE_h}}{w^{*2}}$	$\frac{\overline{TKE_v}}{w^{*2}}$	$\frac{\overline{w'TKE}}{w^{*3}}$	$\frac{\overline{w'TKE_h}}{w^{*3}}$	$\frac{\overline{w'TKE_v}}{w^{*3}}$	$\frac{\overline{w'TKE_h}}{\overline{w'TKE_v}}$
0.9194	0.5985	0.5290	0.0695	0.0003	-0.0044	0.0048	-0.9372
0.6940	0.5322	0.2908	0.2414	0.0479	0.0053	0.0426	0.1234
0.4776	0.6395	0.3534	0.2862	0.0556	-0.0059	0.0615	-0.0957
0.2388	0.6804	0.3389	0.3415	0.2316	0.0414	0.1902	0.2176
0.0373	0.5715	0.3172	0.2543	0.1851	0.0269	0.1581	0.1704

* Level 5 is above the convective PBL.

3.7.1 Comparisons among Observational Case Studies.

Figure 3.22 shows the vertical profile of the normalized average turbulence kinetic energy for the Project LESS. Maxima are found for all three segments at level 2 and at level 4 for the 45 – 75 km and 45 – 60 km segments. Interestingly, the maximum at level 2 does not occur at the level at which buoyancy is a maximum (level 1, Figure 3.20). The vertical profiles of the average normalized horizontal (Figure 3.23) and vertical (Figure 3.24) components of TKE indicate that the maximum at level 2 is due primarily to a corresponding maximum in the horizontal

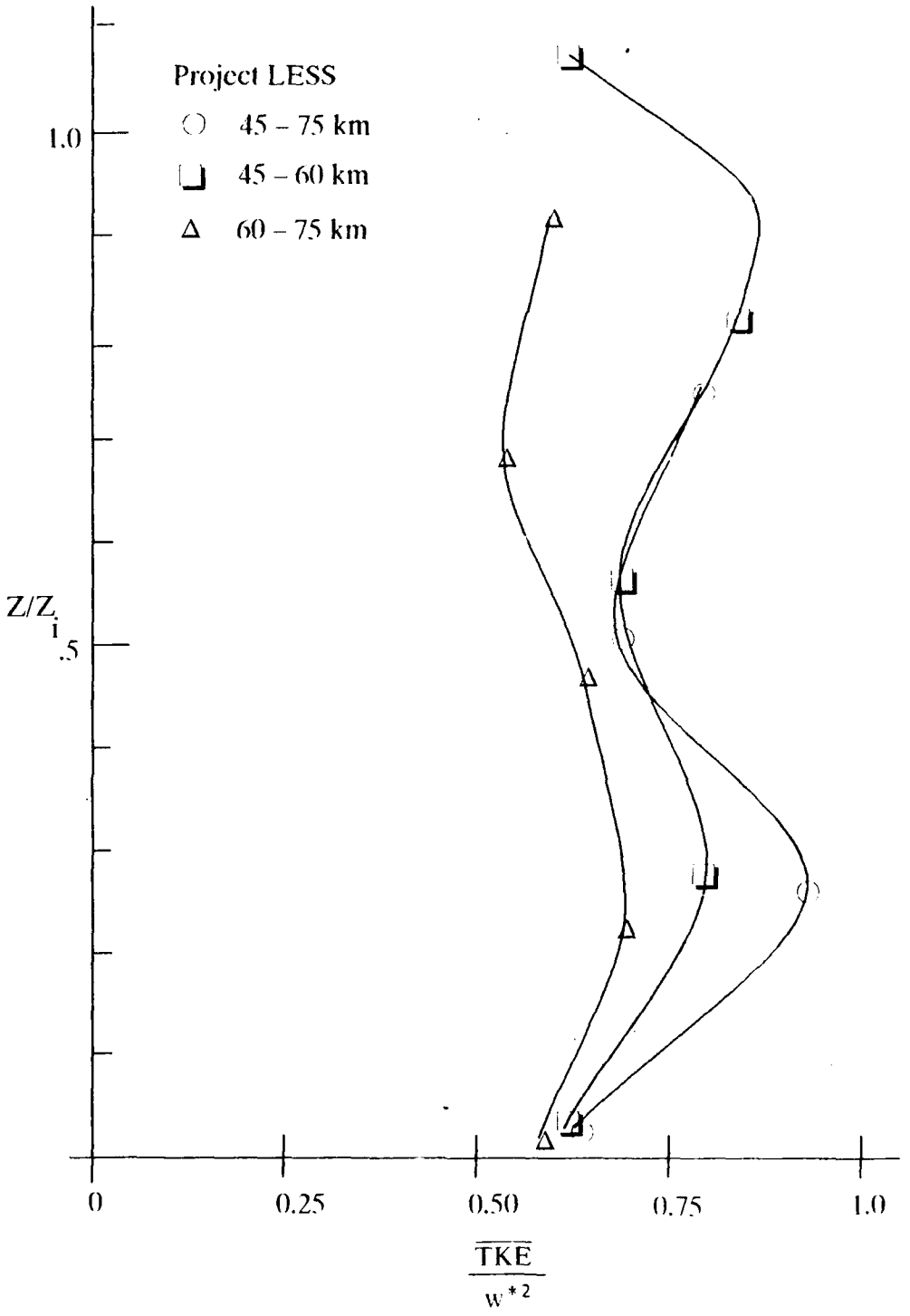

Figure 3.22 Vertical profile of the normalized average TKE for the Project LESS data.

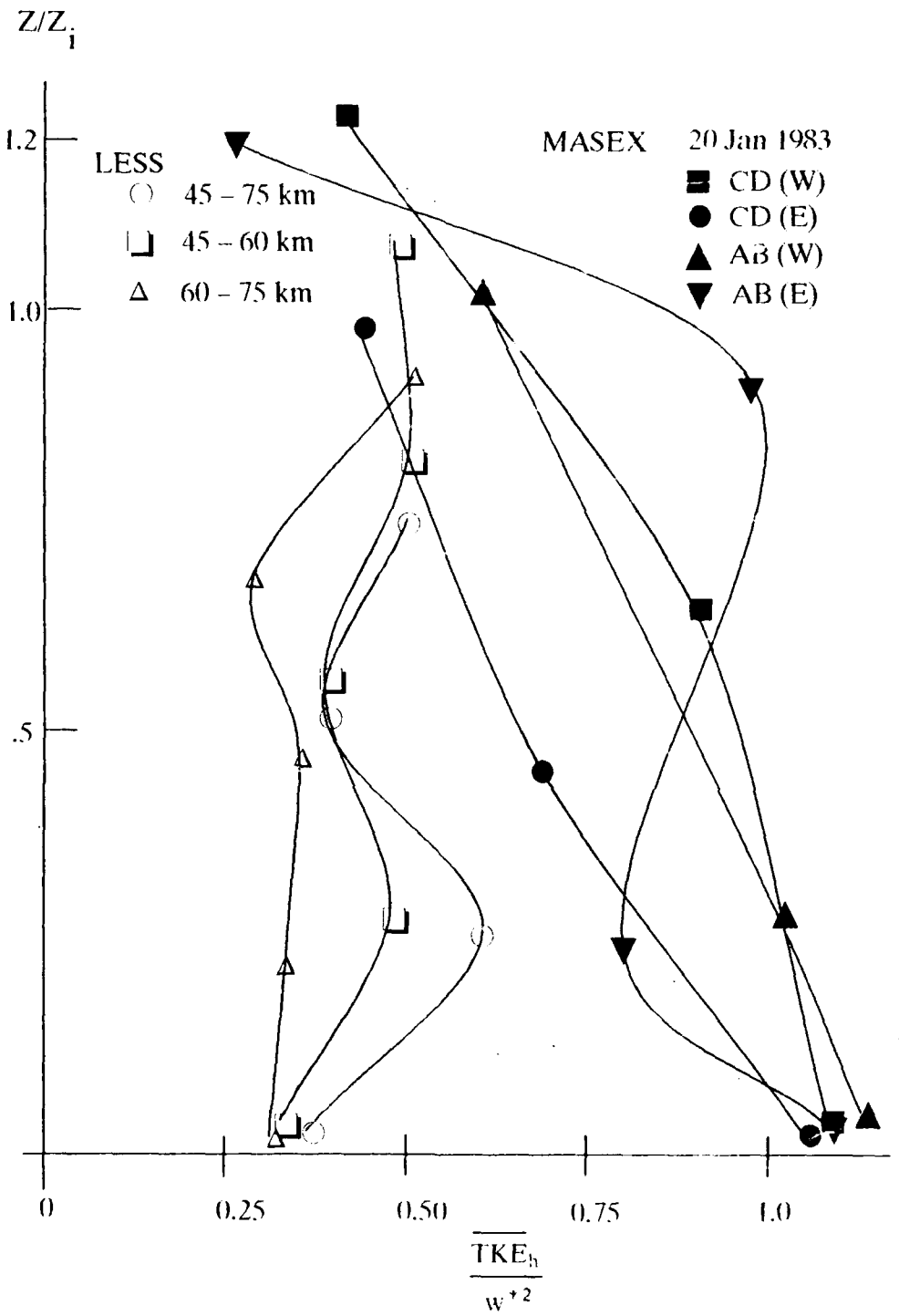

Figure 3.23 Vertical profile of the normalized average horizontal component of TKE for the LESS and MASEX.

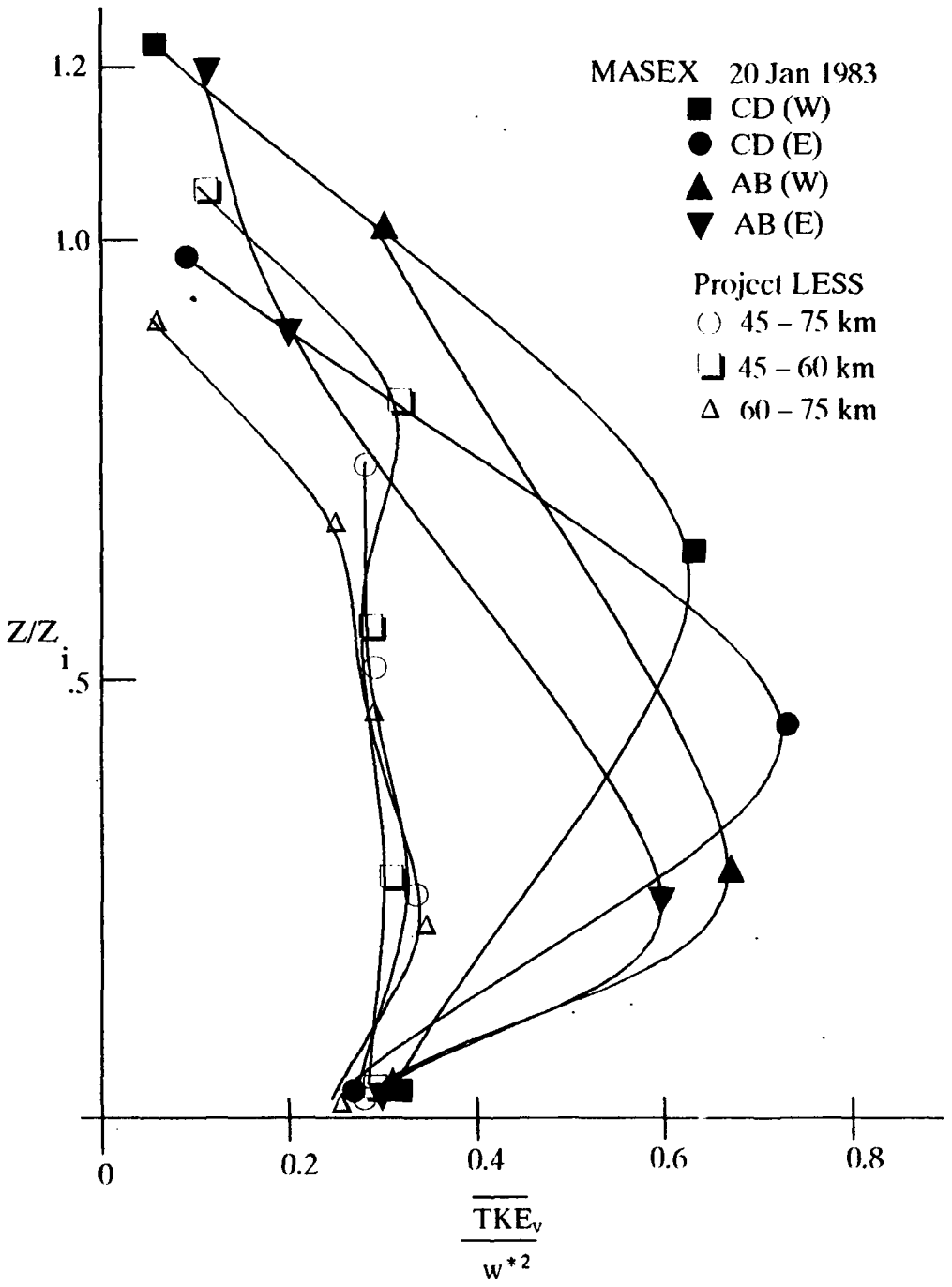

Figure 3.24 Vertical profile of the normalized average vertical component of TKE for the LESS and MASEX

component of TKE at this same level. The vertical profile of the vertical component of TKE on the other hand shows very little variability in the w variance except at level 5. By examining the u and v variances which make up the horizontal component of TKE it becomes evident that the v--component of variance is largely responsible for the maximum in TKE at level 2 since the v variance is between 5% (60–75 km segment) and 40% (45–75 km segment) larger than the u–component of variance. The second maximum at level 4 for the LESS data again appears to be due to the horizontal rather than the vertical component of TKE since the horizontal component is 63% (45 – 60km segment) to 76% (45 – 75km segment) larger than the vertical component. However, unlike the maximum at level 2, the maximum at level 4 owes its origin primarily to the u–component variance rather than the v–component. At level 4 the u variance is between 13% to 48% larger than the v variance. The u variance at level 4 is more than two times as strong as the w–component for the 45 – 60km segment but the two are comparable for the 45 – 75km segment.

A comparison between the LESS and the MASEX data for the normalized average horizontal and vertical components of TKE shows the values of the MASEX to be substantially larger (about 200% larger) in the lower half of the convective PBL but of comparable value in the upper one–third. This would indicate that for a given surface buoyancy flux (actually level 1 buoyancy flux for the LESS) as accounted for by the normalization by w^*, the MASEX PBL is dynamically more active than the LESS.

Figure 3.25 shows the vertical profile of the normalized average vertical flux of TKE for the LESS and MASEX cases. With a few exceptions, the vertical flux decreases with height for the LESS case with the maximum found at level 2. Below this maximum, there is more upward flux leaving the top of any given layer than

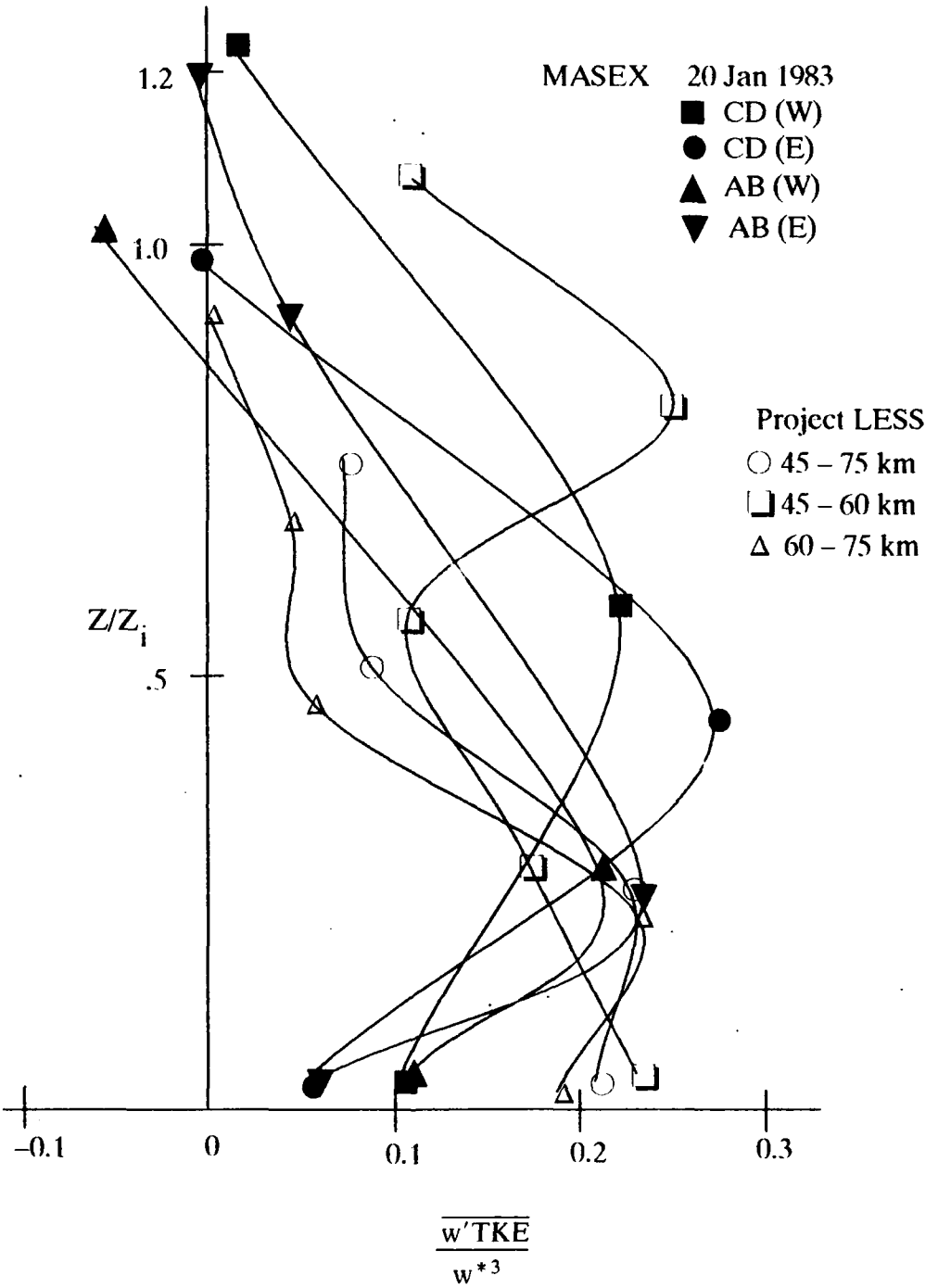

Figure 3.25 Vertical profile of the normalized average vertical flux of TKE for the LESS and MASEX cases.

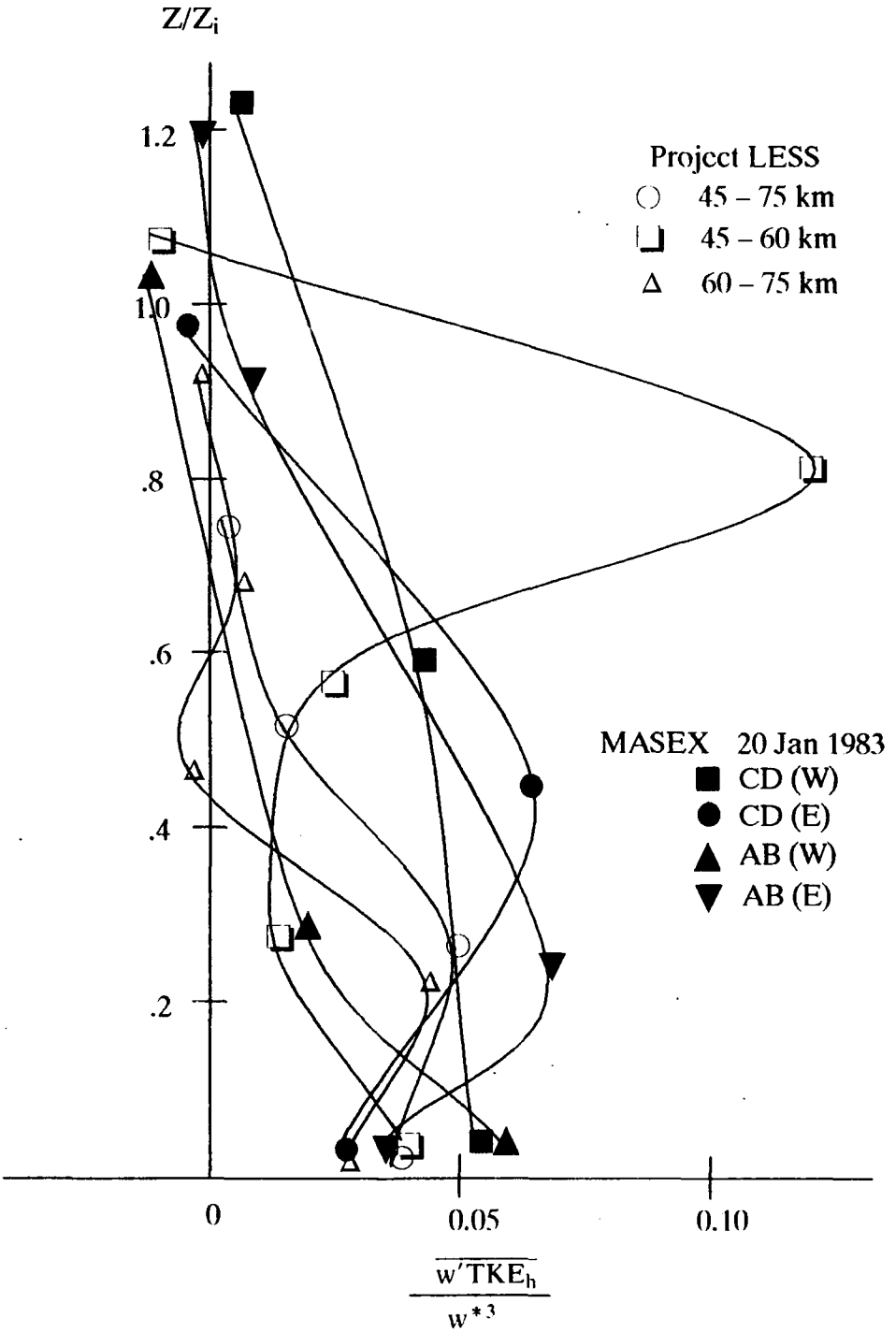

Figure 3.26 Vertical profile of the normalized average vertical flux of the horizontal component of TKE for the LESS and MASEX cases.

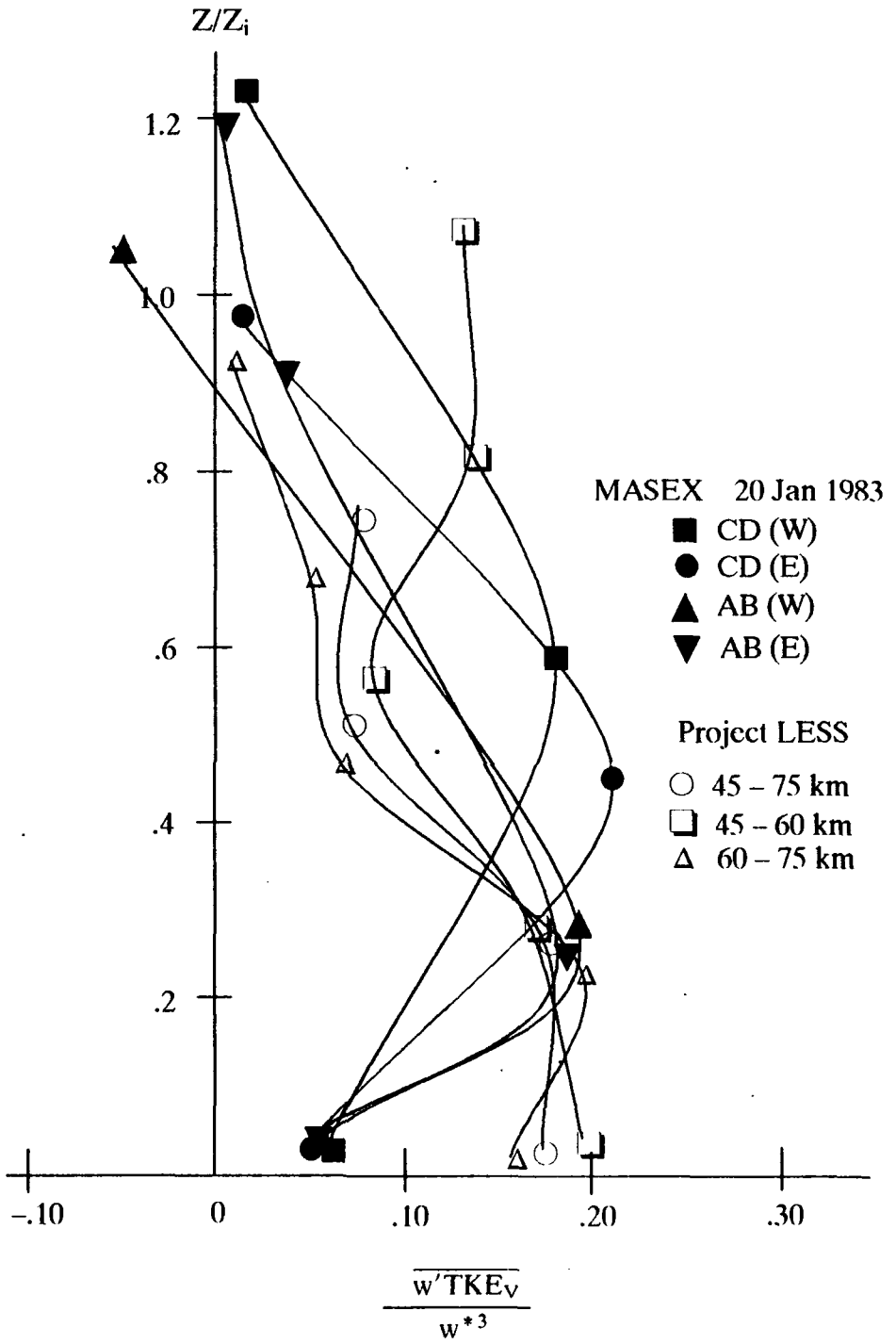

Figure 3.27 Vertical profile of the normalized average vertical flux of the vertical component of TKE for the LESS and MASEX

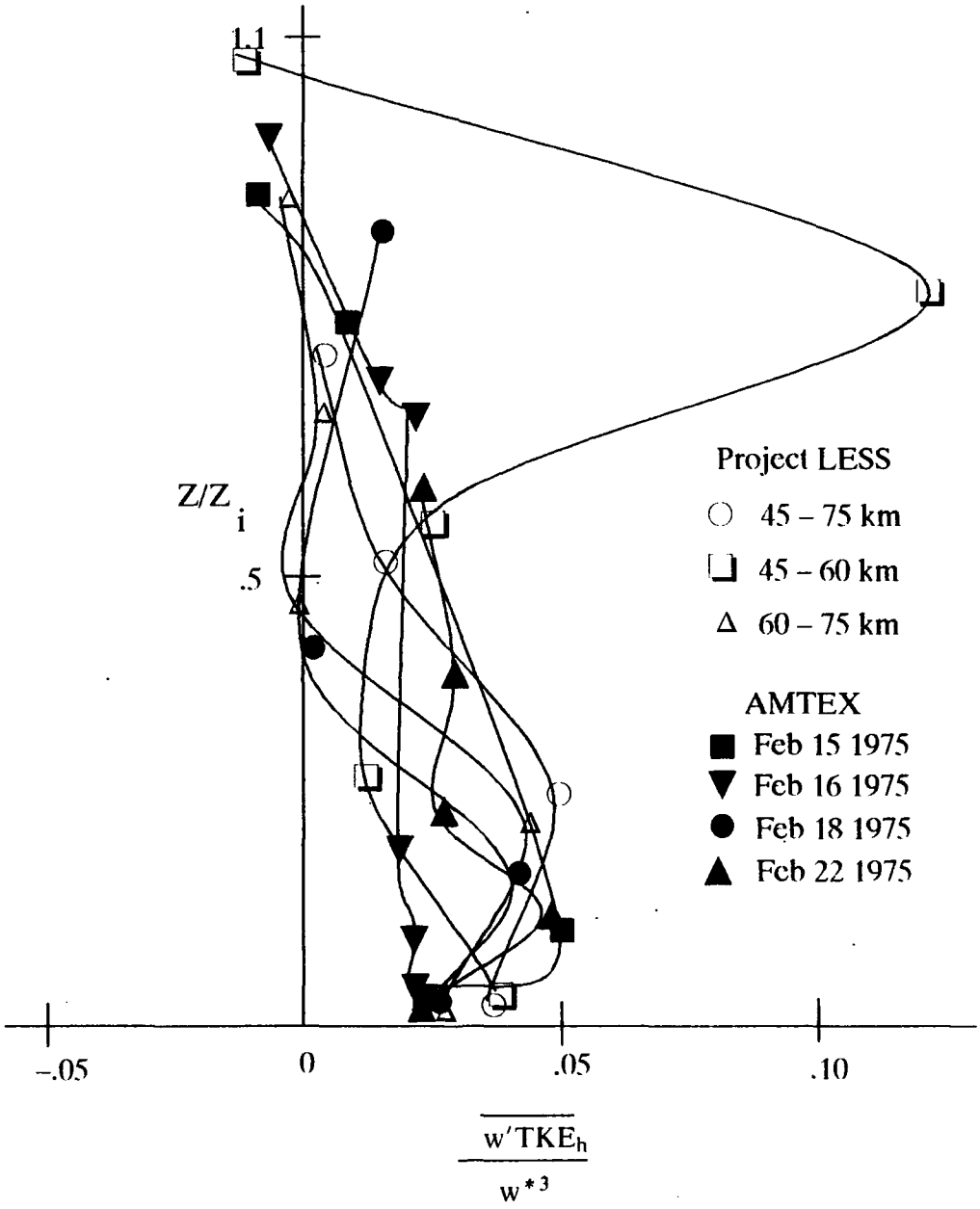

Figure 3.28 Vertical profile of the normalized average vertical flux of the horizontal component of TKE for the LESS and AMTEX.

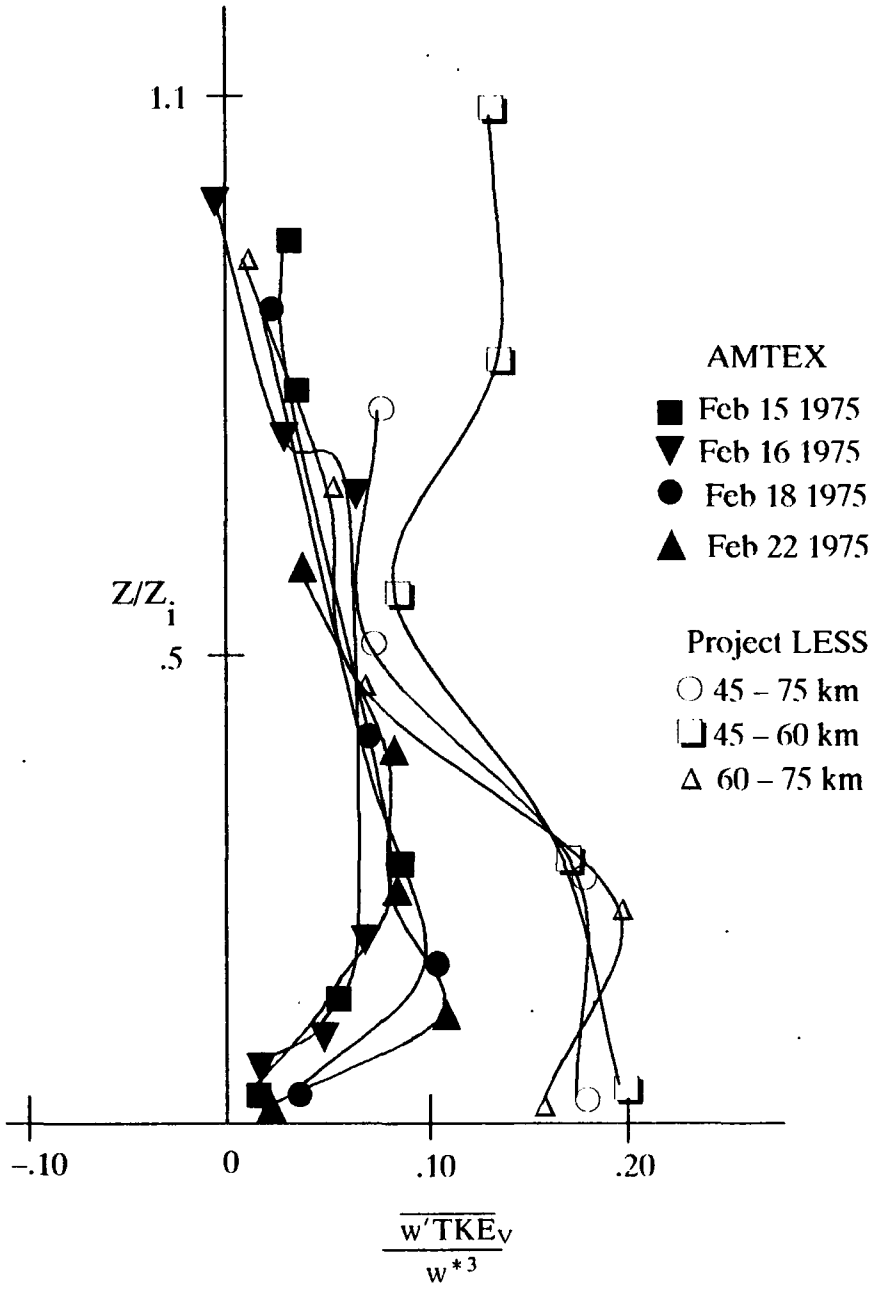

Figure 3.29 Vertical profile of the normalized average vertical flux of the vertical component of TKE for the LESS and AMTEX.

enters from below, resulting in a net divergence or loss of TKE. Above this maximum, there is a net convergence or gain of TKE. As a result, some of the the TKE produced at the lowest levels where buoyancy is a maximum is transported to higher levels. A second maximum is found at level 4 for the LESS profile for the 45–60km segment. This peak appears to be due equally to the vertical flux of horizontal TKE for which this same maximum is found (Figure 3.26) and the vertical flux of vertical TKE (Figure 3.27). Results for the LESS case study compare favorably with those of the MASEX study with both showing that the vertical transport of the vertical component of TKE is two to four times stronger than the vertical transport of the horizontal component.

The vertical profiles of the normalized average vertical flux of the horizontal and vertical components of TKE are shown in Figure 3.28 and 3.29 respectively for the LESS and the AMTEX results of Lenschow et al. (1980). The vertical flux profiles for the horizontal component of TKE are very similar for the two case studies with the exception of the aforementioned strong maximum in the LESS at level 4 for the 45 – 60km segment. For the vertical flux of the vertical component of TKE, however, the LESS values are, with very few exceptions, larger than those for the Lenschow results for the AMTEX. This indicates that for a given buoyancy production the turbulent eddies for the LESS case are more efficient and capable at transporting the vertical component of TKE than are those for the AMTEX case. With regards to the vertical flux of horizontal TKE, the turbulent eddies appear to be approximately equal for both cases in terms of their ability to transport the TKE.

Figures 3.30 and 3.31 show the ratio of the vertical flux of velocity variance between the horizontal and the vertical components of TKE for the LESS and AMTEX (Figure 3.30) and the LESS and MASEX (Figure 3.31). For both the AMTEX

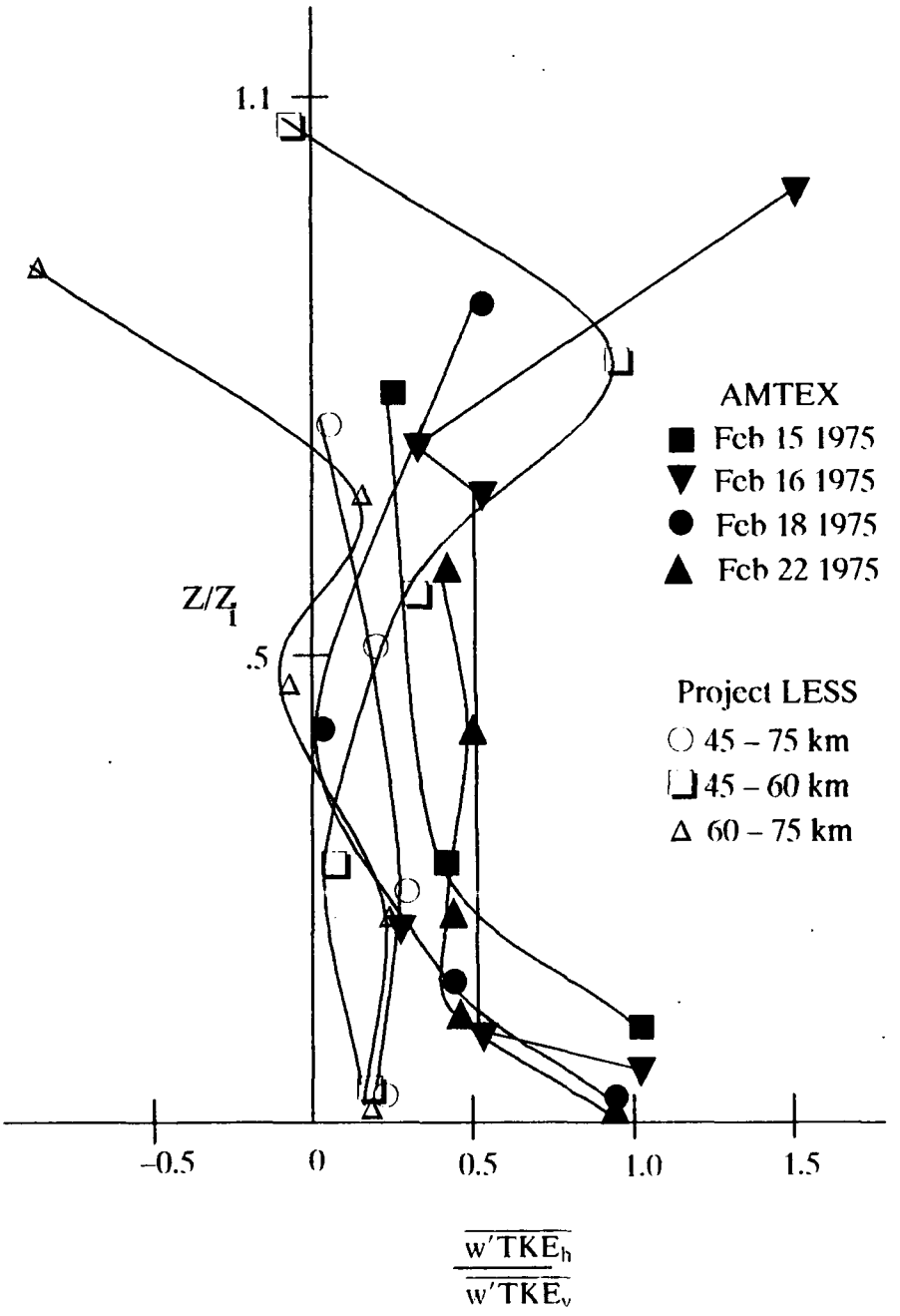

Figure 3.30 Vertical profile of the ratio of the average vertical flux of the horizontal component of TKE to the average vertical flux of the vertical component of TKE for the LESS and AMTEX results.

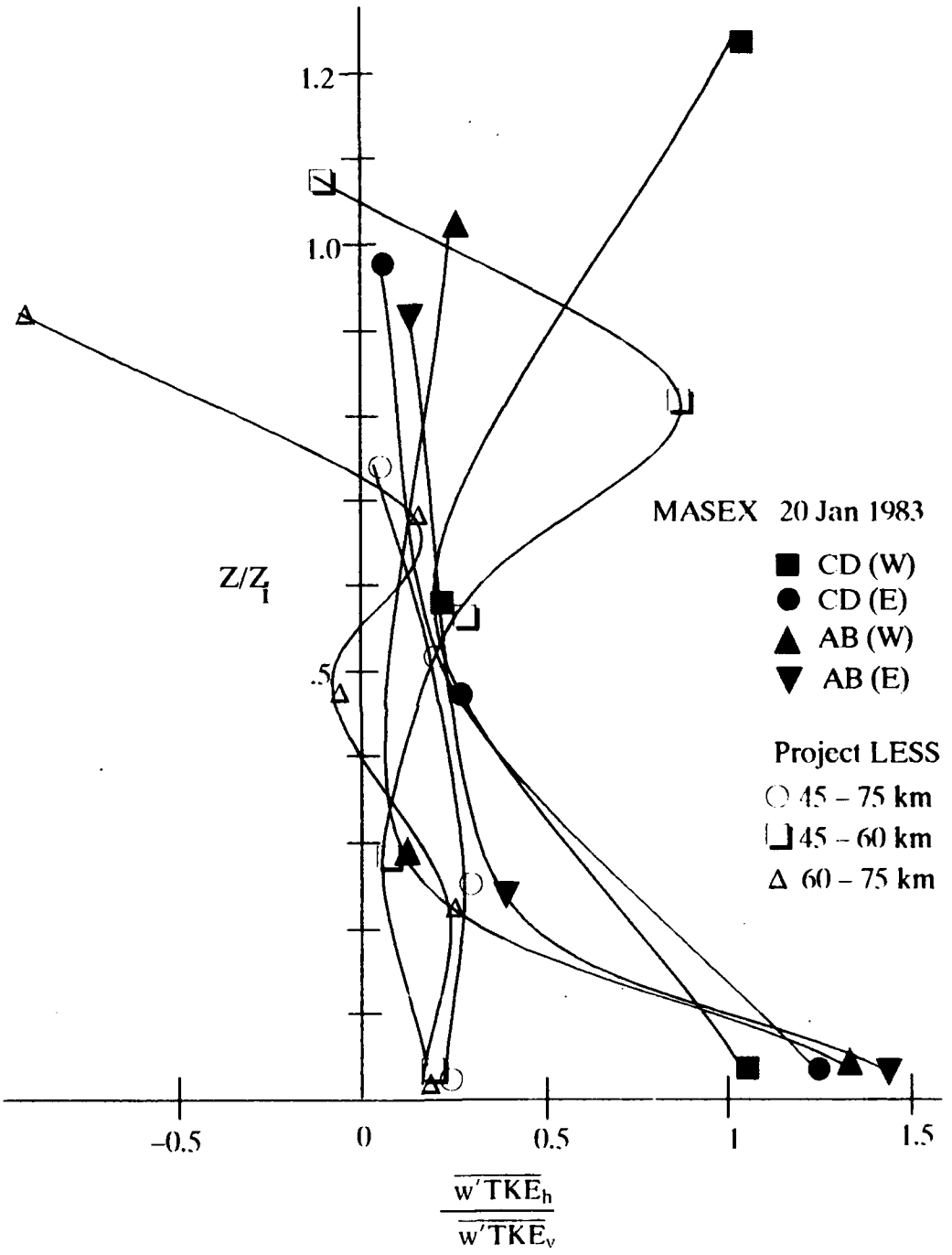

Figure 3.31 Vertical profile of the ratio of the average vertical flux of the horizontal component of TKE to the average vertical flux of the vertical component of TKE for the LESS and MASEX case studies

and MASEX cases the ratio is nearly unity at the lowest level indicating that each component contributes equally to turbulent transport at this level. For the LESS, however, the ratio is less than unity indicating that $\overline{w'^3}$ contributes more to turbulent transport at this level than for either the AMTEX or MASEX case. This is a result of a stronger vertical transport of vertical variance in the LESS over that of the AMTEX and MASEX. The ratio drops to less than unity in the mid–portion of the PBL for both the AMTEX and the MASEX results indicating that $\overline{w'^3}$ contributes more to turbulent transport in this portion of the PBL for both cases. For the LESS case the ratio remains nearly constant with height until level 5 is reached where the ratio for both the 45 – 60km and 60 – 75km segments becomes negative.

3.7.2 Comparisons between the LESS and Model results

Figure 3.32 gives the vertical profile of the normalized average horizontal component of TKE for the Project LESS study and the 3–D model of Deardorff (1980). The horizontal component is generally stronger for the LESS study than for Deardorff's simulation of day 33 of the Wangara experiment indicating the former has stronger turbulence intensity in the horizontal component.

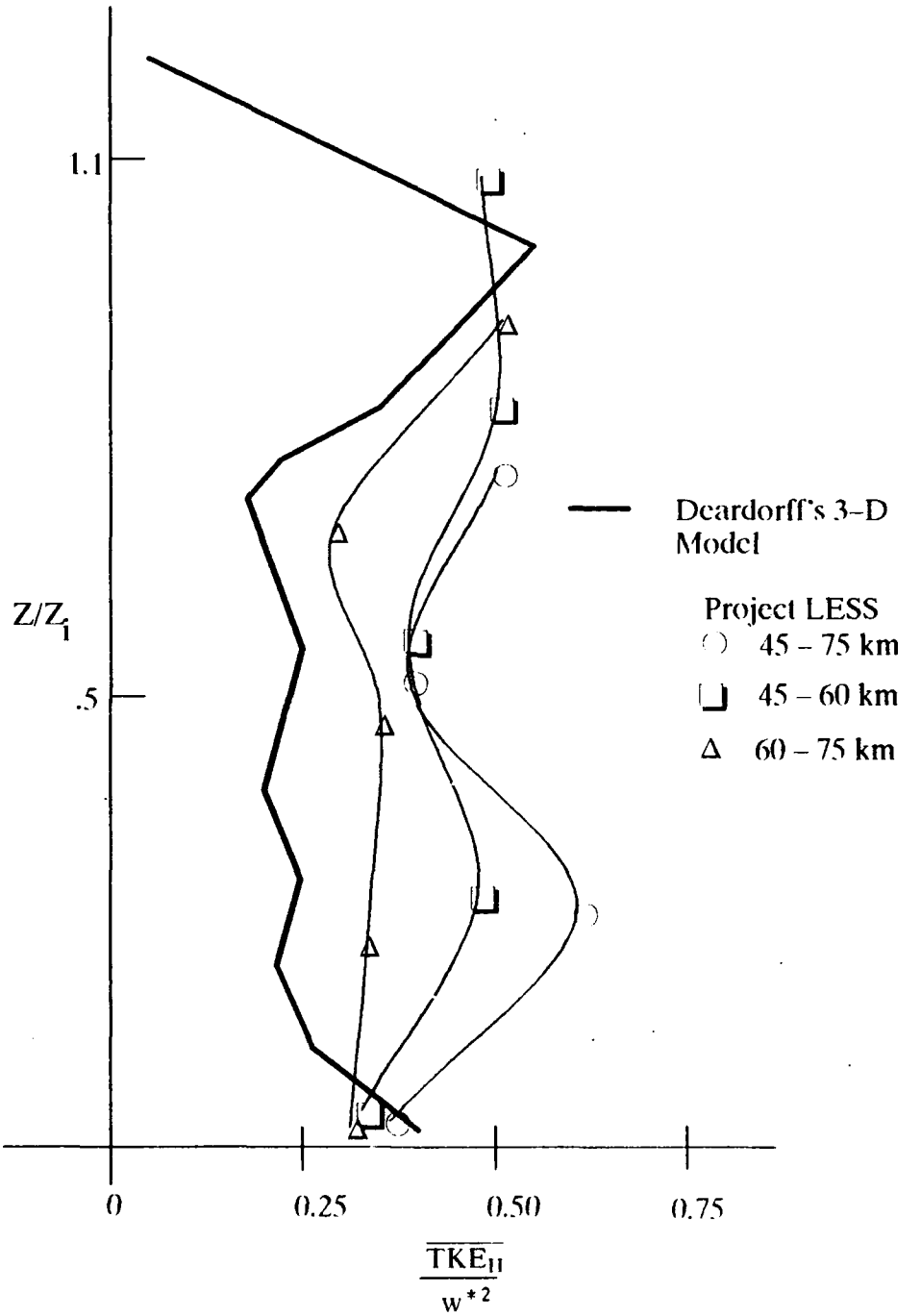

Figure 3.32 Vertical profile of the normalized average horizontal component of TKE for the LESS and Deardorff's 3–D model.

3.8 Skewness

In statistics, skewness is often used as a measure of the extent to which items are symmetrically distributed. One way to study the symmetry (or asymmetry) of a frequency distribution is by examining the mode, median and mean where the mode is the location on the scale which has the greatest concentration of items and the median has roughly half of the items lying below and above it. (Neter et al., 1988)

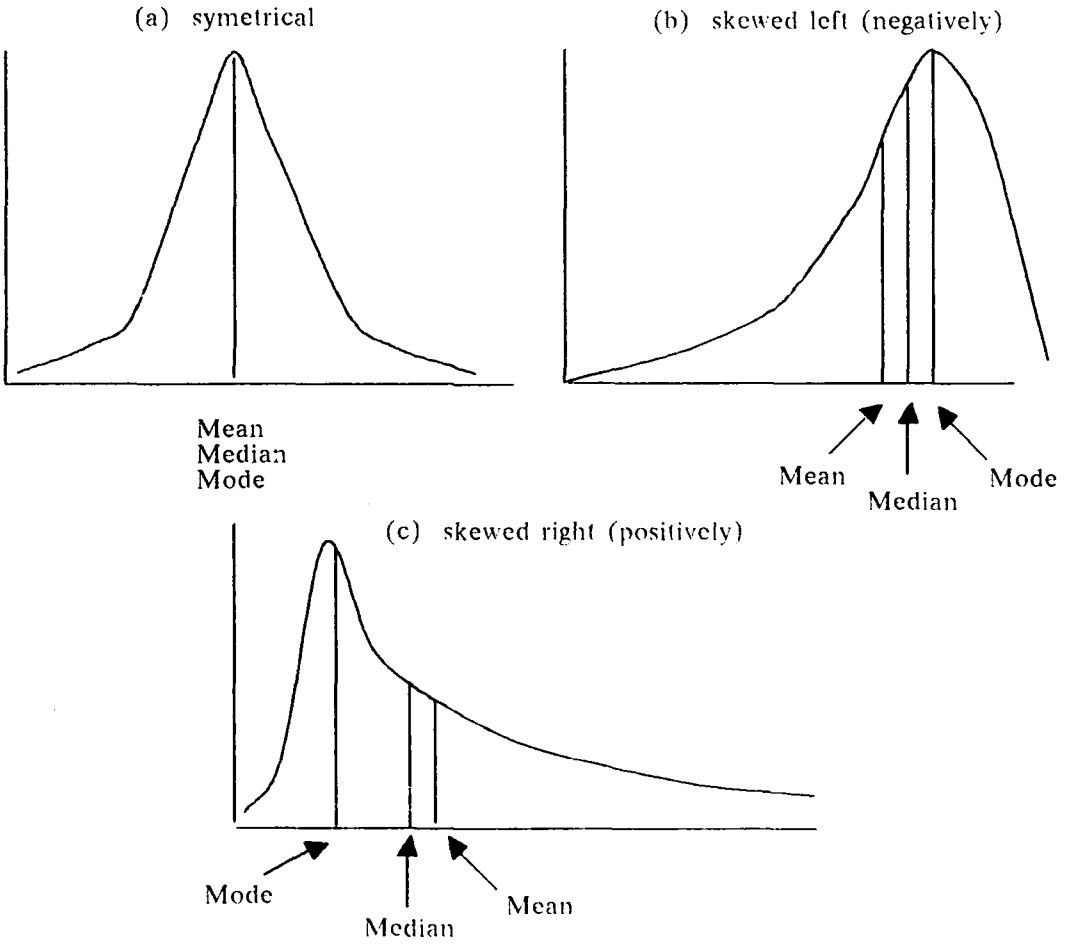

Figure 3.33 Examples of symmetrical and skewed unimodal frequency distributions. From Neter et al. , 1988.

The three frequency polygons in Figure 3.33 show the relative positions of the mean, median and mode for a unimodal frequency distribution with varying degrees and direction of symmetry. Figure 3.33a shows a symmetrical distribution for which the mean, median and mode are identical. Figures 3.33b and 3.33c show frequency distributions skewed to the left (negatively) and skewed to the right (positively) respectively. The mean in each case is typically furthest out toward the tail of the distribution because of its sensitivity to large and small values and the median is between the mean and the mode.

Mathematically, the skewness can be expressed for a set of items X_i for i = 1 to n as shown below:

$$S_x = \frac{m_3}{s^3} \qquad (3.12)$$

$$\text{where } m_3 = \sum_{i=1}^{n} \frac{(X_i - \overline{X})^3}{n-1} \quad \text{and} \quad s = \sqrt{\sum_{i=1}^{n} \frac{(X_i - \overline{X})^2}{n-1}} \; .$$

In other words, the standardized skewness measure, S_x, is the average third moment about the mean divided by the standard deviation cubed. Because of the cube in the numerator of S_x, large deviations $X_i - \overline{X}$ will dominate the sum in the numerator of S_x. If the large deviations are mostly positive, the skewness will be positive, if they are largely negative the skewness will be negative (the denominator is always positive). Because large deviations appear in the tail portion of the frequency distribution, one can see from Figure 3.33 that skewness will be positive or negative according to whether the direction of skewness is positive (right) or negative (left) (Neter et al., 1988).

Skewness is a useful measure in the PBL because it gives an indication of

the structure of the motion. For instance, if $\overline{w} = 0$ and if $S_w > 0$, updrafts are narrower and stronger than surrounding downdrafts (Moeng and Rotunno, 1990). In the sections that follow, vertical profiles of the skewness of all five meteorological parameters (u, v, w, Θ_v and q) will be presented with comparisons made between the LESS results and other case studies and between the LESS and model results.

3.8.1 U, V, Θ_v and Q Skewness

In this section, vertical profiles of skewness will be shown and discussed for u, v, Θ_v and q for the Project LESS. Results for the vertical velocity, w, will be presented in this section, but a discussion of the vertical profiles will be held off until the following section.

Table 3.6 summarizes the skewness results for the Project LESS data sets. As has been the case for all the results presented thus far, skewness calculations have been done using data detrended using a second-degree polynomial fit. As a result, the mean for each variable is zero per the earlier discussion.

Table 3.6 Project LESS boundary layer skewness values.

Skewness (45 – 75 km)

Z_i = 1240m

$\frac{Z}{Z_i}$	S_u	S_v	S_w	$S_{\Theta v}$	S_q
0.9935		(Convective and non-convective data not averaged)			
0.7500	0.1447	0.3383	0.3305	0.2026	-1.9571
0.5161	0.0001	0.0390	0.3230	0.6821	0.1908
0.2581	-0.0763	-0.0058	0.6703	0.8875	0.4303
0.0403	0.1095	-0.0454	0.8601	1.1156	0.2190

Table 3.6, continued

Skewness (45 – 60 km)

Z_i = 1140m

$\frac{Z}{Z_i}$	S_u	S_v	S_w	$S_{\Theta v}$	S_q
1.0807*	0.1405	–0.7806	2.6846	–0.2075	–0.1307
0.8158	0.6884	0.3853	0.5363	0.3926	–2.5200
0.5614	0.1769	–0.0034	0.3833	0.8909	–0.2800
0.2807	–0.0869	0.0195	0.6726	1.4912	0.3502
0.0439	0.0989	0.0589	0.8709	1.3644	0.3016

Skewness (60 – 75 km)

Z_i = 1340m

$\frac{Z}{Z_i}$	S_u	S_v	S_w	$S_{\Theta v}$	S_q
0.9194	0.8798	–0.3387	0.1840	0.2729	–0.6543
0.6940	–0.2894	0.2191	0.2542	–0.0248	–1.6087
0.4776	–0.1429	0.0412	0.2839	0.3053	0.5389
0.2388	–0.0487	0.1255	0.6739	0.5613	0.8186
0.0373	0.1877	0.0599	0.8720	1.1556	0.2141

* Level 5 is above the convective PBL.

The vertical profile of the skewness of the u–wind component is shown in Figure 3.34 below. Skewness is weakly negative for level 1, indicating narrow regions of relatively strong westerly momentum surrounded by broad regions of generally weak easterly momentum. At level 2, just the opposite occurs; skewness is negative for all three segments, indicative of relatively strong narrow regions of easterly momentum surrounded by regions of broad, relatively weak westerly momentum. With the exception of the 60 – 75km segment at levels 2 and 3, the u–component of skewness is generally positive throughout the rest of the PBL and generally increases in strength with increasing height.

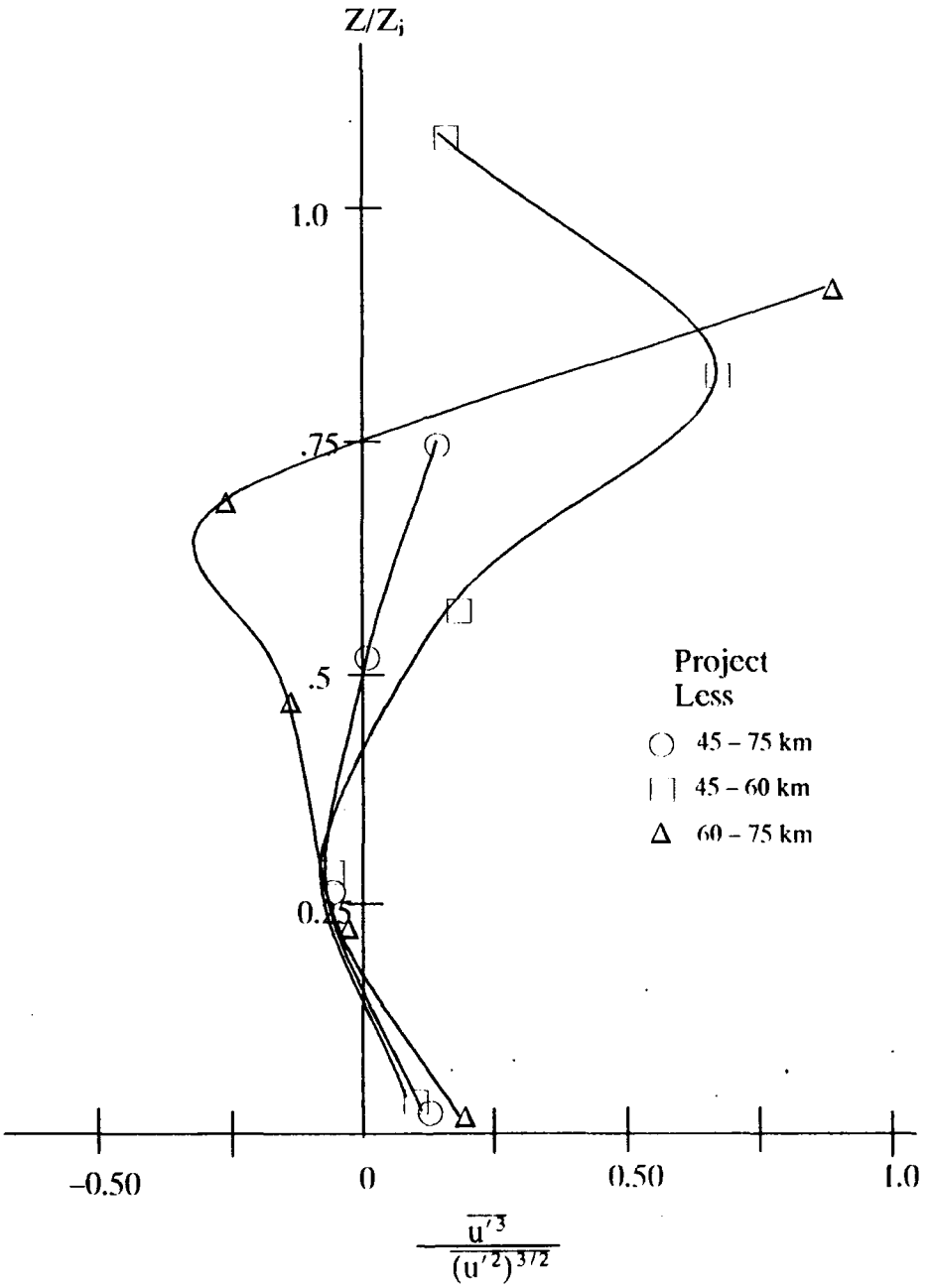

Figure 3.34 Vertical profile of the u–wind component skewness for the Project LESS.

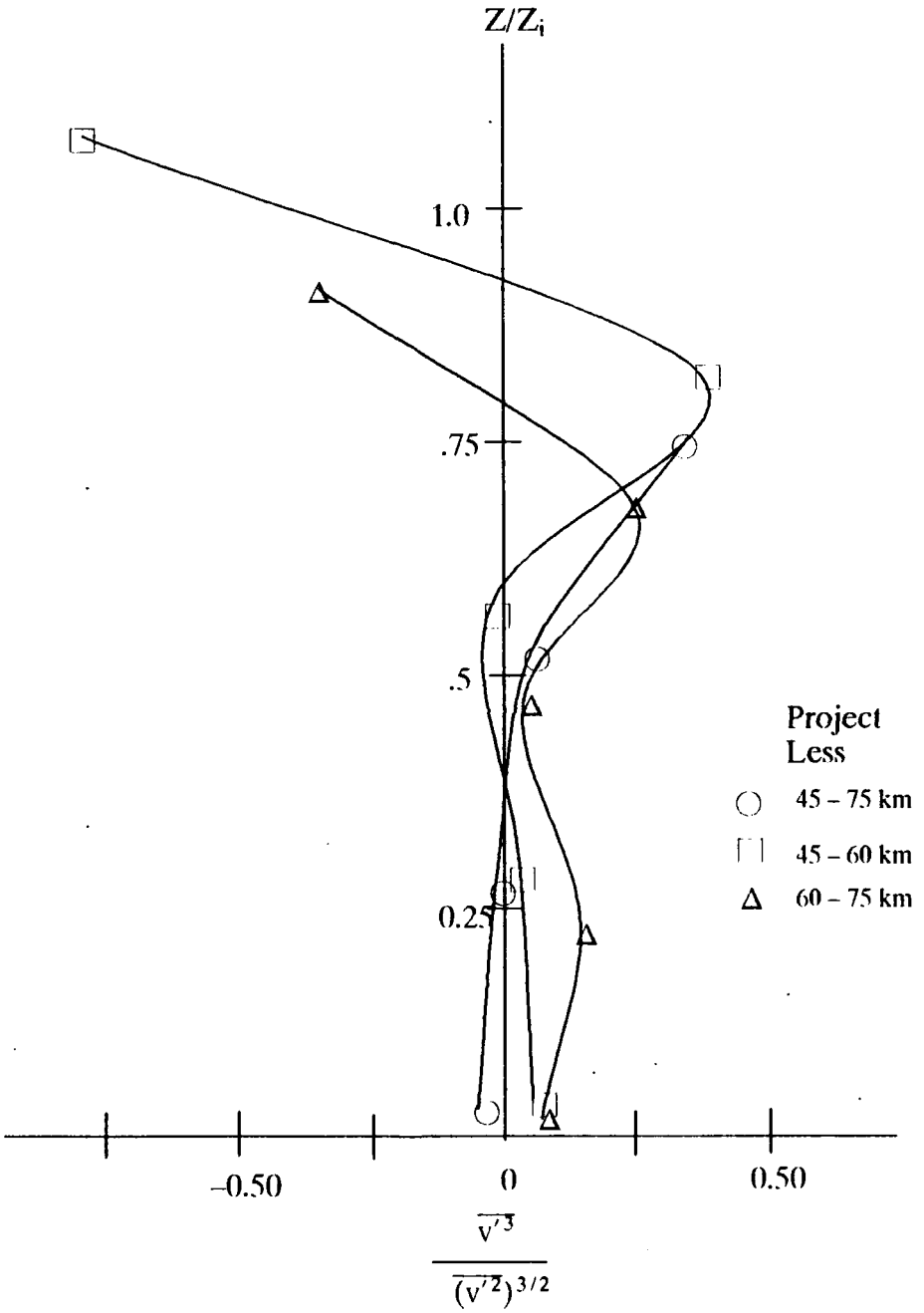

Figure 3.35 Vertical profile of the v–wind component skewness for the LESS

The vertical profile of the v–component of skewness (Figure 3.35) shows values very nearly zero in the lower half of the PBL and positive values at level 4 indicating narrow regions of relatively strong northerly momentum coupled with generally broad regions of weak southerly momentum. The skewness at level 5 for both the 45 – 60km and 60 – 75km segments is quite strongly negative, corresponding to narrow (broad) regions of strong (weak) southerly (northerly) momentum.

The skewness of the virtual potential temperature (Figure 3.36) is strongly positive near the surface and then decreases nearly linearly with height throughout the remainder of the PBL. The strong positive skewness at the lowest level is indicative of relatively narrow (broad) regions of relatively warmer (cooler) air, reflective of the strong buoyancy at this level.

The skewness of the specific humidity (Figure 3.37) is also strongly positive at lower levels, corresponding to the strong moisture flux near the Lake Michigan surface. At the mid–portion of the PBL, however, the skewness is strongly negative indicating that there are relatively narrow regions of drier air surrounded by relatively broad regions of moist air within the top of the cloud layer.

3.8.2 Vertical Velocity Skewness

As pointed out by Moeng and Rotunno (1990), a number of puzzling features concerning vertical velocity skewness have emerged from the comparison of LES model results with those from observational case studies involving convective PBLs. Figure 3.38 gives the vertical profile of vertical velocity skewness for the LESS, AMTEX and LES results of Moeng. For the LESS case, skewness is a maximum at level 1, decreases slightly with height within the subcloud layer and then is nearly constant with height in the cloud layer.

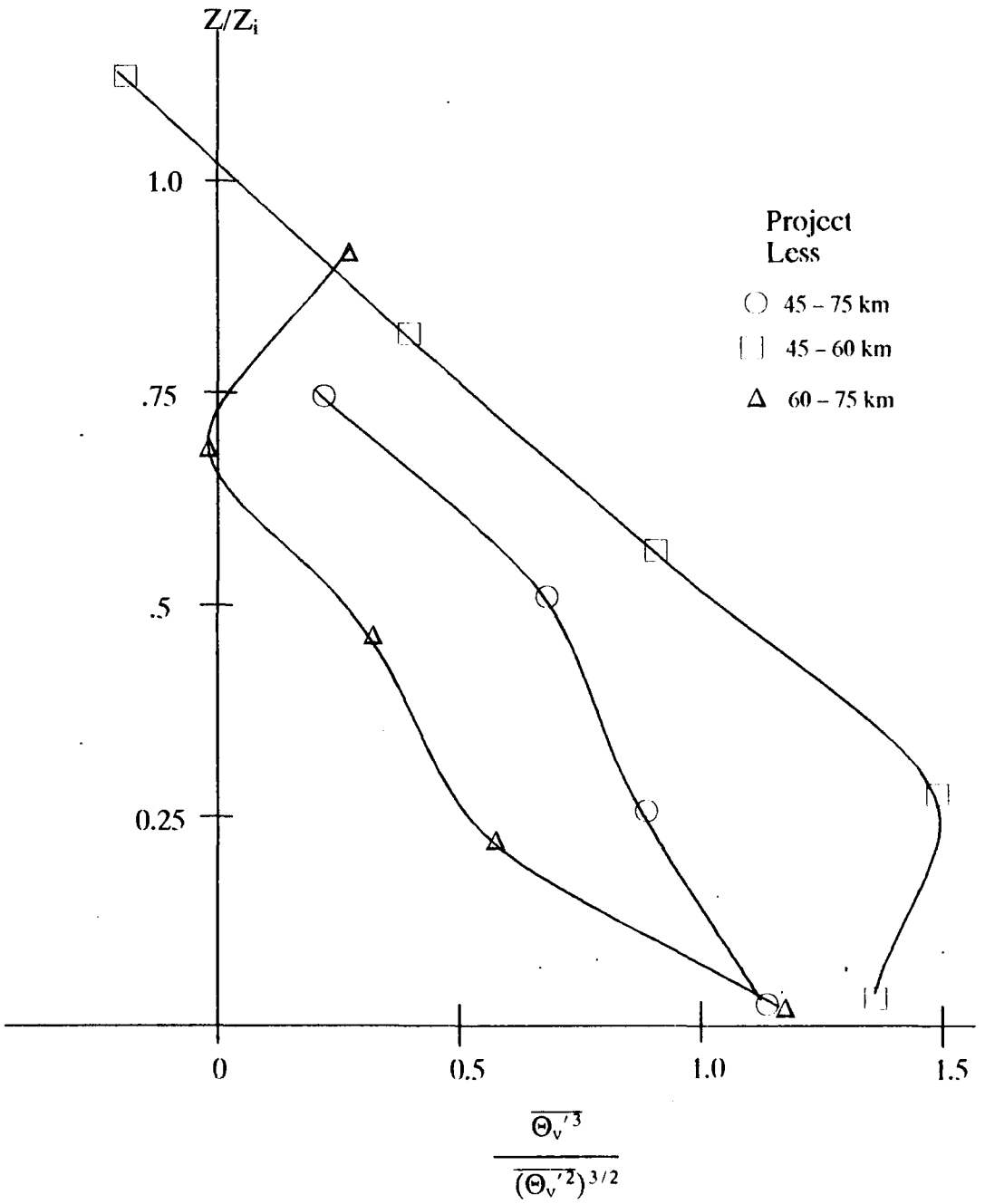

Figure 3.36 Vertical profile of the skewness of virtual potential temperature for the LESS

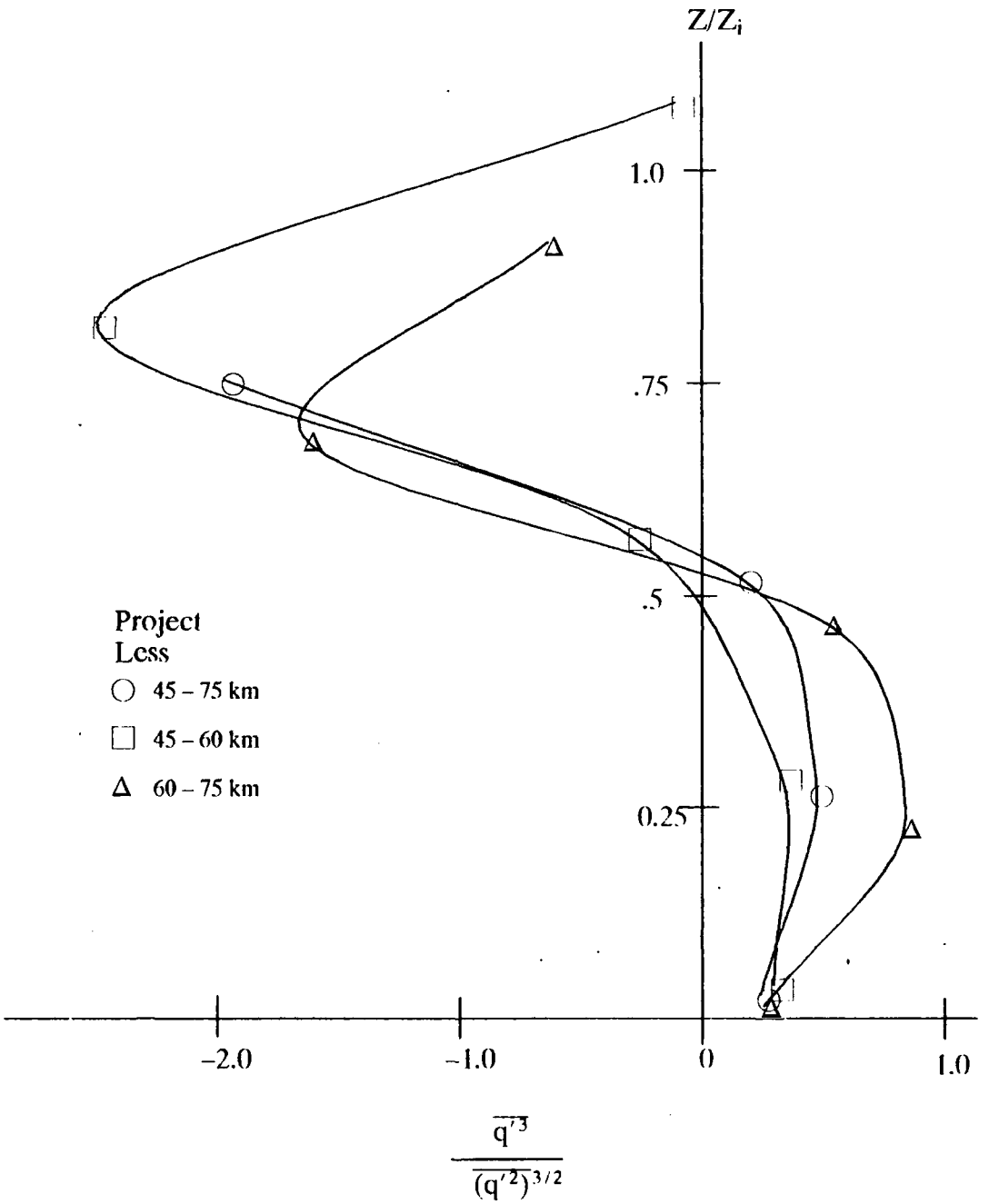

Figure 3.37 Vertical profile of the skewness of specific humidity for the LESS

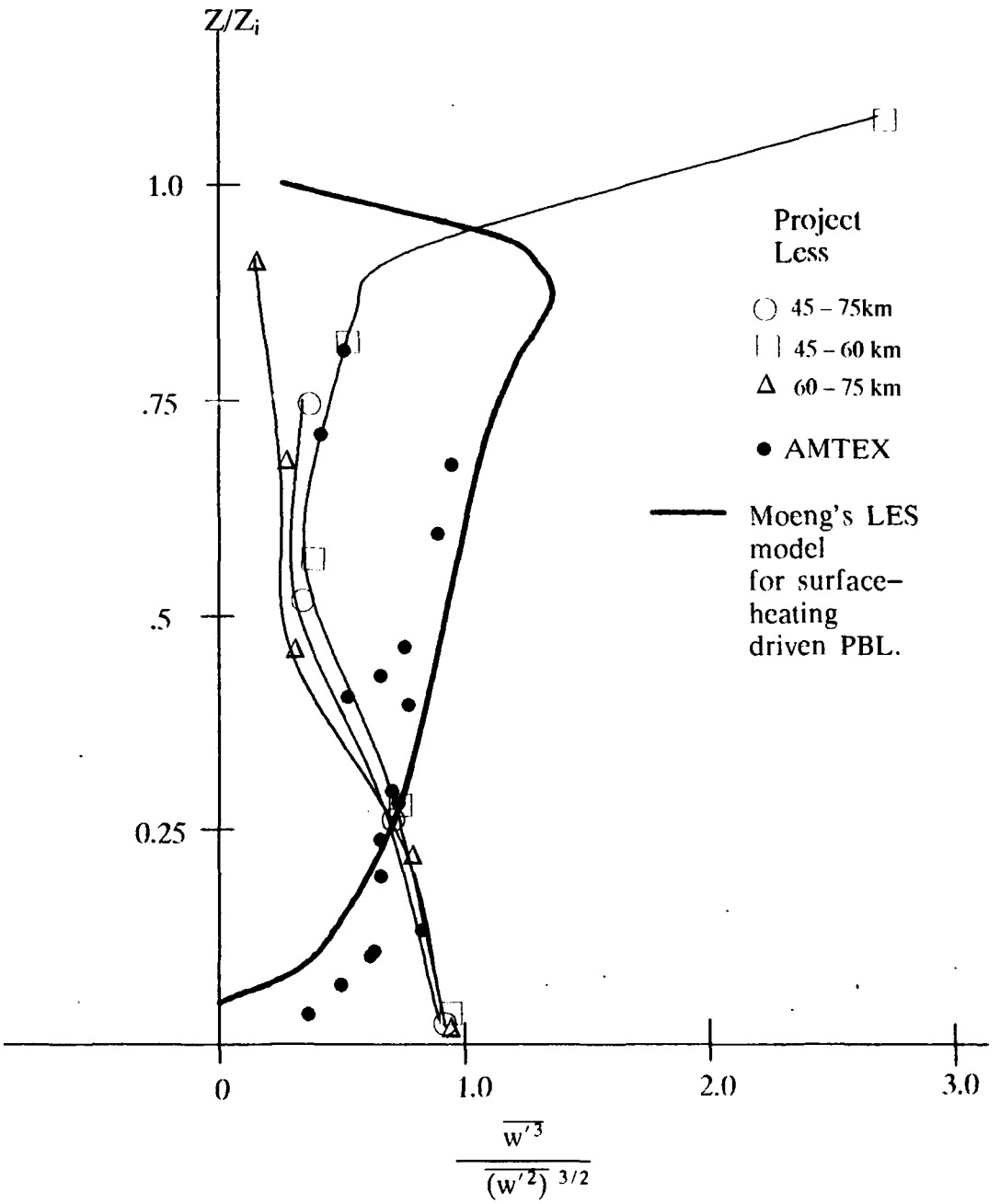

Figure 3.38 Vertical profiles of the vertical velocity skewness for the LESS and the AMTEX (solid circles) and Moeng's LES model (heavy dark line) for surface heating only.

The solid circles for the AMTEX results are taken from Moeng and Rotunno (1990) and agree well with the LES profile. The results from Moeng's LES model (denoted by the heavy dark line) are for the case of surface heating only. Skewness values for the LES model are smaller than those of the AMTEX or LESS study near the surface probably because subgrid–scale features dominate the LES results at these levels. The skewness for the model continues to increase until it reaches a maximum at approximately 0.9 Z/Z_i. It is in the upper portion of the PBL that model and observational case results generally do not agree. For example, as shown in Figure 3.38, the skewness remains nearly constant for the AMTEX and the LESS results in the upper half of the PBL but for Moeng's model continues to increase. This increase in $S_w(z)$ exits in all other large eddy simulations of the convective PBL (Moeng and Rotunno, 1990). This discrepancy in the upper portion of the PBL prompted Moeng and Rotunno to further investigate the cause of the increase in positive skewness with height in the upper portion of the PBL for a layer of thermal convection. They conducted numerical simulations for both no–slip and free–slip top conditions for Ra=380,000 and Pr=1. Surprisingly, they found that the no–slip condition results most closely replicated the LES simulation results for surface heating only. The free–slip condition for the surface heating case resulted in a skewness profile that is positive and relatively constant above a certain height. This surprising result prompted Moeng and Rotunno to further investigate whether the LES model contains some extra subgrid–scale stress near the upper part of the convective zone that would make its skewness behave more like that of the no–slip rather than the free–slip condition. Their examination of the data led to an answer in the negative. They went on to show why they believed the temperature inversion typically overlaying a convective PBL alters in some way the convective eddies impinging on this layer in a way that resembles the no–slip experiment. To test this hypothesis Moeng and

Rotunno carried out a third experiment with surface heating only with an imposed inversion in the upper portion of the numerical domain. The resulting vertical skewness profile (Figure 11, after Moeng and Rotunno, 1990) is very similar to the large–eddy simulations of a surface–heating–driven PBL and a surface–heating–driven PBL with a no–slip top. They explain the increase in skewness at the top of the PBL by considering the effect of the inversion on the turbulent kinetic energy. They hypothesize that the updrafts lose their kinetic energy at the inversion resulting in only broad weak downdrafts and, hence, positive skewness. Mason (1989) hypothesized that observed skewnesses at the top of the mixed layer are lower than the simulated ones due to the presence of "large scale features and inhomogeneities" in the real atmosphere. Mason went on to say that skewness in the boundary layer can be lowered below that replicated in simulations by the presence of mesoscale features if (a) these features are sinusoidal and therefore contribute to total vertical velocity variance but have near–zero skewness; and (b) if these features cannot be replicated by the simulation in question. These features may be related to gravity waves interacting with the boundary layer as described by Clark et al. (1984). There is some evidence of an increase in skewness at level 4 for the LESS 45–60km segment but this is most likely due to the secondary maximum in buoyancy at this flight level.

4. DETRENDED VS. RAW DATA

As mentioned earlier in Chapter 2, Wilczak and Businger (1983) have shown that when computing turbulence statistics in the convective PBL there is little difference between linear and quadratic detrending when compared to the variability when no detrending is used. This relatively short chapter will examine vertical profiles of a variety of turbulent statistics for which both second–degree polynomial detrended and non–detrended data have been used. In the latter case, equation (3.5) still holds where the average subtracted from the instantaneous value of the variable is simply the Reynolds average rather than the predicted value for the given meteorological variable.

4.1 TKE

Figure 4.1 shows the vertical profile of the normalized average TKE for both the detrended (open symbols) and non–detrended or raw (closed symbols) data of the Project LESS. The two sets of curves are both qualitatively and quantitatively in good agreement, with the TKE values for the non–detrended data consistently slightly larger than those for the detrended. This certainly is not surprising since one would expect the second moments calculated about the mean (non–detrended) to be larger than those calculated about the detrend curve. Generally maxima and minima are found at the same levels in both the detrended and raw data sets. The fact that the two sets of curves are quantitatively in good agreement suggests that very little synoptic or large–mesoscale signal is present in the u,v and w–wind components.

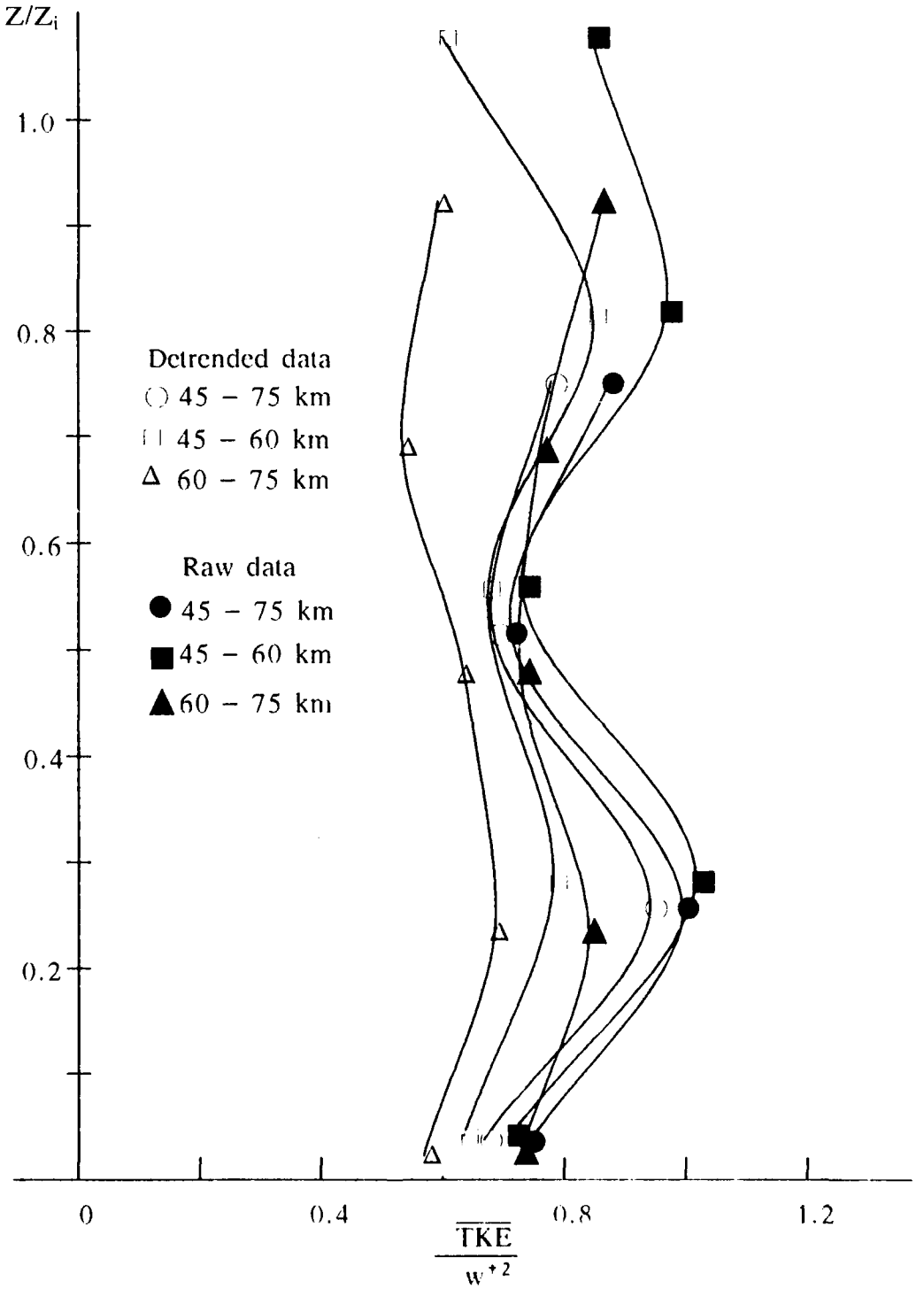

Figure 4.1 Vertical profile of the normalized average TKE for both the detrended and raw data for the Project LESS

4.2 Normalized Buoyancy

The vertical profiles of the normalized buoyancy for the detrended and raw data (Figure 4.2) present a picture quite different from that of the TKE. The buoyancy profiles for the detrended data for all three segments are remarkably similar with the aforementioned maximum found at levels 1 and 4. The striking similarity among the curves for the detrended data indicates that after synoptic and large–mesoscale signals are removed from the data, the 45–75km "hand–picked" data segment represents a nearly homogeneous portion of the convective PBL. The raw data, on the other hand do not indicate the same convergence in the buoyancy statistics. In fact, the two–15 km segments are nearly mirror images of one another with maximum in the normalized buoyancy for the 45–60km segment (at level 2) occurring at the same level as the minimum for the 60–75km segment for flight levels below 0.8 Z/Z_i. Likewise, the maximum in normalized buoyancy for the 60–75km segment occurs at the same level as the minimum for the 45–60km segment buoyancy for levels below 0.8 Z/Z_i. The lack of convergence in the normalized buoyancy statistic in this case suggests that synoptic and large–mesoscale features may be affecting the buoyancy. Considering the lack of trend in the vertical velocity, it would seem that the large scale features are more likely found in the virtual potential temperature. The comparison of the normalized average variance of virtual potential temperature for both the raw and detrended data (Figure 4.3) seems to support this hypothesis. The variances for the raw data for virtual potential temperature are as much as 300% larger than those for the detrended data.

4.3 Vertical Velocity Skewness

Figure 4.4 shows the vertical profile of the vertical velocity skewness for the Project LESS detrended and raw data. As was the case for TKE, the two sets of curves are in very good agreement both qualitatively and quantitatively.

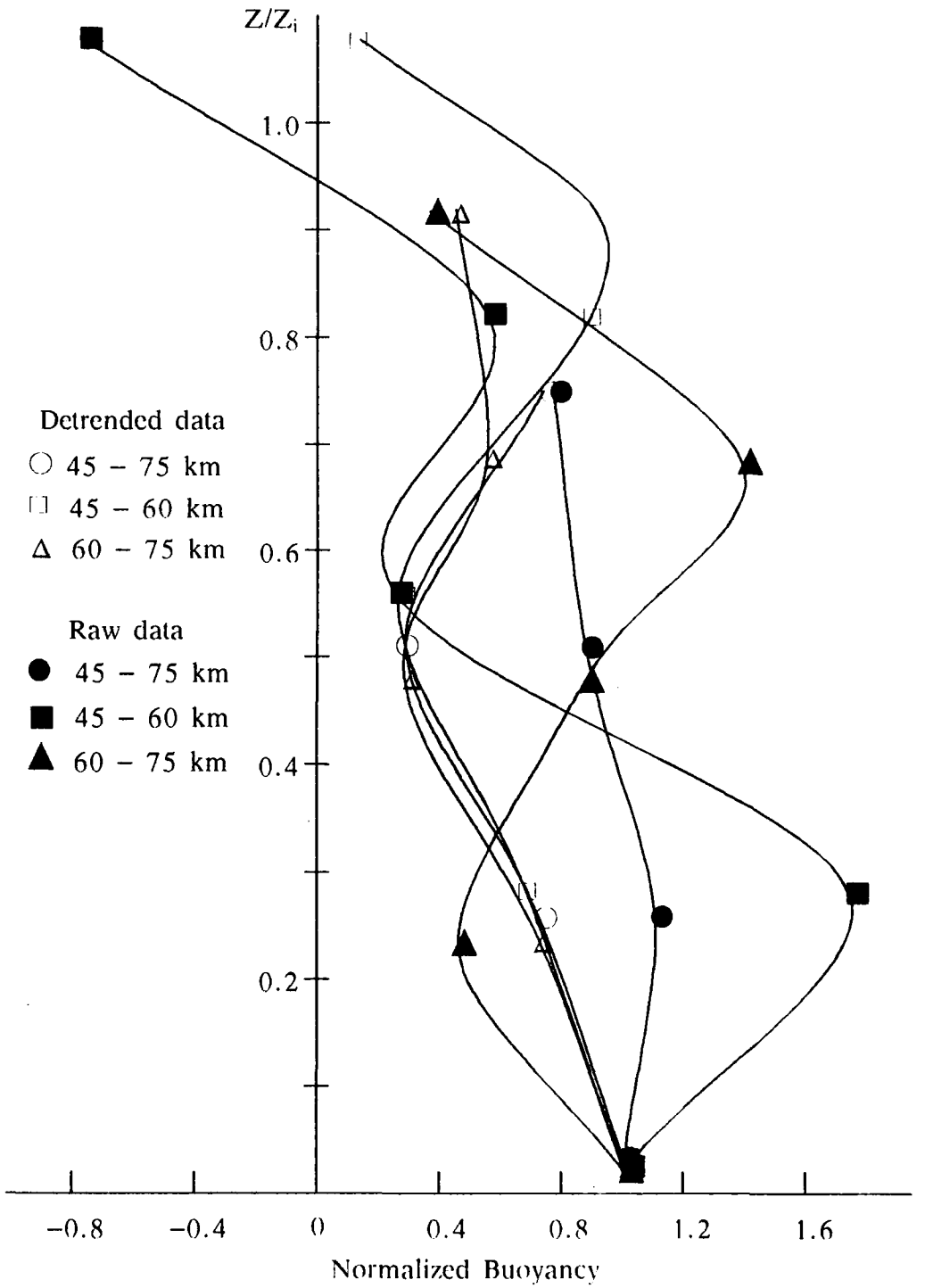

Figure 4.2 Vertical profile of the normalized buoyancy for both detrended and non-detrended data for Project LESS.

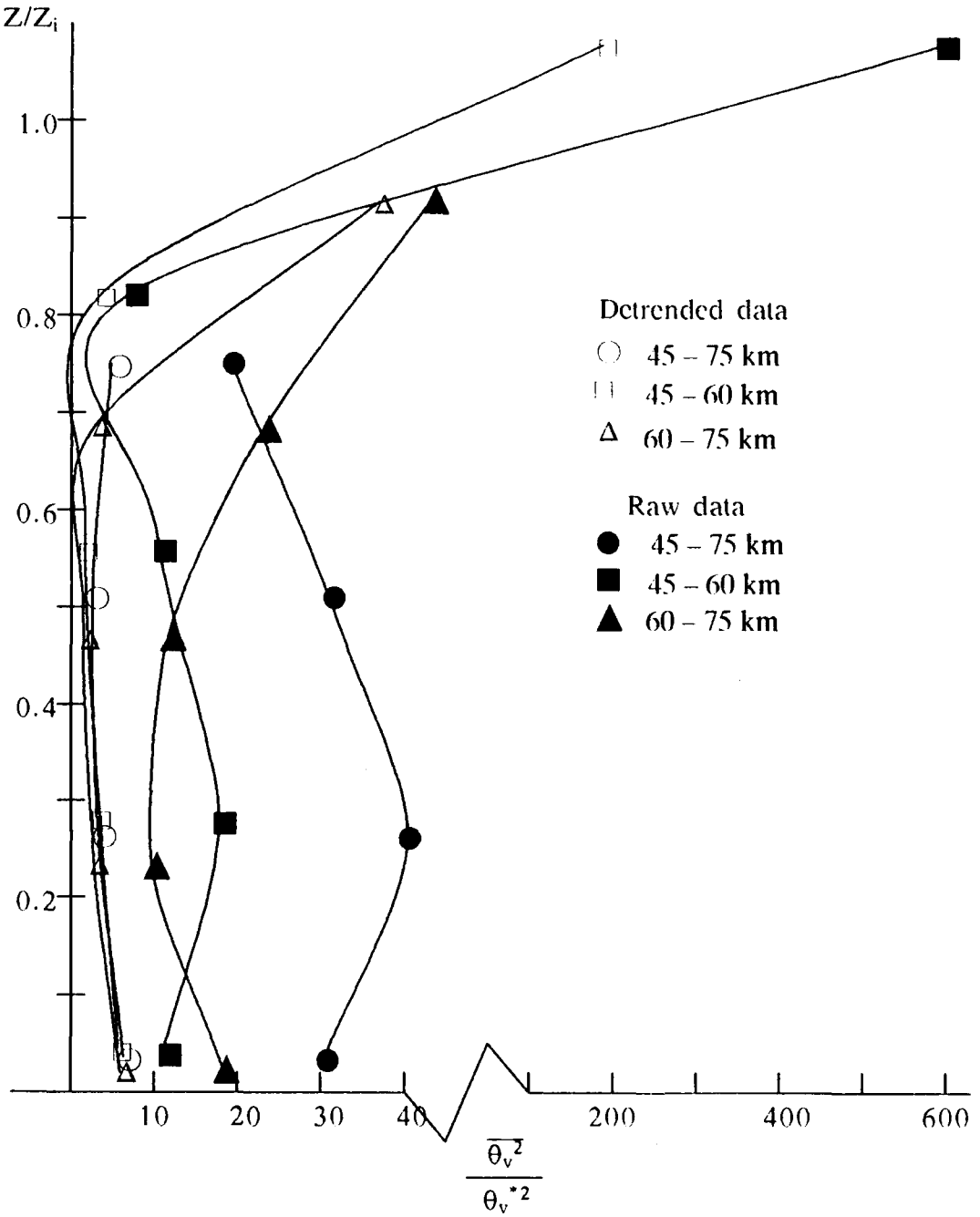

Figure 4.3 Vertical profile of the normalized average variance of virtual potential temperature for both detrended and raw data of the Project LESS

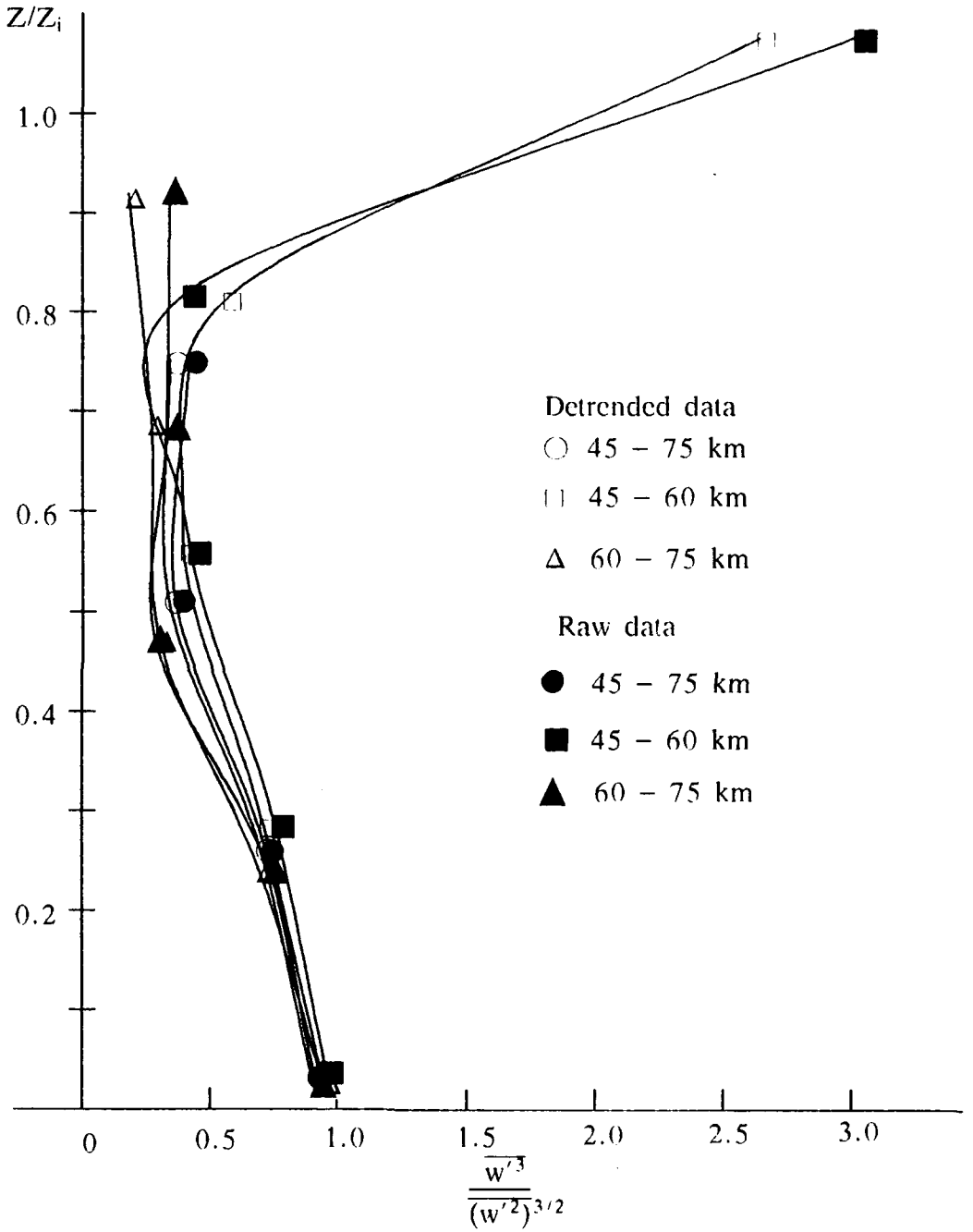

Figure 4.4 Vertical profile of the vertical velocity skewness for the Project LESS for both the detrended and raw data.

As pointed by out by Agee and Hart (1990), the vertical velocity skewness can be easily expanded into three terms as shown below:

$$\frac{\overline{w'^3}}{(\overline{w'^2})^{3/2}} = \frac{\overline{w_i^3}}{(\overline{w'^2})^{3/2}} + \frac{(-3\overline{w}\ \overline{w_i^2})}{(\overline{w'^2})^{3/2}} + \frac{2\overline{w}^3}{(\overline{w'^2})^{3/2}} \qquad (4.1)$$

$$\text{or} \qquad S = S_1 + S_2 + S_3 \qquad (4.2)$$

Because of continuity constraints numerical models have the condition that $\overline{w}=0$, which effectively reduces (4.2) to $S = S_1$. This is also the case for the detrended vertical velocity data for which $\overline{w} = 0$ per the earlier discussion. In the real atmospheric convective boundary layer this constraint of course does not exist. It seems somewhat surprising then that the skewness profiles for the raw and detrended vertical velocity data are so similar. Table 4.1 shown below gives the relative contributions of S_1, S_2 and S_3 to the total skewness for all three flight segments of the LESS:

Table 4.1 Relative contributions of the S_1, S_2 and S_3 terms to the total skewness of vertical velocity.

45 – 75 km Segment

Z/Z_i	$\overline{w}$	S_1	S_2	S_3	S
0.7500	0.1182	0.7395	-0.3141	0.0022	0.4277
0.5161	0.3192	1.2038	-0.9037	0.0435	0.3437
0.2581	0.2035	1.2385	-0.5125	0.0092	0.7351
0.0403	-0.0220	0.7962	0.0608	0.0000	0.8569

45 – 60 km Segment

Z/Z_i	$\overline{w}$	S_1	S_2	S_3	S
1.0807	-0.0307	2.9555	0.1379	-0.0002	3.0933
0.8158	0.1900	0.8834	-0.4807	0.0077	0.4103
0.5614	0.1946	0.9320	0.5538	0.0114	0.3896
0.2807	0.1898	1.2483	-0.4808	0.0077	0.7751
0.0439	-0.0419	0.7638	0.1134	-0.0001	0.8771

Table 4.1, continued

60 – 75 km Segment

Z/Z_i	$\overline{w}$	S_1	S_2	S_3	S
0.9194	-0.1836	-0.6658	1.0906	-0.0707	0.3541
0.6940	0.0461	0.5180	-0.1310	0.0002	0.3872
0.4776	0.4353	1.4800	-1.3050	0.1098	0.2849
0.2388	0.2172	1.2262	-0.5429	0.0109	0.6942
0.0373	-0.0022	0.8327	0.0061	0.0000	0.8388

Generally, the S_1, which is proportional to the turbulent vertical transport of vertical velocity variance, makes the largest contribution to the total skewness although the contribution of the S_2 is occasionally comparable to and may even exceed the S_1 term contribution. Because the S_3 involves the cube of the average vertical velocity (which is always less than unity) its contribution to total skewness is the least significant. As pointed out by Agee and Hart (1990), however, the S_2 and S_3 terms may make important contributions to skewness when $\overline{w}$ values exceed 0.1 ms^{-1} for observational periods <10 minutes (the longest observational period for the LESS is less than 8 minutes). This is the case because the vertical velocity data meet specific accuracy requirements (see NCAR RAF Bulletin 23). It would appear from this analysis that the vertical velocity skewness for raw and detrended data are very similar because of the lack of significant trend in this component of the wind. It appears that S_1 for the detrended data effectively equals $S_1 + S_2 + S_3$ for the raw data and, hence, the total skewnesses are nearly the same when this condition is met.

This section is brought to a close with a closer analysis of the sign and magnitude of the vertical velocity for the Project LESS data. Table 4.2 gives an account of the overall average vertical velocity, $\overline{w}$ (always zero for detrended data), the number of positive and negative vertical velocities, the average of positive and negative w_i values and the summation of the length segments for the positive and negative values.

Table 4.2 Results from analysis of the sign and magnitude of the vertical velocity for both detrended and raw data of the Project LESS for the 45 – 75 km segment.

Detrended Data

45 – 75 km Segment

Z/Z_i	Total # obs	# of pos. w	# of neg. w	Average of pos. w	Average of neg.w	Length of pos. w(m)	Length of neg. w(m)
0.7500	8441	4053	4388	0.9029	−0.8344	14405	15595
0.5161	8063	3735	4328	0.9416	−0.8123	13897	16103
0.2581	8256	3586	4688	1.0702	−0.8147	12965	17035
0.0403	8683	3684	4999	0.9811	−0.7230	12728	17272

Raw Data

45 – 75 km Segment

Z/Z_i	Total # obs	# of pos. w	# of neg. w	Average of pos. w	Average of neg.w	Length of pos. w(m)	Length of neg. w(m)
0.7500	8441	4461	3980	0.9555	−0.8199	15855	14145
0.5161	8063	4710	3353	1.0414	−0.7093	17525	12475
0.2581	8256	4180	4076	1.1302	−0.7471	15189	14811
0.0403	8683	3612	5071	0.9783	−0.7346	12480	17520

For the detrended data, the analysis of the sign and magnitude of w is consistent with the values of the vertical velocity skewness. For example, the skewness at level 4 for the 45 – 75 km segment was found to be 0.3305 (Table 3.4). For the detrended data, there are fewer positive than negative vertical velocities at this level and the average (+) vertical velocity is stronger (+0.9029) than the average (−) vertical velocity (−0.8344). The summation of the length segments for positive and negative vertical velocities confirms that this level is marked by relatively narrow regions of strong updraft, surrounded by relatively broad regions of downdraft. The results for the raw data do not lead to the same conclusion. For the same level 4 in the raw data, (+) velocities are more numerous but still stronger than (−) velocities. Hence, one would conclude that at this flight level, broad regions of relatively stronger upward vertical velocities were dominating over narrow regions of relatively weak downdrafts. This analysis points out the importance of not drawing conclusions about

the structure of updrafts and downdrafts from vertical velocity skewness when $\overline{w}$ does not equal zero.

5. SUMMARY AND CONCLUSIONS

Meteorlogical data sampled at a frequency of 20Hz and collected by NCAR research aircraft have been analyzed for the CAO event of 10 Jan 84 over Lake Michigan during the Project LESS. This particular CAO event was associated with a surface anticyclone–cyclone pair between which southward transport of continental polar air occurred resulting in the formation of a Type I CTBL over the relatively warm waters of Lake Michigan. A brief comparison of 850mb temperatures from the PROAM and PROAMU for the 10 Jan 84 case and the results from the analysis done by Konrad and Colucci (1989) indicates this event represents a strong if not extreme CAO event.

The NCAR King and Queen Air aircraft collected data at five vertically stacked flight levels oriented perpendicular to the mean wind (which was northerly) at a latitude of 43°N in a west–east and east–west fashion (i.e. perpendicular to the 2–d cloud streets which had formed). Because it was desirable to obtain turbulence statistics over as homogeneous a region as possible, a "hand–picked" data set that attempted to eliminate the effects of the interfacial and inversion layer and the Michigan and Wisconsin land breezes was chosen. The resulting data set included the u,v,w,θ_v and q 20Hz data collected 45–75km from the Wisconsin shore. This turned out to be a fortuitous choice since the data collection period over this flight segment was less than 10 minutes for each flight level, allowing for the use of mean vertical velocities in the S_w calculations for raw data.

Data used in the turbulence statistics have been detrended using a second–degree polynomial fit. Comparisons were made between the LESS results and those for two other observational case studies; the AMTEX and MASEX. Turbulence statistics were also compared to those of the models of Deardorff (1980) and Moeng(1984). Comparisons among

observational case studies and model results are facilitated by the use of appropriate scaling factors such as Z_i and w^*, the depth of the mixed layer and the free convective scaling velocity, respectively.

Vertical profiles of the means of u and v show very little shear in the mean horizontal wind except near the base of the inversion at the top of the mixed layer. The vertical profile of the mean vertical velocity shows a positive maximum in the subcloud layer and weak subsidence near the inversion base for the 45–60km and 60–75km segments. The vertical profile of the mean virtual potential temperature and specific humidity reveals the drying and warming effect of the entrainment of air from the inversion layer overlying the convective PBL.

The vertical profiles of the normalized average u,v and w variances indicates that the values are, generally speaking, larger for the LESS results than for the AMTEX, especially for the w variance. This would indicate that for a given surface buoyancy flux, as accounted for in the normalization by w^*, the LESS CTBL is more turbulent that the AMTEX. The vertical profiles of the normalized average variances for the virtual potential temperature and the specific humidity show the effects of the entrainment very clearly at the top of the PBL where the variances are as much as 50 times larger than over the bulk of the mixed layer. The larger increase in the θ_v variance over that of q near the top of the mixed layer agrees well with the results of Chou et al. and results from a larger normalized virtual potential temperature jump ($\Delta\theta_v/\theta_v^*$) than humidity jump ($\Delta q/q^*$). A comparison of the LESS u variance with that of Moeng's LES model shows general good agreement in the lower half of the PBL but larger values for the LESS results in the upper half. The latter may be due to the secondary maximum in buoyancy at level 4 in the LESS case resulting in corresponding increase in u variance.

Perhaps the most significant finding in the research presented is the discovery of a secondary buoyancy maxima at level 4 which appears to be due to condensational heating

which has resulted from the formation of precipitating and clouds at this level. While results for the normalized buoyancy from the MASEX and AMTEX studies are generally in very good agreement with the LESS results in the lower half of the PBL, neither of the other two studies indicate this secondary maxima in buoyancy within the cloud layer. The LESS results, however, are in very good agreement at least qualitatively with the model results of Deardorff. The vertical profile of the normalized average vertical eddy moisture flux shows good agreement between the LESS and MASEX results with the maximum occurring for the LESS at level 2 where both the w and q variances were large.

The vertical profile of the normalized average TKE for the LESS case study shows maxima at levels 2 and 4. Both maxima appear to be primarily due to the corresponding maximum in the horizontal component of TKE at these same levels. Both the horizontal and vertical components of TKE are stronger for the MASEX case than for the LESS. This is probably due to the shorter fetch for the former resulting in greater shear, and, hence, greater turbulence. For both cases, the horizontal component is stronger than the vertical but just the opposite is true of the vertical flux of the respective components of TKE. The vertical flux of the vertical component of TKE is generally much stronger than the vertical flux of the horizontal component. For the LESS and AMTEX data, the values for the vertical flux of horizontal TKE are comparable, however, the vertical flux of vertical TKE is generally stronger than for the AMTEX case indicating that the turbulent eddies for the LESS case are more efficient and capable at transporting the vertical component of TKE than are the eddies for the AMTEX. The analysis of the ratio of the vertical flux of velocity variance between the horizontal and vertical components for all three case studies shows that the LESS has a stronger vertical transport of vertical variance at the lowest levels than either of the other two case studies.

Much controversy has developed in the literature with regards to comparisons of vertical velocity skewness for observational case studies and models. For observational studies

vertical velocity skewness, S_w, is positive throughout the Type I convective PBL and nearly constant in the upper half of the PBL. Model S_w is erroneously negative in the surface layer for the surface heating only simulation probably because of poor subgrid–scale parameterizations. Unlike the observational case study skewness, model skewness continues to increase with height reaching a maximum at 0.9 Z/Z_i. There is some evidence of an increase in S_w for the Project LESS at level 4 for the 45–60km flight leg, but this is probably due to the secondary maximum in buoyancy at this level discussed earlier in Chapter 3.

Comparisons made between turbulence statistics calculated from the detrended and raw data for TKE, S_w and buoyancy show very similar profiles for the first two quantities but not for the last. Similarities in the TKE and S_w profiles for the two meteorological parameters are indicative of very little trend in the three wind components. The difference in the buoyancy profiles suggests that a significant trend at the synoptic or large–mesoscale level may exist in the virtual potential temperature as evidenced in the plots of the raw 20Hz data (Figure 2.5).

As for future work, it would be interesting to develop a prototype Type I CTBL LES for which sensitivity studies could be done by adding one physical process at a time. Comparisons could be made between the results of this new LES study and those presented in this study. A fellow member of the Purdue Mesoscale Convection and Climatology (MCAC) research group, Guan–Shu Rao, is actively pursuing such a project with Chin–Hoh Moeng at NCAR.

Future study could also involve comparisons of turbulent statistics for the Type I 'vs' the Type II CTBL to explore how the transitions between the two CTBLs occur (using S_w profiles, for example).

LIST OF REFERENCES

LIST OF REFERENCES

Agee, E.M. and T.S. Chen, 1973: A model for investigating eddy viscosity effects on mesoscale cellular convection. *J. Atmos. Sci.*, 30, 180–199.

Agee, E.M., T.S. Chen and K.E. Dowell, 1973: A review of mesoscale cellular convection. *Bull. Amer. Met. Soc.*, 54, 1004–1012.

Agee, E.M., K.E. Dowell, 1974: Observational studies of mesoscale cellular convection. *J. Appl. Met.*, 13, 46–53.

Agee, E.M., Howley, R.P., 1977: Latent and sensible heat flux calculations at the air–sea interface during AMTEX 74. *J. Appl. Met.*, 16, 443–447.

Agee, E.M., 1982: An introduction to shallow convective systems. *Cloud Dynamics*, Agee and Asai ed., D. Reidel pub, 3–30.

Agee, E.M., 1984: Observations from space and thermal convection: A historical perspective. *Bull. Amer. Met. Soc.*, 65, 938–949.

Agee, E.M., 1987: Mesoscale cellular convection over the oceans. *Dyn. Atmos. Oceans*, 10, 317–341.

Agee, E.M., and S. Gilbert, 1989: Aircraft investigation of mesoscale convection over Lake Michigan during the 10 January 1984 cold air outbreak. *J. Atmos. Sci.*, 46, 1877–1897.

Agee, E.M., and M. Hart, 1990: Boundary layer structure over Lake Michigan during a wintertime cold air outbreak. *J. Atmos. Sci.*, 47, 2294–2316.

Benard, H., 1901: Les tourbillons cellulaires dans une nappe liquids transportant de la chaleur par convection en regime permanent. *Ann. Chim. Phys.*, 23, 62–144.

Benard, H., 1927: Hydrodynamique experimental sur les tourbillons cellulares et la theorie de Rayleigh. *Acedemie Des Sciences*, 185, 1109–11, 1256–59.

Benard, H., 1928: Sur les tourbillons cellularies, les tourbillons en bandes, et la theorie de Rayleigh. *Bull. Soc. franc. phys.*, 266, 112–225.

Boussinesq, J., 1903: *Theorie Analytique de la Chaleur*, 2, 172.

Braham, R.R., and R.D. Kelly, 1982: Lake–effect snow storms on Lake Michigan. *Cloud Dynamics*, Agee and Asai ed., D. Reidel pub., 87–102.

Braham, R.R., and Dungey, M. 1984: Quantitative estimates of the effect of Lake Michigan on snowfall. *J Climate and Appl. Met.*, 23, 940–949.

Braham, R.R., 1986: Cloud and motion fields in open-cell convection over Lake Michigan. *Proc. 23rd Conf. Radar Met. and Conf. on Cloud Phys. Snowmass, CO Sept 22-26.*

Brunt, Sir David, 1951: Experimental cloud formation. *Compendium of Meteorology,* American Meteorological Society, 1255-1262.

Busse, F.H., 1962: Das stabilitatsverhalten der Zellularkonvektion bei endlicher amplitude, Dissertation, University of Munich, trans. by S.H. Davis, the Rand Corporation, Santa Monica, Calif. 1966 99pp.

Chandrasekhar, S., 1957: Thermal convection. *Daedalus*, 86, 4, 325-339.

Channon, S.A.,Jr., 1968: Precipitation climatology of Lake Michigan Basin. *Bull. No. 52, Ill. St. Water Survey*, Urbana, 46 pp.

Christopherson, D.G., 1940: Note on the vibrations of membranes. *Quart. J. Math., 11*, 63-63.

Chou, S.-H., D. Atlas and E.-N. Yeh, 1986: Turbulence in a convective marine atmospheric boundary layer. *J. Atmos. Sci.*, 43, 547-564.

Clark, T.L., T. Hauf and J.P. Kuettner, 1986: Convectively forced internal gravity waves: Results from two-dimensional numerical experiments. *Quart. J. Roy. Meteor. Soc.*, 112, 899-925

Deardorff, J.W., 1980: Stratocumulus-capped mixed layer derived from a three dimensional model. *Bdry. Layer Met.*, 18, 495-527

Dewey, K.F., 1970: An analysis of lake-effect snowfall, Bull. Ill. Geogr. Soc., 12, 27-42.

Friehe, C.A., R.L. Grossman and Y. Pann, 1986: Calibration of an airborne Lyman-Alpha hygrometer and measurement of water vapor flux using a thermoelectric hygrometer. *J. Atmos. and Oceanic Tech.*, 3, 299-304.

Hubert, L.F., 1966: Mesoscale cellular convection. *Rept. 37*, Meteorological Satellite Laboratory, Wasington, D.C., 68pp.

Jeffreys, H., 1926:, The stability of a layer of fluid heated from below. *Phil. Mag.* 2, 833-844.

Jeffreys, H., 1928:, Some cases of instability in fluid motion. *Proc. Roy. Soc.* (London), 118, 195-208.

Konrad, C.E., II, and S.J. Collucci, 1989: An examination of extreme cold air outbreaks over eastern North America. *Mon. Wea. Rev.*, 117, 2687-2700.

Kruger, A.F., and S. Fritz, 1961: Cellular cloud patterns revealed by TIROS I. *Tellus*, 13, 1-7.

Krishnamurti, R., 1973: Some further studies on the transition to turbulent convection. *J. Fluid Mech.*, 60, 285-303

Krishnamurti, R., 1975: On cellular cloud patterns. Part 1: Mathmatical model. *J. Atmos. Sci.*, 32, 1353-1363.

Lenschow, D.H., and E.M. Agee, 1976: Preliminary results from the Air Mass Transformation Experiment (AMTEX). *Bull. Amer. Met. Soc.*, 44, 1346–1355.

Lenschow, D.H., J.C. Wyngaard and W.T. Pennel, 1980: Mean–field and second–moment budgets in a baroclinic, convective boundary layer. , 37, *J. Atmos. Sci.* 1313–1326.

Low, R.A., and D. Brunt, 1925: Instability of an inviscous fluid motion. *Nature*, 115, 299–301

Malkus, W.V.R., and G. Veronis, 1958: Finite amplitude cellular convection. *J. Fluid Mech.*, 4, 225–260.

Mason, P.J., 1989: Large–eddy simulation of the convective atmospheric boundary layer. *J. Atmos. Sci.*, 46, 1492–1516.

Moeng, C.–H., 1984: A large–eddy simulation model for the study of planetary boundary–layer turbulence. *J. Atmos. Sci.*, 41, 2052–2062.

Moeng, C.–H., and Rotunno, R. 1990: Vertical–velocity skewness in the buoyancy–driven boundary layer. *J. Atmos. Sci.*, 47, 1149–1162.

Neter, J. Wasserman, M. and Whitmore, G.A., 1988: *Applied Statistics*, Allyn and Bacon inc., 1006pp

Palm, E., 1960: On the tendency toward hexagonal cells in steady convection. *J. Fluid Mech.*, 8, 183–192.

Pellew, A., and R,V. Southwell, 1940: *On maintained convection motion in a fluid* heated from below. *Proc. Roy. Soc.*, A, 176, 312–343.

Prout, W.1834: *Bridgewater Treatises*, 8, edited by W. Pickering, London, 65.

Priestly, C.H.B.,1962: Width–height ratio of large convective cells, *Tellus*, 14, 123–124.

Ray, D., 1965: Cellular convection with nonisotropic eddys, *Tellus*, 17, 434–439.

Rayleigh, O.M., 1916: On convection currents in a horizontal layer of fluid, when the higher temperature is on the underside. *Phil. Mag.*, Ser. 6, 32, 529–546.

Rothermel, J., and E.M. Agee, 1980: Aircraft investigation of mesoscale cellular convection during AMTEX 75. *J. Atmos. Sci.*, 37, 1027–1040.

Rothermel, J., and E.M. Agee, 1986: A numerical study of atmospheric convective scaling. *J. Atmos. Sci.*, 43, 1185–1197.

Segal, L.A. and J.T. Stuart, 1962: On the question of the preferred mode in cellular thermal convection. *J. Fluid Mech.*, 13, 289–306.

Sheu, P.J., and E.M. Agee, 1977: Kinematic analysis and air–sea heat flux associated with mesoscale cellular convection during ATMEX 75. *J. Atmos. Sci.*, 34, 793–801.

Stommel, H., 1947: A summary of the theory of convection cells. Ann. N.Y. Acad. Sci., 48 715–726.

Stull, R.B., 1988: *An Introduction to Boundary Layer Meteorology*, Kluwer Academic, 666 pp.

Sun, W.–Y., and W.–R. Hsu, 1988: Numerical study of a cold air outbreak over the ocean. *J. Atmos. Sci.*, 45, 1205–1227.

Tippleskirch, H.V.,1956: Uber konvektionzellen, insbesondene im flussigen Schwefel. *Beitr. Phys. Atmos.* , 29, 37–54.

Van Der Borght, R., 1975: A non–linear investigation of atmospheric cellular convection. *J. Meteor. Soc. Japan,* 53, 247–254.

Wexler, H., 1943: Some aspects of dynamic anticyclones. The University of Chicago Inst. Meteor., Misc. Rept. No. 8, 28pp.

Wexler, H., 1951: Anticyclones. Compendium of Meteorology, T.F. Malone, Ed. Amer. Meteor. Soc. 621–629.

Whitehead, J.A. Jr., 1974: Oscillatory and collective instabilities in large Prandtl number convection. *J. Fluid Mech.* 66, 67–90.

Wilczak, J.M. and Joost A. Businger, 1983: Thermally indirect motions in the convective atmospheric boundary layer. *J. Atmos. Sci.*, 40, 343–358.

Zishka, K., and Smith,P.J., 1980: The climatology of cyclones and anticyclones over North America and surrounding environs for January and July, 1950–1977. *Mon. Wea. Rev.* , 108, 387–401.